

AEDC-TR-76-109

cy.10



**AN EVALUATION OF JET SIMULATION
PARAMETERS FOR NOZZLE AFTERBODY TESTING
AT TRANSONIC MACH NUMBERS**

**PROPULSION WIND TUNNEL FACILITY
ARNOLD ENGINEERING DEVELOPMENT CENTER
AIR FORCE SYSTEMS COMMAND
ARNOLD AIR FORCE STATION, TENNESSEE 37389**

October 1976

Final Report for Period January 1975 — June 1976

Approved for public release; distribution unlimited.

Property of U. S. Air Force
AEDC LIBRARY
1 AUG 1976

Prepared for

**DIRECTORATE OF TECHNOLOGY (DY)
ARNOLD ENGINEERING DEVELOPMENT CENTER
ARNOLD AIR FORCE STATION, TENNESSEE 37389**

NOTICES

When U. S. Government drawings specifications, or other data are used for any purpose other than a definitely related Government procurement operation, the Government thereby incurs no responsibility nor any obligation whatsoever, and the fact that the Government may have formulated, furnished, or in any way supplied the said drawings, specifications, or other data, is not to be regarded by implication or otherwise, or in any manner licensing the holder or any other person or corporation, or conveying any rights or permission to manufacture, use, or sell any patented invention that may in any way be related thereto.

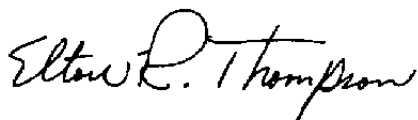
Qualified users may obtain copies of this report from the Defense Documentation Center.

References to named commercial products in this report are not to be considered in any sense as an endorsement of the product by the United States Air Force or the Government.

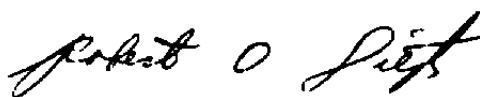
APPROVAL STATEMENT

This technical report has been reviewed and is approved for publication.

FOR THE COMMANDER



ELTON R. THOMPSON
Research and Development Division
Directorate of Technology



ROBERT O. DIETZ
Director of Technology

UNCLASSIFIED

REPORT DOCUMENTATION PAGE		READ INSTRUCTIONS BEFORE COMPLETING FORM
1 REPORT NUMBER AEDC-TR-76-109	2 GOVT ACCESSION NO	3 RECIPIENT'S CATALOG NUMBER
4 TITLE (and Subtitle) AN EVALUATION OF JET SIMULATION PARAMETERS FOR NOZZLE AFTERBODY TESTING AT TRANSONIC MACH NUMBERS		5 TYPE OF REPORT & PERIOD COVERED Final Report - January 1975 - June 1976
		6 PERFORMING ORG REPORT NUMBER
7 AUTHOR(s) William Lee Peters - ARO, Inc.		8 CONTRACT OR GRANT NUMBER(s)
9 PERFORMING ORGANIZATION NAME AND ADDRESS Arnold Engineering Development Center (DY) Air Force Systems Command Arnold Air Force Station, Tennessee 37389		10 PROGRAM ELEMENT PROJECT TASK AREA & WORK UNIT NUMBERS Program Element 65807F
11 CONTROLLING OFFICE NAME AND ADDRESS Arnold Engineering Development Center (DYFS) Arnold Air Force Station Tennessee 37389		12 REPORT DATE October 1976
		13 NUMBER OF PAGES 95
14 MONITORING AGENCY NAME & ADDRESS (if different from Controlling Office)		15 SECURITY CLASS (of this report) UNCLASSIFIED
		15a DECLASSIFICATION/DOWNGRADING SCHEDULE N/A
16 DISTRIBUTION STATEMENT (of this Report) Approved for public release; distribution unlimited.		
17 DISTRIBUTION STATEMENT (of the abstract entered in Block 20, if different from Report)		
18 SUPPLEMENTARY NOTES Available in DDC		
19 KEY WORDS (Continue on reverse side if necessary and identify by block number) <div style="display: flex; justify-content: space-between;"> <div> jets plumes jet flow transonic flow </div> <div> wind tunnel test aerodynamic characteristics Reynolds number </div> </div>		
20 ABSTRACT (Continue on reverse side if necessary and identify by block number) <p>The objective of this investigation was to evaluate various jet simulation parameters in an attempt to establish a method of matching hot jet interference with cold jet flows. Successful parameters were determined based on their ability to correlate integrated afterbody pressure drag, a measurement of aerodynamic interference, for jet flows of varying total temperature. Data used in this investigation were obtained from experiments conducted in the AEDC Propulsion Wind Tunnel (16T) with three different isolated</p>		

UNCLASSIFIED

UNCLASSIFIED

20. ABSTRACT (Continued)

nozzle/afterbody configurations at free-stream Mach numbers from 0.6 to 1.5. Gas temperature effects on pressure drag were acquired with a convergent nozzle utilizing an air/ethylene burner to produce gas temperatures from 540 to 3,300°R. In addition, the jet effects of varying internal nozzle geometry, specifically nozzle divergence half-angle and nozzle exit-to-throat area ratio, were investigated utilizing high-pressure air as the nozzle exhaust gas. Jet simulation parameters were evaluated for jet flows where nozzle exit-to-throat area ratio was varied from 1.0 to approximately 1.5 and where divergence half-angle was varied from 0 to 10 deg. Correlation parameters that characterize the inviscid jet plume boundary provided significantly better hot and cold jet simulation than nozzle total pressure ratio for underexpanded nozzle flow conditions. Afterbody drag was essentially independent of nozzle divergence half-angle when nozzle total pressure ratio was duplicated for underexpanded nozzle flows at all free-stream Mach numbers. The inviscid plume shape parameters (Δv and $P_j/\gamma P_\infty$) modified by including the area ratio, e.g., $(\Delta v) (A/A^*)$ and $(P_j/\gamma P_\infty) (A/A^*)$, produced good drag correlation for variable nozzle exit-to-throat area ratio at nozzle total pressure ratios above the nozzle design pressure ratio for afterbodies with attached flow.

PREFACE

The work reported herein was conducted by the Arnold Engineering Development Center (AEDC), Air Force Systems Command (AFSC), under Program Element 65807F. The results presented were obtained by ARO, Inc. (a subsidiary of Sverdrup & Parcel and Associates, Inc.), contract operator of AEDC, AFSC, Arnold Air Force Station, Tennessee, under ARO Project Number P32P-AOA. The Air Force project engineer for this program was E. R. Thompson, AEDC/DYR. The author of this report was William Lee Peters, ARO, Inc. The manuscript (ARO Control No. ARO-PWT-TR-76-67) was submitted for publication on June 29, 1976.

CONTENTS

	<u>Page</u>
1.0 INTRODUCTION	7
2.0 APPARATUS	
2.1 Test Facility	9
2.2 Test Article and Support System	9
2.3 Instrumentation	10
3.0 PROCEDURE	
3.1 Test Conditions and Techniques	11
3.2 Data Reduction	11
3.3 Uncertainty of Measurements	12
4.0 RESULTS AND DISCUSSION	
4.1 Presentation of Results	13
4.2 Effect of Variable Jet Temperature	15
4.3 Effect of Nozzle Divergence Half-Angle	22
4.4 Effect of Nozzle Exit-to-Throat Area Ratio	24
4.5 Effect of Strut Interference on Jet Simulation	26
4.6 Effect of Nozzle Base Area on Jet Simulation	27
5.0 CONCLUDING REMARKS	27
REFERENCES	30

ILLUSTRATIONS

Figure

1. Basic Model Dimensions and Location in Test Section	31
2. Model Installation in Tunnel 16T	32
3. Sketch of the Nozzle/Afterbody Configurations Tested	33
4. Sketch of Internal Nozzle Inserts for the Cold-Flow Configuration	36
5. Sketch of External Afterbody Contours for the Hot-Flow Convergent Nozzle Configuration and the Cold-Flow Configuration	38

<u>Figure</u>	<u>Page</u>
6. Variation of the Ratio of Specific Heats as a Function of Jet Total Temperature for Air and for the Products of 100-percent Ethylene/Air Combustion at $P_{t_j} = 14.7$ psia	40
7. Jet Temperature Effects on Afterbody Pressure Drag Coefficient for a Convergent Nozzle Geometry with Unseparated Afterbody Flow	41
8. Comparison of Quiescent MOC Jet Plume Boundaries Evaluated at Equal Drag Conditions with Jet Total Temperature as a Variable	52
9. Comparison of Quiescent MOC Jet Plume Boundaries at a Fixed Value of Δv with Jet Total Temperature as a Variable	53
10. Δv_{hot} for Equal Drag as a Function of Free-Stream Velocity at a $\Delta v_{cold} = 30$ deg	54
11. Jet Temperature Effects on Afterbody Pressure Drag Coefficient for a Convergent-Divergent Nozzle Geometry with Unseparated Afterbody Flow	55
12. Jet Temperature Effects on Afterbody Pressure Drag Coefficient for a Convergent Nozzle Geometry with Separated Afterbody Flow	59
13. Nozzle Divergence Angle Effects on Afterbody Pressure Drag Coefficient with Unseparated Afterbody Flow	70
14. Comparison of Quiescent MOC Jet Plume Boundaries Evaluated at Equal Drag Conditions with Nozzle Divergence Half-Angle as a Variable	73
15. Nozzle Exit-to-Throat Area Ratio Effects on Afterbody Pressure Drag Coefficient with Unseparated Afterbody Flow	74
16. Comparison of Quiescent MOC Jet Plume Boundaries Evaluated at Equal Drag Conditions with Nozzle Exit-to-Throat Area Ratio as a Variable	85

<u>Figure</u>	<u>Page</u>
17. Model Strut Interference Effects on the Jet Simulation Performance of Δv with Variable Jet Total Temperature	86
18. Model Strut Interference Effects on the Jet Simulation Performance of $(\Delta v)(A/A^*)$ with Variable Nozzle Exit-to- Throat Area Ratio	87
19. Nozzle Base Area Effects on Afterbody Pressure Drag Coefficient with Unseparated Afterbody Flow	88

TABLES

1. Model Configurations	90
2. Jet Simulation Parameter Performance for Variable Jet Total Temperature	91
3. Jet Simulation Parameter Performance for Variable Nozzle Exit-to-Throat Area Ratio	92
NOMENCLATURE	93

1.0 INTRODUCTION

A modern turbojet or turbofan engine, operating over a wide range of power settings, experiences vast changes in jet exhaust gas temperature. Matching the aerodynamic effects of these hot engine exhaust gases on a full-scale aircraft by wind tunnel testing a model incorporated with a burner has proved unreliable, time consuming, and uneconomical in the past. This has led to jet effects testing of models utilizing a cold high-pressure air jet to simulate the hot engine exhaust jet. Because of the large temperature differences between these two flows, no adequate means has yet been determined to accurately duplicate the jet interference of one by the other. This, in turn, has focused much effort in finding a jet simulation parameter whereby the aerodynamic effects produced by a hot engine exhaust gas could be matched by those of a cold high-pressure air jet.

The purpose of this investigation was to evaluate jet simulation parameters for correlating jet gas temperature effects on aircraft performance using integrated afterbody pressure drag as the measuring parameter for equal jet effects. Experimental data used to obtain the results reported herein were obtained from experiments (Refs. 1 and 2) of three strut-mounted, isolated nozzle/afterbody model configurations. Gas temperature effects on pressure drag were acquired for these tests by using high-pressure air or the products of ethylene/air combustion as the jet exhaust such that gas total temperature was varied from approximately 540 to 3,300°R. Jet simulation parameters were also evaluated in this investigation for changes in nozzle geometry since this is a variable which can alter the character of nozzle exhaust flow and thus influence jet interference. By utilizing high-pressure air as the jet exhaust gas, the jet effects of nozzle divergence half-angle were determined for half-angles from 0 to 10 deg, and the effects of nozzle exit area-to-throat area ratio were obtained for area ratios from 1.0 to approximately 1.5. The results presented in this report were obtained at Mach numbers from 0.6 to 1.5 and Reynolds numbers from 1.0×10^6 to 2.5×10^6 per foot.

One nozzle flow parameter investigated which is commonly used in wind tunnel testing for hot and cold jet simulation was nozzle total pressure ratio. Use of this parameter has usually been justified on the basis that the measured drag of a wind tunnel model with a cold high-pressure air jet will be higher, hence conservative, as compared to the drag produced by a similar model with a hot exhaust jet. Another parameter investigated was the exit static pressure ratio, which has been for many years a parameter to approximate when matching the effects of a highly underexpanded jet on the base region of a rocket. Other nozzle flow parameters considered in this study were mass flow flux, momentum flux, and kinetic energy flux, all of which were evaluated at the nozzle exit plane and which are used frequently in analyzing flow problems. Similarly, the parameter M_1 , the jet boundary Mach number, was evaluated since it is closely related to nozzle total pressure ratio. Jet boundary or jet plume shape parameters investigated include Δv , or the incremental change in Prandtl-Meyer angle and the related parameter δ_j or initial jet inclination angle which includes the nozzle divergence half-angle ($\delta_j = \Delta v + \theta_N$). Love in Ref. 3 concluded that, for slightly underexpanded jets (P_j/P_∞ from 1 to 10), good boundary simulation was obtained if the jet inclination angle was matched. Other investigators (Ref. 4) have determined that if either M_1/γ or $\gamma M_1^2/\beta_1$ are matched simultaneously with jet inclination angle, good jet boundary simulation is achieved over a wide range of underexpanded jet exhaust flows. However, it should be noted that to match M_1/γ or $\gamma M_1^2/\beta_1$ with δ_j for differing jet flows, requires that each flow have a different jet boundary Mach number, M_1 (a function of nozzle total pressure ratio), and a different jet exit Mach number, M_j (a function of nozzle internal geometry). Since for nozzle/afterbody performance testing, it is impractical to vary nozzle internal geometry and nozzle total pressure ratio simultaneously, this investigation evaluated M_1/γ and $\gamma M_1^2/\beta_1$ as jet simulation parameters independent of δ_j . One final jet plume simulation parameter investigated was $\gamma M_1/\beta_1$ which was developed in the course of this study.

2.0 APPARATUS

2.1 TEST FACILITY

Tunnel 16T is a closed-circuit, continuous-flow wind tunnel capable of operating at Mach numbers from 0.2 to 1.6 within a stagnation pressure range from approximately 120 to 4,000 psfa, depending on the Mach number, and over a stagnation temperature range from about 80°F to a maximum of 160°F. The specific humidity of the air is controlled by removing tunnel air and supplying conditioned makeup air from an atmospheric drier.

2.2 TEST ARTICLE AND SUPPORT SYSTEM

Data for this investigation were obtained from experiments of three different model configurations. These configurations were all modifications of the same basic model design. The basic design was an existing isolated axisymmetric nozzle/afterbody model with a 14-deg half-angle conical nose and a maximum body diameter of 9.86 in. A boundary-layer trip consisting of 0.55-in.-diam steel spheres spot-welded to a trip ring at a circumferential spacing of four sphere diameters was located 12 in. aft of the cone vertex. For all three configurations, the model was mounted on a tapered strut with an average aft sweep of 35 deg. The strut thickness-to-chord ratio varied from 0.53 at the model to 0.88 at the tunnel floor. The maximum cross-sectional area of the model/strut arrangement was equivalent to 0.88 percent of the wind tunnel test section cross-sectional area.

The model configurations consisted of two hot-flow configurations, each with an ethylene/air combustor, and one cold-flow configuration utilizing high-pressure air as the jet exhaust gas. One hot-flow configuration had a convergent-divergent nozzle, and a more complete description

of this configuration may be found in Ref. 1. A description of the other two configurations, a hot-flow configuration with a convergent nozzle and a cold-flow configuration with variable internal nozzle geometry may be found in Ref. 2. Minor differences existed in the overall model lengths among the three configurations because of differences in individual external afterbody and internal nozzle geometry. The basic dimensions of each of the configurations are presented in Table 1. A sketch and installation photograph representative of all three configurations except for individual differences in model length is shown, respectively, in Figs. 1 and 2. A sketch of the internal nozzle assembly for each of the model configurations is shown in Fig. 3, and a sketch of the various internal nozzle inserts for the cold-flow configuration is presented in Fig. 4. Although exit-to-throat area ratio and the divergence half-angle were varied for the cold-flow configuration, nozzle exit area was fixed. Both the hot-flow convergent nozzle and the cold-flow configurations shared a common external afterbody geometry with a 15-deg boattail angle. A 25-deg boattail was also tested with the hot-flow convergent nozzle configuration. A dimensional sketch of these two boattail geometries is shown in Fig. 5.

2.3 INSTRUMENTATION

Rows of static pressure orifices were located along the nozzle afterbody and boattail surfaces at top, bottom, and side circumferential stations for all three model configurations. Pressure measurements were made utilizing a single differential pressure transducer per pressure orifice with a transducer range of ± 5 psid. The external instrumentation was common for the hot-flow convergent nozzle configuration and the cold-flow configuration with the 15-deg boattail installed. The 15-deg boattail had approximately 29 pressures on the top row and 24 pressures on the bottom row. Air and/or ethylene flow rates were determined from pressure, temperature, and area measurements in critical-flow venturi metering sections external to each model configuration. A more

complete description of the instrumentation for the hot-flow convergent-divergent nozzle configuration may be found in Ref. 1 and for the hot-flow convergent nozzle, and cold-flow configurations may be found in Ref. 2.

3.0 PROCEDURE

3.1 TEST CONDITIONS AND TECHNIQUES

The data in this report are presented at nominal free-stream Mach numbers of 0.6, 0.9, 1.1, and 1.5 at free-stream Reynolds numbers from 1.0×10^6 per foot to 2.5×10^6 per foot. The data were obtained at an angle of attack of zero degree for all three model configurations. Nozzle total pressure ratio for these results was varied from a jet-off condition to a maximum of 22 depending on the free-stream Mach number.

3.2 DATA REDUCTION

The primary parameter presented in this report to measure jet interference was integrated afterbody pressure drag coefficient. This drag coefficient was based on a maximum model cross-sectional area of approximately 76 in.² for all three model configurations and was determined by numerically integrating the top centerline pressure distribution on nozzle afterbody and boattail model surfaces. It represented the pressure drag on the nozzle afterbody and boattail projected area aft of model station, MS 135.47 in. for the hot-flow convergent-divergent nozzle configuration and aft of model station, MS 130.47 in. for the hot-flow convergent nozzle and the cold-flow configurations. A similar drag coefficient was determined based on the bottom centerline pressure distribution but was used only to evaluate strut interference effects on jet simulation parameter performance.

The internal flow properties, i.e. the jet stagnation conditions, were calculated using one-dimensional isentropic flow relations, measured areas and the measured static pressure in the flow duct ahead of the nozzle throat. The ratio of specific heats for the hot jet was calculated using the theoretical total temperature for complete combustion of an ethylene/air mixture. The variation of the specific heat ratio with temperature for the products of ethylene/air combustion and for heated air is shown in Fig. 6. It can be seen, for example, that the difference in using air alone versus complete combustion would only amount to a 2.35-percent error in the ratio of specific heats at 3,300°R. Therefore, using a combustion efficiency of 100 percent introduces little error in determining the ratio of specific heats (the combustion efficiency was determined to be nominally 80 percent).

A more complete description of the data reduction procedures for the hot-flow convergent-divergent nozzle configuration may be found in Ref. 1 and for the hot-flow convergent nozzle and cold-flow configurations in Ref. 2.

3.3 UNCERTAINTY OF MEASUREMENTS

Typical uncertainty values for the measured tunnel and model parameters presented in this report may be found in Ref. 2.

4.0 RESULTS AND DISCUSSION

In conducting aerodynamic wind tunnel tests, simulating the hot nozzle exhaust jet of a full-scale aircraft is usually accomplished by means of a cold high-pressure air jet. This technique has been developed for a variety of reasons, among which include the prohibitive high cost and complexity associated with constructing and testing of a model with a burner. However, by using cold-flow techniques, a problem has arisen in that no completely satisfactory method of duplicating the aerodynamic

interference produced by a hot nozzle exhaust jet has been formulated. The objective of this investigation was to evaluate various jet simulation parameters in an attempt to establish a method of matching hot jet interference with cold jet flows. Successful parameters would correlate integrated afterbody pressure drag which is a measurement of the aerodynamic interference for jet flows of varying total temperature. In addition, since most modern aircraft engines operate with variable internal nozzle geometry which also influences the character of the jet flow issuing from a nozzle, this investigation was conducted to determine the jet effects introduced by varying internal nozzle geometry and to obtain jet simulation parameters to correlate these effects.

4.1 PRESENTATION OF RESULTS

The nature of jet interference on nozzle/afterbody performance has been described by Bergman in Ref. 5 and Compton in Ref. 6 to be composed of two dissimilar effects, the effect of jet plume blockage and the effect of jet entrainment. The effect of jet plume blockage occurs as the free-stream flow over the afterbody attempts to negotiate the plume boundary produced by the exhausting jet flow from the nozzle. As the jet plume boundary increases in size, this blockage increases and compresses the flow over the afterbody producing a decrease in the integrated pressure drag. The jet entrainment, a function of the mixing that results between the free-stream flow over the afterbody and the nozzle jet flow, acts in an opposing manner as compared to that displayed by jet plume blockage. Jet entrainment tends to lower the pressure on the afterbody surfaces by accelerating the flow which in turn increases integrated pressure drag.

The present investigation evaluated parameters that have been used in the past for simulation of jet plume boundaries and aerodynamic interference on afterbodies and those which should have some relation

to the effectiveness of the jet entrainment on the free-stream flow. A few parameters were formulated during the course of this study which give some degree of data correlation of specific experimental conditions. The performance of all these parameters as jet simulation parameters was based on their degree of correlation of pressure drag coefficient data for differing nozzle flows. For most results shown herein, drag coefficient represents that determined from integration of the top row of afterbody pressures where the effects of model strut interference are minimized. However, a small portion of this study was devoted to examining the effects of model strut interference on jet simulation utilizing integrated afterbody drag results determined from the bottom row of afterbody pressures.

The following list is a summary of the parameters evaluated for the exhaust flow conditions established during this investigation. The discussion of the results which follows gives an indication of the success of these parameters as jet simulation parameters.

$NPR = P_{t_j}/P_\infty$	Nozzle total pressure ratio
P_j/P_∞	Nozzle exit static pressure ratio
$(\rho V)_j$	Jet mass flow flux at nozzle exit
$(\rho V^2)_j$	Jet momentum flux at nozzle exit
$(\rho V^3)_j$	Jet kinetic energy flux at nozzle exit
$M_1 = \left(\frac{2}{\gamma-1}\right) \sqrt{\left[\left(P_{t_j}/P_\infty\right)^{\frac{\gamma-1}{\gamma}} - 1\right]}$	Jet boundary Mach number when expanded to free-stream static pressure ratio
$\gamma M_1/\beta_1$	Jet boundary matching parameter

$\gamma M_1^2 / \beta_1$	Jet boundary matching parameter
M_1 / γ	Jet boundary Mach number corrected for specific heat ratio
$P_j / \gamma P_\infty$	Nozzle exit static pressure ratio corrected for specific heat ratio
$\Delta v = (v_1 - v_j)$	Incremental change in Prandtl-Meyer angle when expanded from nozzle exit conditions to free-stream conditions
$\delta_j = (\Delta v + \theta_N)$	Initial jet inclination angle when expanded from the nozzle exit conditions to free-stream conditions
$(\Delta v) (A/A^*)$	Incremental Prandtl-Meyer angle corrected for nozzle exit-to-throat area ratio
$(P_j / \gamma P_\infty) (A/A^*)$	Nozzle exit static pressure ratio corrected for specific heat ratio and nozzle exit-to- throat area ratio

4.2 EFFECT OF VARIABLE JET TOTAL TEMPERATURE

4.2.1 Convergent Nozzle Results with an Unseparated Boattail

In Fig. 7, integrated afterbody pressure drag data are presented for underexpanded hot and cold jet flows issuing from a convergent, sonic nozzle (configuration HF1). The jet flows, as shown, encompass total temperatures from 540 to 3,300°R and span a significantly wider nozzle total pressure ratio range than commonly experienced by a turbofan or turbojet engine. The results are presented at free-stream Mach numbers of 0.9 and 1.5, respectively. The afterbody external geometry

for these results was a 15-deg boattail geometry which had a gently sloping contour. The analysis reported in Ref. 2 concluded that, in general, there was no indication of separation of the flow over this afterbody.

By matching nozzle total pressure ratio as shown in Fig. 7, large errors in drag result between cold and hot underexpanded jet flows. Cold jet drag as a function of nozzle total pressure ratio is higher compared to that displayed by a hot jet for both subsonic and supersonic free-stream Mach numbers. The differences between cold and hot jet drag coefficient become larger as gas total temperature differences increase and as nozzle total pressure ratio increases. As shown, the drag differences are smaller for a given nozzle total pressure ratio value at a supersonic free-stream Mach number of 1.5 as compared to a subsonic free-stream Mach number of 0.9. Corresponding drag errors as displayed by nozzle total pressure ratio are introduced by matching the nozzle flow parameters of exit static pressure ratio, exit mass flow flux, exit momentum flux, jet boundary Mach number, and $\gamma M_1^2 / \beta_1$. The parameter $\gamma M_1 / \beta_1$ displays no better jet simulation and provides higher hot jet drag than cold jet drag when duplicated. Exit kinetic energy flux appears to correlate hot to hot jet drag data, but like $\gamma M_1 / \beta_1$ gives higher hot jet drag than cold jet drag when duplicated.

Some jet simulation is achieved at underexpanded nozzle flow conditions by matching the parameters M_1 / γ , $P_j / \gamma P_\infty$, and Δv . As shown in Fig. 7i, hot jet drag is slightly higher than cold jet drag when M_1 / γ is matched except for jet flows corresponding to near nozzle design conditions. For these jet flows, cold jet drag is higher when M_1 / γ is matched. By duplicating $P_j / \gamma P_\infty$, cold jet drag is higher than hot flow drag for all nozzle conditions corresponding to design nozzle total pressure ratios and greater. When the parameter Δv is duplicated, no orderly consistent drag trend by jet gas total temperature is evident at underexpanded nozzle flow conditions; however, at nozzle design

conditions, cold jet drag is higher than that demonstrated by a hot jet for this parameter. Like nozzle total pressure ratio, the parameters $P_j/\gamma P_\infty$ and Δv demonstrate less hot and cold drag errors when duplicated at supersonic free-stream Mach numbers than at subsonic free-stream Mach numbers. Conversely, the parameter M_1/γ gives better hot and cold jet drag correlation at subsonic free-stream conditions as compared to that obtained supersonically. It should be further noted for these results that δ_j or the initial jet inclination angle provides the same jet simulation as demonstrated by Δv since for a convergent nozzle geometry they are equivalent parameters.

At a free-stream Mach number of 0.9, all three parameters just discussed give hot and cold jet simulation within 40 drag counts based on maximum cross-sectional area for underexpanded nozzle flows up to a gas total temperature of approximately 1,700°R ($\gamma = 1.330$). This temperature corresponds to a typical turbojet or turbofan exit gas total temperature at a subsonic cruise power setting. Jet simulation within approximately 30 drag counts is realized at a free-stream Mach number of 1.5 by matching any of these three parameters except M_1/γ for underexpanded nozzle flows ranging in total temperature from 540°R ($\gamma = 1.400$) to 3,300°R ($\gamma = 1.275$). This range of temperatures typically span those of an aircraft engine between a low power setting and a maximum afterburning power setting.

A comparison of the hot and cold jet simulation performance of all of the parameters thus far discussed is presented in Table 2. Drag increments between hot and cold jets (gas total temperatures corresponding to 3,300 and 540°R, respectively) are shown for each parameter when duplicated. Nozzle flows corresponding to the maximum drag condition for the cold jet and to a condition above nozzle design pressure ratio are those at which the jet simulation performance comparisons were made. The results agree, in general, with those previously established with the parameters M_1/γ , $P_j/\gamma P_\infty$, and Δv providing the best correlation at underexpanded jet conditions.

Analysis of underexpanded quiescent MOC jet plume boundaries presented in Fig. 8 indicates that neither jet plume shape nor jet plume blockage is necessarily duplicated for equal drag producing hot and cold jets. These boundaries were computed based on values of nozzle total pressure ratio, ratio of specific heats, nozzle exit-to-throat area ratio, and nozzle divergence half-angle at a nearly fixed value of pressure drag coefficient. As shown, jet plume shape is essentially constant in size and curvature for cold and hot nozzle flows up to a gas total temperature of approximately $2,400^{\circ}\text{R}$ ($\gamma = 1.300$). However, as noted, above this temperature, a significantly larger cold jet plume boundary is required to provide the same jet interference as exhibited by a hot jet plume boundary corresponding to a temperature of $3,300^{\circ}\text{R}$ ($\gamma = 1.275$). This indicates that a hot jet produces greater interaction between the plume and free-stream than a cold jet and that jet plume shape alone is not the only factor which must be considered in the duplication of hot jet drag by a cold flow.

In Fig. 9, it is shown that by duplicating Δv , jet plume shape is essentially matched for flows of variable jet total temperature. This indicates that Δv , at least for these results, is perhaps a measure of jet plume shape. From this, it can be implied that if hot and cold jet drag were a function of jet plume shape alone, the parameter Δv in itself would provide excellent jet simulation. However, as shown in Fig. 10, when afterbody pressure drag is duplicated for jet flows with large temperature differences ($T_{t_j} = 3,300^{\circ}\text{R}$ versus $T_{t_j} = 540^{\circ}\text{R}$), a significant discrepancy in hot and cold jet plume shape as measured by Δv is observed. The magnitude of this discrepancy in jet plume shape indicates differences in jet interaction between the plume and free stream for equal drag producing hot and cold jets. The largest differences in jet plume shape occur at subsonic free-stream velocities. At these conditions, a significantly larger cold jet plume is required to produce the same jet interference as realized by a hot jet plume. As free-stream velocity is increased to supersonic conditions, hot and

cold jet plume shapes are essentially equivalent in size. At these conditions, jet plume shape appears to be the governing jet interference producing agent for both hot and cold jet flows.

convergent nozzle

From all of these results, it can be generally concluded that matching jet plume shape alone is not sufficient in duplicating hot and cold jet interference for slightly underexpanded jet flows, subsonic free-stream velocities, and for large discrepancies in hot and cold jet temperature. However, simulating jet plume shape is important in duplicating hot and cold jet interference for highly underexpanded jet flows, supersonic free-stream velocities, and for small differences in hot and cold jet temperature.

4.2.2 Convergent-Divergent Nozzle Results with an Unseparated Boattail

In Fig. 11 integrated afterbody pressure drag data are presented for hot and cold jet flows issuing from a model configuration with a convergent-divergent nozzle (configuration HF2). The afterbody geometry of this configuration was not a 15-deg boattail as just previously shown; however, it had a gentle sloping contour such that little or no separation of afterbody flow was suspected. The drag results are shown as a function of nozzle total pressure ratio and the three parameters, $P_j/\gamma p_\infty$, M_1/γ , and δ_j (or Δv). These parameters provided the best hot and cold jet interference correlation for the previously presented convergent nozzle drag data. The results are shown at free-stream Mach numbers from 0.6 to 1.5 for moderately underexpanded jet flows of varying total temperature.

As shown in Fig. 11, large errors in drag result between hot and cold jet flows by matching nozzle total pressure ratio. This drag trend is similar to that observed for the previously shown HF1 configuration drag data, where cold jet pressure drag as a function of nozzle total pressure ratio is higher compared to that displayed by a hot jet for

all Mach numbers presented. The present results, however, show a much better drag correlation by duplication of the parameters $P_j/\gamma P_\infty$, M_1/γ , and δ_j than observed for the HF1 configuration results. Again, it should be noted that the parameter Δv which represents the incremental change in Prandtl-Meyer angle gives similar jet simulation as δ_j since these parameters differ only by a constant, the nozzle divergence half-angle, when the internal nozzle geometry is fixed. Since it has been shown previously that Δv provides hot and cold jet plume boundary simulation by comparison of hot and cold MOC plume shapes, it can be concluded for these results that consistent drag duplication was achieved for hot and cold underexpanded jet flows by matching jet plume shape. These results thus indicate that better hot and cold jet simulation was provided by matching jet plume boundary shape for jet flows issuing from a convergent-divergent nozzle than for similar flows issuing from a convergent nozzle.

4.2.3 Convergent Nozzle Results with a Separated Boattail

In Fig. 12, hot and cold integrated afterbody drag coefficient data are presented at free-stream Mach numbers of 0.9 and 1.5 for an afterbody with a 25-deg boattail angle and with a convergent nozzle internal geometry (Configuration HF1). From results obtained in Ref. 2, the 25-deg boattail demonstrated separated flow at Mach number 1.5; however, it was suspected that this existed for all free-stream Mach numbers down to and including Mach number 0.6. These data are presented as a function of the same parameters as were the data for the 15-deg boattail with the convergent nozzle.

For the various parameters previously examined, the afterbody drag coefficient data for the 25-deg boattail exhibit similar trends with gas total temperature as noted for the 15-deg boattail. However, the 25-deg boattail drag results show unusual drag characteristics for both hot and cold jets at slightly underexpanded nozzle conditions. At these conditions, particularly at subsonic Mach numbers ($M_\infty = 0.9$ presented),

drag increases as the jet flow becomes increasingly underexpanded. This trend continues only until a certain underexpanded jet flow condition is achieved, at which point drag reaches a maximum. As compared to the results from the 15-deg boattail, it can be seen that a higher underexpanded flow is required for the 25-deg boattail to achieve a maximum drag condition. This can probably be attributed to the large separated region on the 25-deg boattail which prohibits any significant recompression on the afterbody or any decrease in drag until a large jet plume boundary, perhaps as large as the separated region on the boattail, is produced.

As a function of nozzle total pressure ratio, cold jet drag is higher than hot jet drag for both subsonic and supersonic free-stream conditions for the 25-deg boattail. These results show larger hot and cold jet drag errors at subsonic free-stream conditions and for slightly underexpanded nozzle flows than experienced on the 15-deg boattail. As noted similarly for the 15-deg boattail results, a higher cold jet drag can be linked to differences in plume and free-stream interaction exhibited by a cold jet as compared to a hot jet.

The parameter $(\rho V)_j$ appears to provide some degree of jet simulation at subsonic free-stream conditions for slightly underexpanded jet flows. This indicates that the differences in hot and cold plume-free stream interaction at these conditions is a function of mixing between the two flows and perhaps represents differences in hot and cold jet entrainment.

At subsonic free-stream conditions, no jet simulation is achieved by duplicating Δv ; however, at supersonic free-stream conditions and for highly underexpanded jet flows, typically higher than those at which a turbofan or turbojet engine operate, good drag correlation is achieved by matching Δv for both hot and cold jets. These trends agree well with those observed for the HF1 configuration with the 15-deg boattail where it was concluded that duplicating jet plume

shape represented by Δv is more important in achieving hot and cold jet simulation as free-stream velocity increases, as jet flow becomes increasingly underexpanded and as hot and cold jet temperature differences decrease.

4.3 EFFECT OF NOZZLE DIVERGENCE HALF-ANGLE

Afterbody pressure drag coefficient data for the 15-deg boattail are presented in Fig. 13 as a function of various nozzle flow and jet plume shape parameters with nozzle divergence half-angle as a variable (Configuration CF1). The data are shown at Mach numbers 0.9 and 1.5 for three internal nozzle inserts with respective nozzle divergence half-angles of 2.5, 5, and 10 deg and with a similar fixed nozzle exit-to-throat area ratio of 1.22. As for the HF1 configuration, they span a significantly wider range of underexpanded jet flows than typically experienced by a modern aircraft engine. The general internal geometry of this nozzle configuration is representative of a full-scale aircraft engine at a reheat power setting.

In Fig. 13, good pressure drag duplication is achieved for moderately underexpanded jet flows by matching the nozzle total pressure ratio for variable divergence half-angle. This duplication is maintained as the jet flows become increasingly underexpanded and as a drag decrease is observed. Similar jet simulation can be realized by matching the nozzle flow parameters of exit static pressure ratio, exit mass flow flux, exit momentum flux, exit kinetic energy flux, and the jet expansion Mach number. Like results can also be obtained by matching the jet plume shape parameters $\gamma M_1/\beta_1$, $\gamma M_1^2/\beta_1$, and Δv . All of these parameters exhibit equivalent correlation of the drag coefficient data as compared to NPR because they are but a function of NPR and of one or a combination of the configuration constants exit-to-throat area ratio, ratio of specific heats, and nozzle gas total temperature. The only parameter investigated which fails to provide jet simulation for variable

nozzle divergence half-angle is the parameter δ_j or the initial jet inclination angle. As shown in Fig. 13, at a constant drag coefficient value and at underexpanded jet conditions, the difference in δ_j between any two nozzle geometries corresponds to the difference in nozzle divergence half-angle between these two geometries. Since δ_j is but a function of Δv , a parameter which correlates these jet drag data, and the divergence half-angle, it can be concluded that the lack of success of this parameter in providing jet simulation can be attributed to the variation of divergence half-angle.

In Fig. 13, at a free-stream Mach number of 1.5 and for jet flows which correspond to those near nozzle design conditions ($NPR \approx 4$ for $A/A^* \approx 1.22$), pressure drag coefficient becomes larger as divergence half-angle becomes larger. It should be noted that at near nozzle design conditions jet plume shape is essentially cylindrical in shape and the jet flow exits the nozzle at approximately the same static pressure as that of the free-stream flow. This leaves only the divergence half-angle to produce any jet flow deflection from the nozzle and thus any jet interference.

In Fig. 14, theoretical MOC jet plume boundaries at quiescent free-stream conditions are presented for underexpanded jet flows with nozzle divergence half-angle as a variable. They typify jet plume shapes of a modern aircraft engine at a supersonic free-stream Mach number and at a reheat power setting. As shown for equal drag (which also corresponds to equal NPR from previous discussion), jet plume shape is duplicated for underexpanded nozzle flows regardless of divergence half-angle. Duplication is achieved from the nozzle exit to at least three nozzle radii downstream of the nozzle exit. Since matching nozzle total pressure ratio represents matching jet plume shape as well as matching any of the various flow parameters such as jet exit mass flow flux, jet exit momentum flux, etc., it can perhaps be established that both jet entrainment and jet plume shape duplication is achieved by matching NPR for underexpanded flows where divergence half-angle is a variable.

4.4 EFFECT OF NOZZLE EXIT-TO-THROAT AREA RATIO

In Fig. 15, integrated afterbody pressure drag coefficient data are shown at free-stream Mach numbers of 0.9 and 1.5 for high-pressure air jet flows issuing from nozzles of differing exit-to-throat area ratios and from an unseparated (15-deg) external boattail geometry (configuration CF1). The area ratios presented vary from 1.000 to 1.475 and span the range of operational area ratios for a turbojet or turbofan engine in the course of going from a low to a maximum power setting. For the results shown, the parameters evaluated are those for which good jet simulation has been indicated for variable divergence half-angle at underexpanded jet flow conditions (all except δ_j). As before, these results encompass a wider range of underexpanded jet flow conditions than typically experienced by a modern aircraft engine.

In Fig. 15 for underexpanded jet flows, higher drag is realized at a given nozzle total pressure ratio value as exit-to-throat area ratio becomes greater. This drag discrepancy becomes larger as jet flows become increasingly underexpanded. The increase in drag with increasing area ratio can best be explained if jet plume shape is assumed to be the mechanism by which jet interference is produced for underexpanded jet flows. As nozzle exit-to-throat area ratio increases, less jet expansion is experienced externally and more occurs internally to a nozzle. A smaller external jet expansion results in a smaller jet plume boundary and, in conclusion, provides less plume blockage and higher afterbody drag.

Similar drag errors, as obtained by matching nozzle total pressure ratio, are noted by matching the nozzle flow parameters of jet expansion Mach numbers and exit mass flow flux, exit momentum flux, and exit kinetic energy flux. Corresponding results are displayed by matching the jet plume shape parameters $\gamma M_1/\beta_1$ and $\gamma M_1^2/\beta_1$. An opposing drag trend as that provided by matching nozzle total pressure ratio is

obtained by duplicating either of the parameters P_j/p_∞ or Δv . By matching either of these, pressure drag coefficient decreases as area ratio increases. Large drag discrepancies by matching these two parameters are noted between differing area ratios as the jet flows become increasingly underexpanded. If jet plume shape is the dominating factor which influences underexpanded jet drag correlation, it can be deduced that neither Δv nor P_j/p_∞ provide the necessary jet simulation capabilities when exit-to-throat area ratio is varied.

In Fig. 15, excellent drag duplication is achieved for underexpanded jet flows by matching the parameters $(P_j/\gamma p_\infty)(A/A^*)$ and $(\Delta v)(A/A^*)$. These parameters are similar to those for which jet simulation was provided for underexpanded hot and cold jet drag results; however, these parameters are both corrected for exit-to-throat area ratio. Since the area ratio changes for this configuration were accomplished by increasing or decreasing the throat area at an essentially fixed exit area, these parameters seem to provide a nozzle throat area size correction to size of the jet plume boundary.

The results in Fig. 15 show that for any of the parameters which are duplicated, appreciable drag errors are experienced for jet flows near nozzle design conditions issuing from nozzles of differing exit-to-throat area ratio. As shown, drag is higher with increasing area ratio for both subsonic and supersonic free-stream flows. Since at nozzle design conditions jet plume shape is essentially cylindrical, it is difficult to ascertain the reasons for differences in drag at these conditions unless jet entrainment effects are different and predominate.

A comparison of jet simulation parameter performance in correlating area ratio effects is presented in Table 3. Two nozzle flow conditions, one near that of nozzle design and one at an underexpanded jet condition, were chosen to make the evaluation. In general, the trends are as previously discussed with the parameters $(\Delta v)(A/A^*)$ and $(P_j/\gamma p_\infty)(A/A^*)$ providing the best correlation for underexpanded jet flows.

In Fig. 16, underexpanded MOC quiescent jet plume shapes are presented at constant drag values for nozzles of differing area ratio. These plume shapes are representative of those produced by a modern aircraft engine between a cruise and maximum afterburning power setting. The results show that, for equal drag, jet plume shape is closely duplicated for at least three nozzle radii downstream of the exit for variable nozzle exit-to-throat area ratio. This stresses the importance of matching jet plume shape or jet plume blockage in providing equal jet interference for underexpanded jet flows from nozzles of differing area ratio.

4.5 EFFECT OF STRUT INTERFERENCE ON JET SIMULATION

In Figs. 17 and 18, integrated afterbody pressure drag coefficient data are presented which were obtained by integration of the bottom row of centerline afterbody and boattail pressures located directly downstream of the model support strut. These results were obtained with the unseparated (15-deg) boattail installed at Mach numbers 0.9 and 1.5 for the HF1 and the CF1 configurations. As shown, the drag coefficient data are displayed as a function of the parameters which provided the best correlation of the drag coefficient data representative of the top row of boattail pressures.

The data from Figs. 17 and 18, respectively, indicate that strut interference does not influence the performance of the jet simulation parameter Δv in correlating hot and cold jet drag results or $(\Delta v)(A/A^*)$ in correlating jet drag from nozzles of differing exit-to-throat area ratios. These parameters provide as good a jet simulation as demonstrated for the previous integrated drag results from the top row of pressures where strut interference was negligible. These results show that if the support strut used for this model is compared to an aircraft wing, it can be concluded that wing interference does not affect the jet interference duplication achieved on the afterbody by matching the above parameters.

4.6 EFFECT OF NOZZLE BASE AREA ON JET SIMULATION

In Fig. 19, integrated afterbody pressure drag coefficient data for underexpanded cold jet flows are shown for both the HF1 configuration which had a large base area as a result of combustor cooling requirements and the CF1 configuration which was installed with a sonic nozzle insert which had a relatively small base area. Both model configurations are presented at a free-stream Mach number of 0.9 utilizing the same unseparated (15-deg) external afterbody geometry.

As shown, for both model configurations, drag decreases with increasing underexpansion of the jet flow. These results further show that a higher drag is exhibited for the HF1 configuration with the large base area by duplicating NPR or Δv . As a result of a larger base area, the diameters of both the nozzle exit and thus the jet plume boundary are smaller. This yields a smaller jet plume blockage and thus higher drag for the nozzle with the large base area. As shown, modification of the parameter NPR by the nozzle exit-to-total base area ratio gives jet simulation agreement within approximately 40 drag counts based on maximum model cross-sectional area. However, similar modification of the parameter Δv does not yield good drag correlation results.

5.0 CONCLUDING REMARKS

The objective of this investigation was to evaluate jet simulation parameters that would correlate integrated afterbody pressure drag for jet flows of variable gas total temperature and for jet flows issuing from nozzles of variable internal geometry. Data were utilized from previous experiments conducted with three different isolated nozzle/afterbody configurations where gas total temperature was varied from 540 to 3,300°R, nozzle exit-to-throat area ratio was varied from 1.000 to 1.475, and nozzle divergence half-angle was varied from 0 to 10 deg. The significant results and conclusions obtained may be summarized as follows:

1. Significant afterbody drag differences are present between hot and cold jets at the same nozzle total pressure ratio (NPR) regardless of internal or external nozzle geometries. These differences are generally larger for subsonic free-stream conditions at pressure ratios above the nozzle design pressure ratio and are larger for a separated external afterbody geometry as compared to an unseparated afterbody geometry. At the nozzle design pressure ratio, differences in hot and cold drag by duplication of NPR are about the same regardless of free-stream Mach number.
2. Correlation parameters that characterize the inviscid jet plume boundary provide significantly better hot and cold jet simulation than NPR (roughly a factor of 4) for nozzle total pressure ratios above that of nozzle design. The best jet simulation with these parameters is realized at supersonic free-stream Mach numbers.
3. Inviscid plume shape parameters provided better hot and cold drag correlation for unseparated afterbody flows; however, correlation was achieved with these parameters for a separated afterbody when the jet flow was sufficiently underexpanded such as to fill the wake region.
4. No parameters that were investigated appeared to correlate the hot and cold drag coefficient data at nozzle design conditions any better than nozzle total pressure ratio.
5. Afterbody drag is essentially independent of nozzle divergence angle when nozzle total pressure ratio is duplicated for underexpanded jet flows and for unseparated boattail flows.

6. The use of the initial jet inclination angle ($\delta_j = \Delta v + \theta_N$), a correlation parameter, spreads the drag data apart by an amount equal to the difference in the nozzle divergence half-angle (θ_N) between any two nozzle geometries.
7. With θ_N as a variable, all parameters investigated except initial jet inclination angle provided as good a jet simulation at underexpanded jet flow conditions as nozzle total pressure ratio. These parameters in essence were a function of the variable nozzle total pressure ratio and various constants including specific heat ratio, gas total temperature, and nozzle exit-to-throat area ratio.
8. Afterbody drag becomes higher at a given nozzle total pressure ratio as nozzle exit-to-throat area ratio is increased for unseparated afterbody flows. This drag trend with NPR is essentially the same for both subsonic and supersonic free-stream Mach numbers.
9. With area ratio as a variable, the inviscid plume shape parameter Δv and the parameter $P_j/\gamma p_\infty$ modified by including the area ratio, e.g., $(\Delta v)(A/A^*)$ and $(P_j/\gamma p_\infty)(A/A^*)$, produced good data correlation at nozzle total pressure ratios above the nozzle design pressure ratio. Fair correlation with these parameters was obtained near the design pressure ratio for supersonic free-stream Mach numbers.

REFERENCES

1. Robinson, C. E. and High, M. D. "Exhaust Plume Temperature Effects on Nozzle Afterbody Performance over the Transonic Mach Number Range." AEDC-TR-74-9 (AD781377), July 1974.
2. Galigher, Lawrence L., Yaros, S. F., and Bauer, R. C. "Evaluation of Boattail Geometry and Exhaust Plume Temperature Effects on Nozzle Afterbody Drag at Transonic Mach Numbers." AEDC-TR-76-102, October 1976.
3. Love, E. S., et al. "Experimental and Theoretical Studies of Axisymmetric Free Jets." NASA TR R-6, 1959.
4. Herron, R. D. "Jet-Boundary Simulation Parameters for Uncerexpanded Jets in a Quiescent Atmosphere." Journal of Spacecraft and Rockets, Vol. 5, No. 10, October 1968, pp. 1155-1160.
5. Bergman, D. "Effects of Engine Exhaust Flow on Boattail Drag." Journal of Aircraft, Vol. 8, No. 6, June 1971, pp. 434-439.
6. Compton, W. B. "An Experimental Study of Jet Exhaust Simulation." NASA TM X-71975, June 1974.

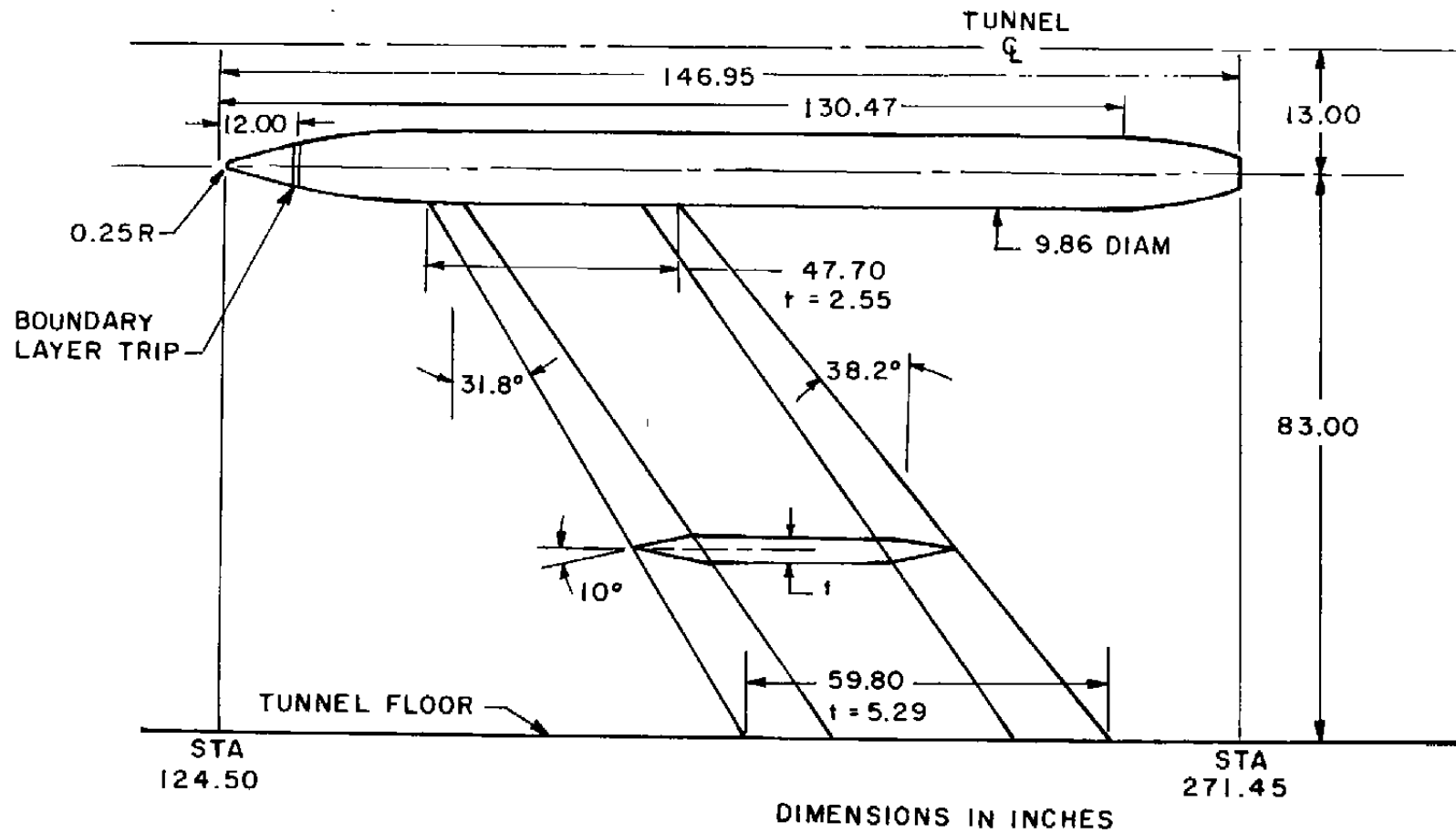


Figure 1. Basic model dimensions and location in test section.

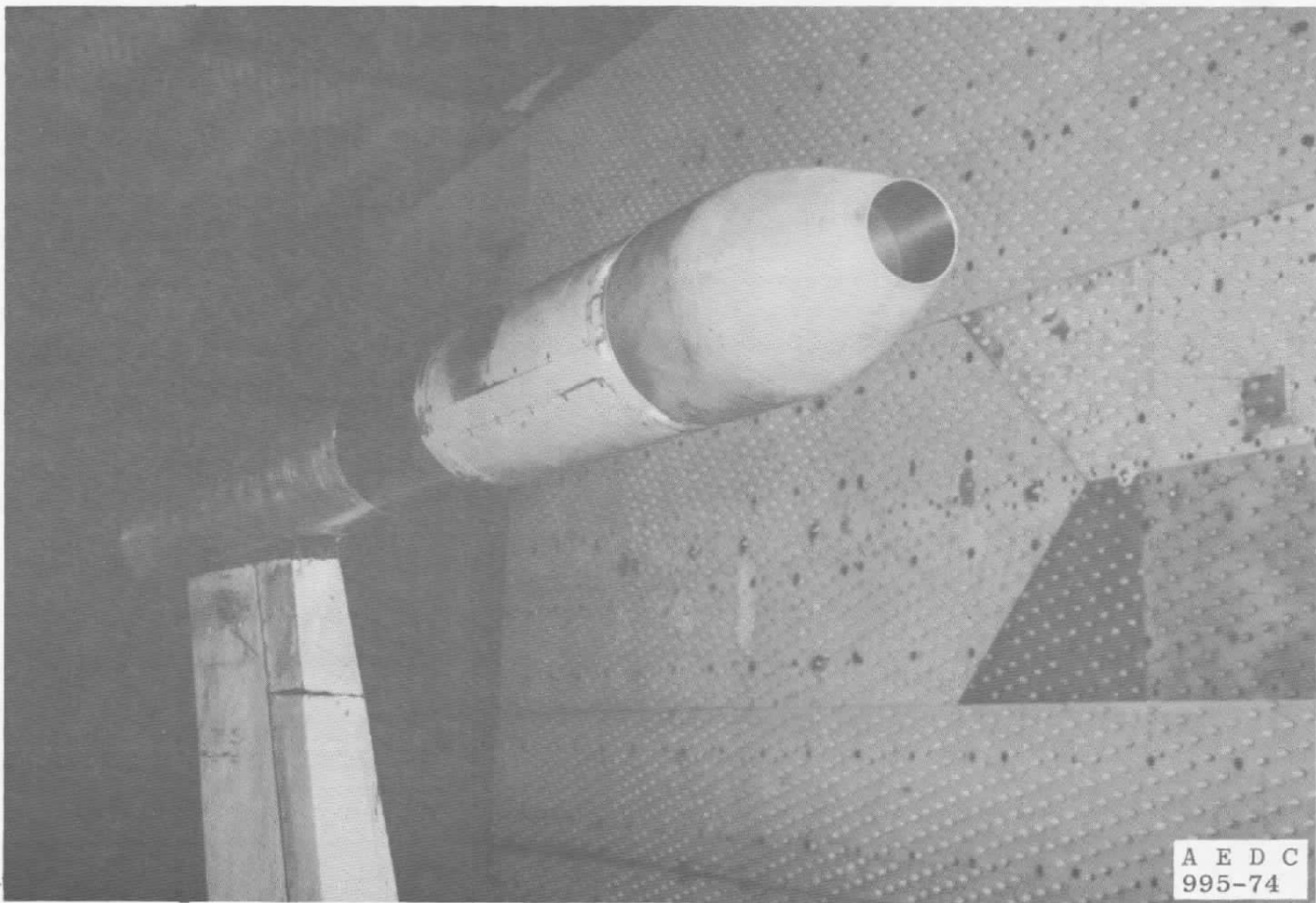
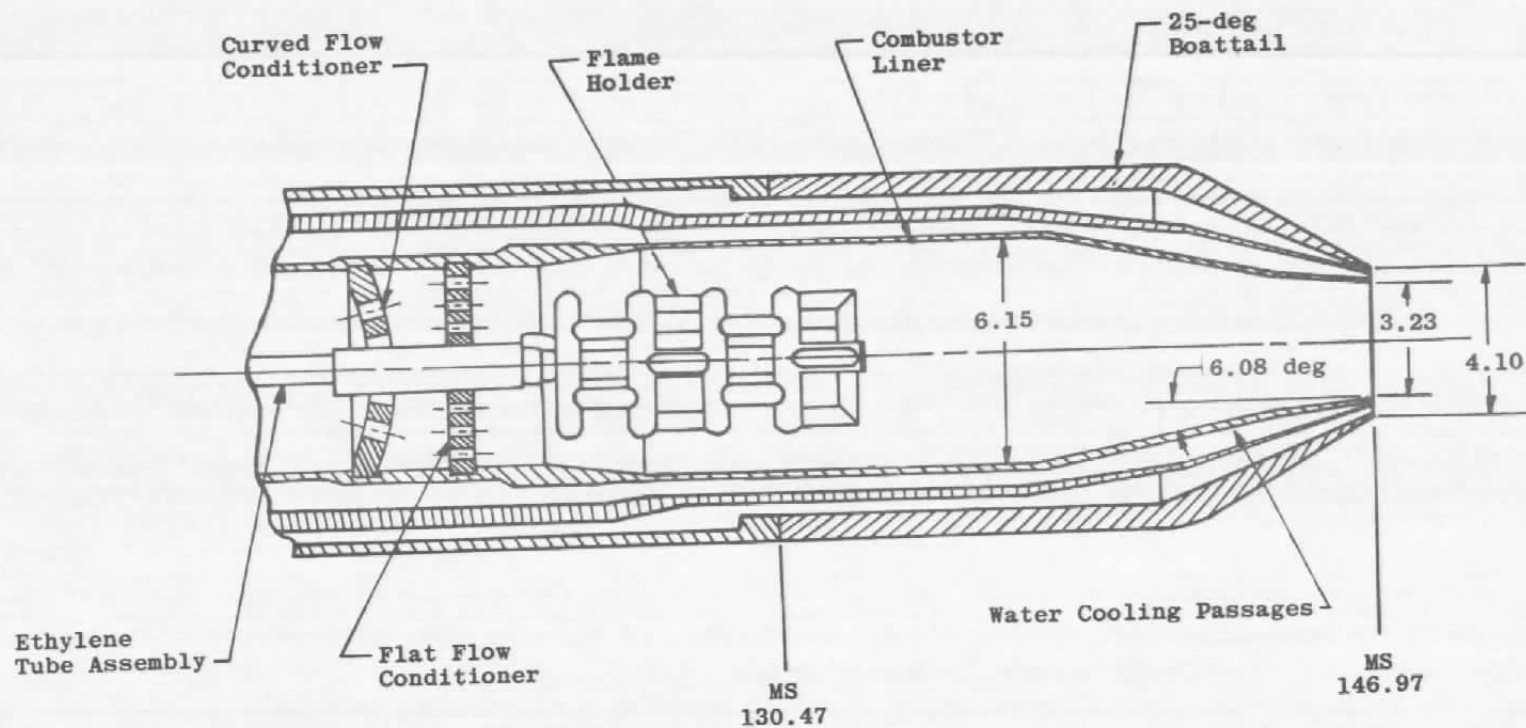


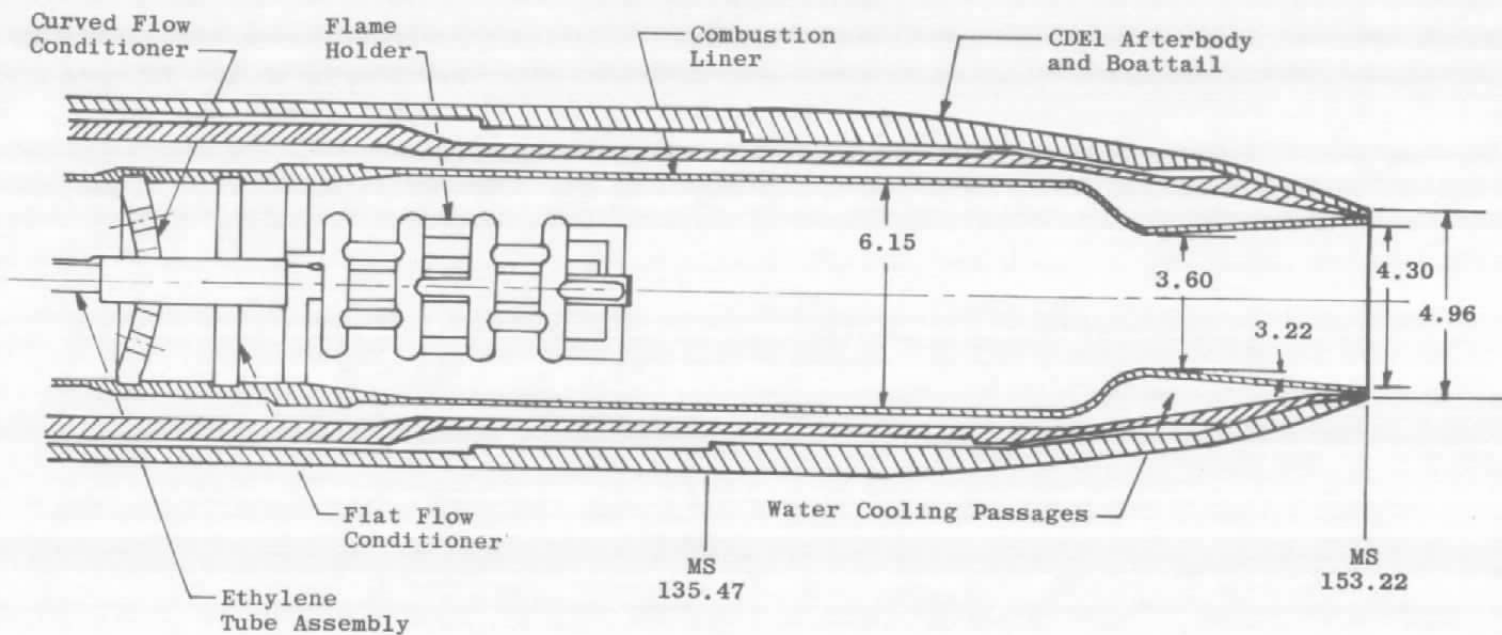
Figure 2. Model installation in Tunnel 16T.



Stations and Dimensions in Inches

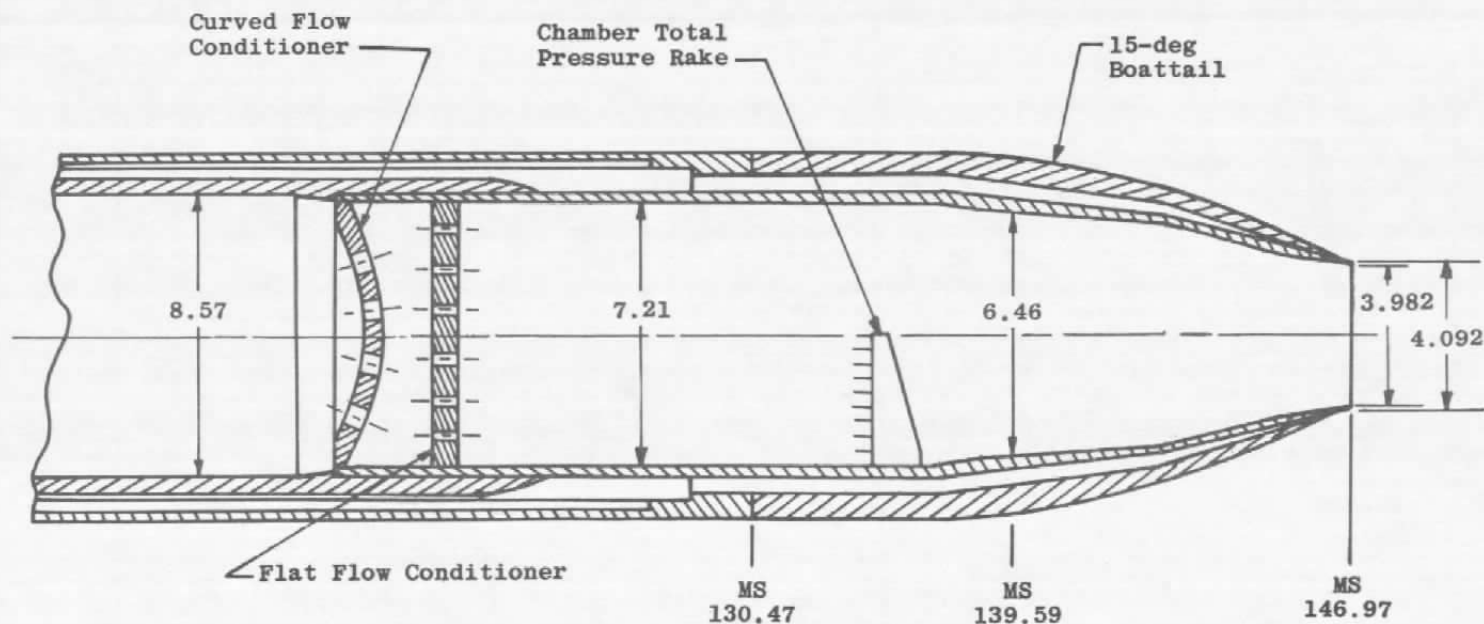
a. Configuration HF1

Figure 3. Sketch of the nozzle/afterbody configurations tested.



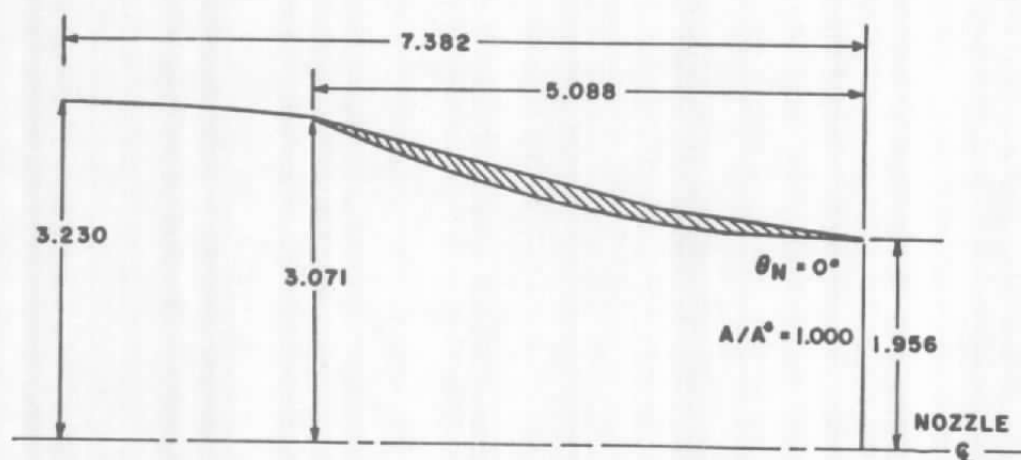
Stations and Dimensions in Inches

b. Configuration HF2
Figure 3. Continued.



Stations and Dimensions in Inches

c. Configuration CF1
Figure 3. Concluded.



STATIONS AND DIMENSIONS IN INCHES

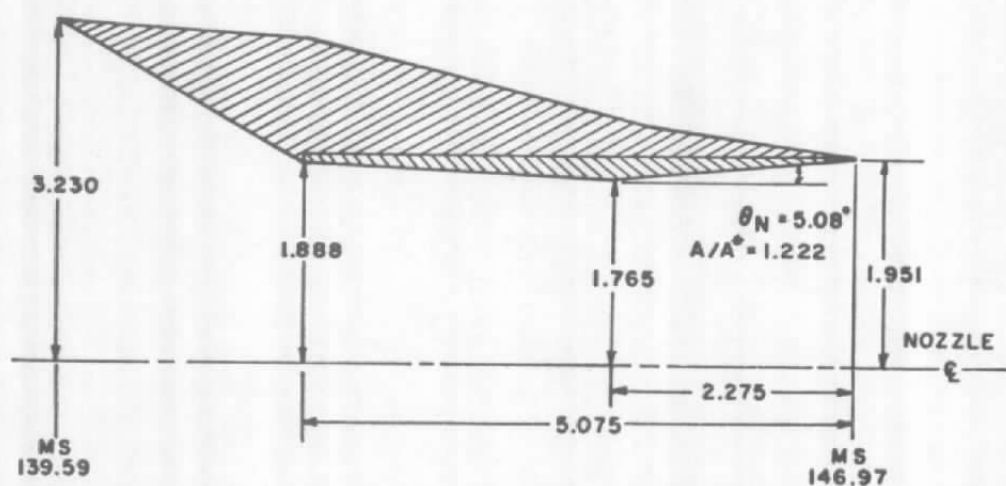
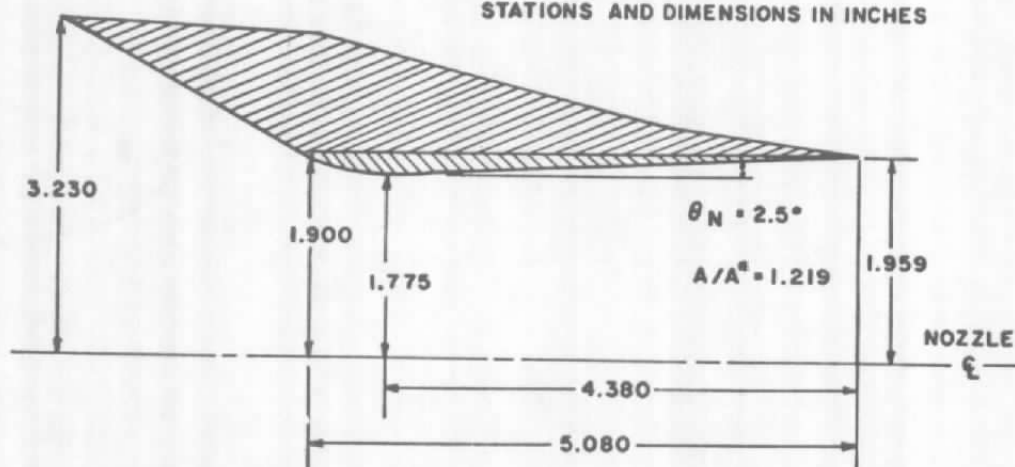
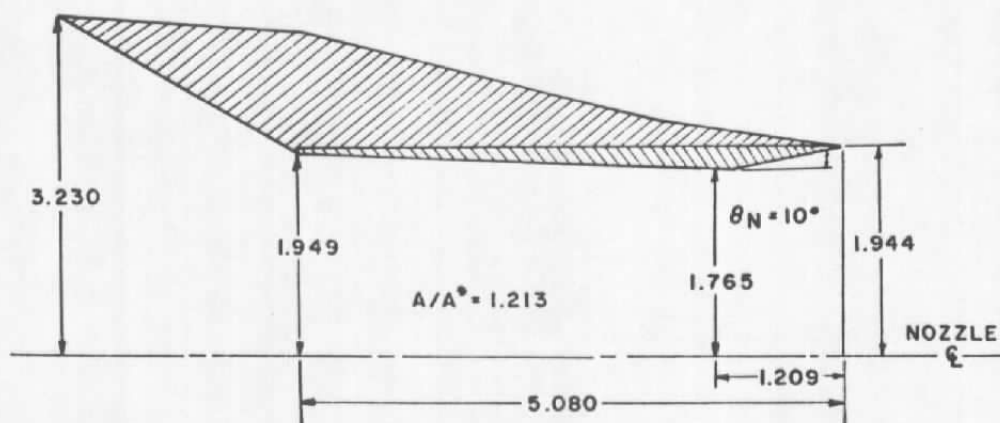


Figure 4. Sketch of internal nozzle inserts for the cold-flow configuration.



STATIONS AND DIMENSIONS IN INCHES

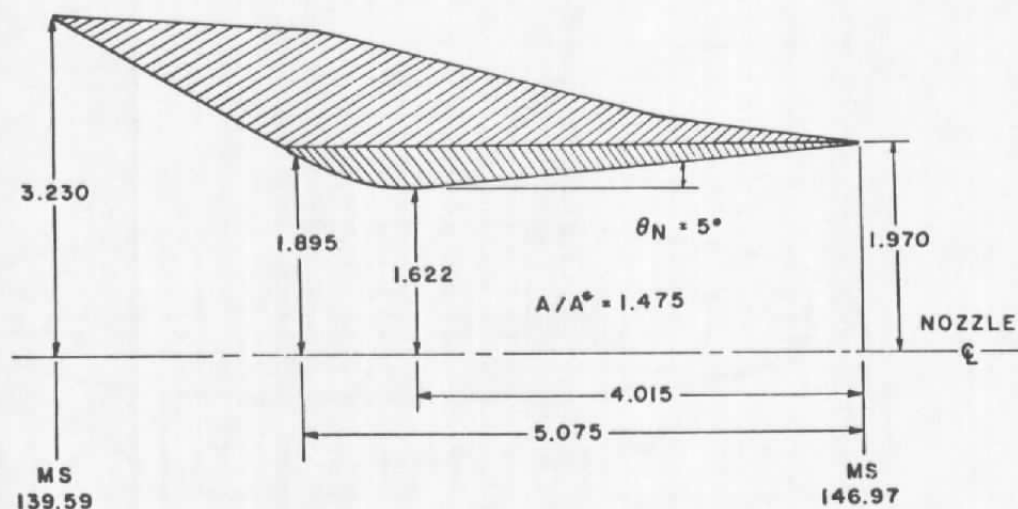
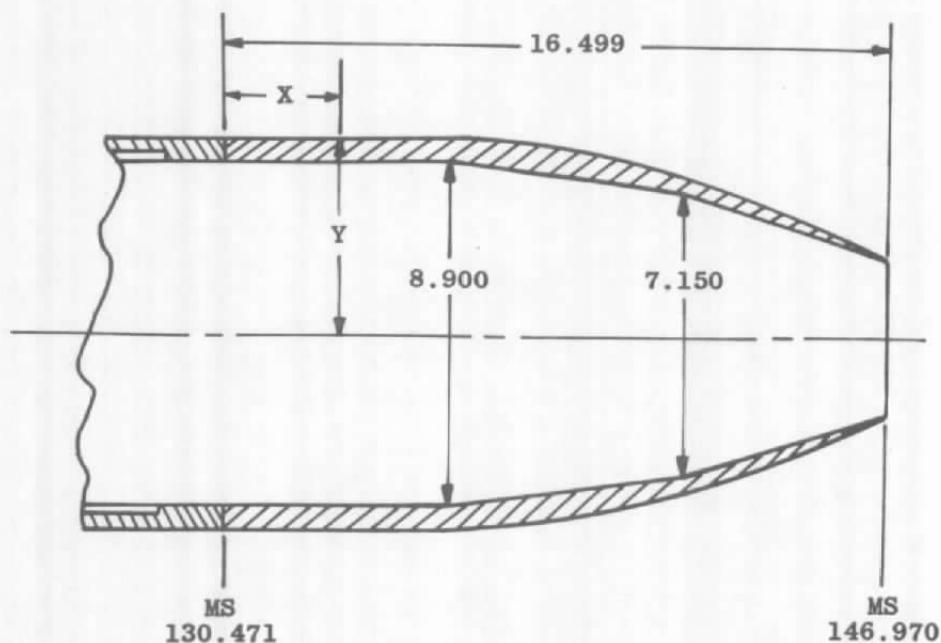


Figure 4. Concluded.

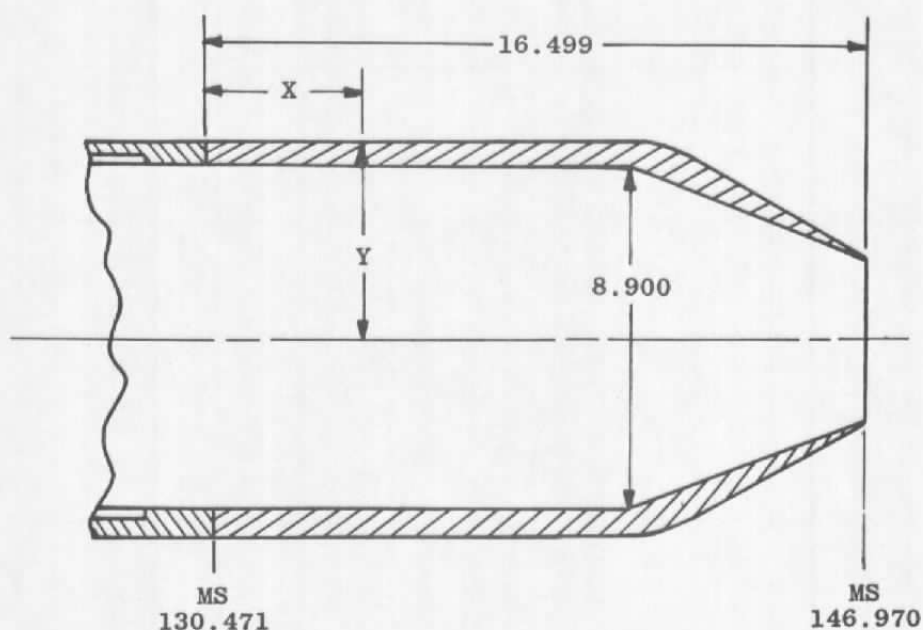


Stations and Dimensions in Inches

X	Y	X	Y
0	4.930	11.322	3.977
6.146	4.930	11.569	3.903
6.392	4.920	11.815	3.826
6.639	4.908	12.062	3.747
6.895	4.884	12.308	3.666
7.132	4.859	12.555	3.579
7.378	4.829	12.801	3.495
7.625	4.795	13.048	3.410
7.871	4.760	13.294	3.321
8.118	4.721	13.541	3.229
8.364	4.677	13.787	3.135
8.611	4.629	14.034	3.043
8.857	4.580	14.280	2.946
9.103	4.531	14.527	2.848
9.350	4.479	14.773	2.749
9.597	4.427	15.020	2.641
9.843	4.373	15.266	2.532
10.090	4.313	15.513	2.423
10.336	4.252	15.759	2.315
10.583	4.189	16.006	2.214
10.830	4.120	16.252	2.125
11.076	4.050	16.499	2.046

a. 15-deg boattail

Figure 5. Sketch of external afterbody contours for the hot-flow convergent nozzle configuration and the cold-flow configuration.



Stations and Dimensions in Inches

X	Y	X	Y
0	4.930	13.294	3.545
10.090	4.930	13.541	3.425
10.336	4.910	13.787	3.310
10.583	4.859	14.034	3.196
10.830	4.777	14.280	3.080
11.076	4.669	14.527	2.966
11.322	4.543	14.773	2.851
11.569	4.417	15.020	2.736
11.815	4.292	15.266	2.621
12.062	4.166	15.513	2.505
12.308	4.041	15.759	2.391
12.555	3.914	16.006	2.276
12.801	3.791	16.499	2.046

b. 25-deg boattail
Figure 5. Concluded.

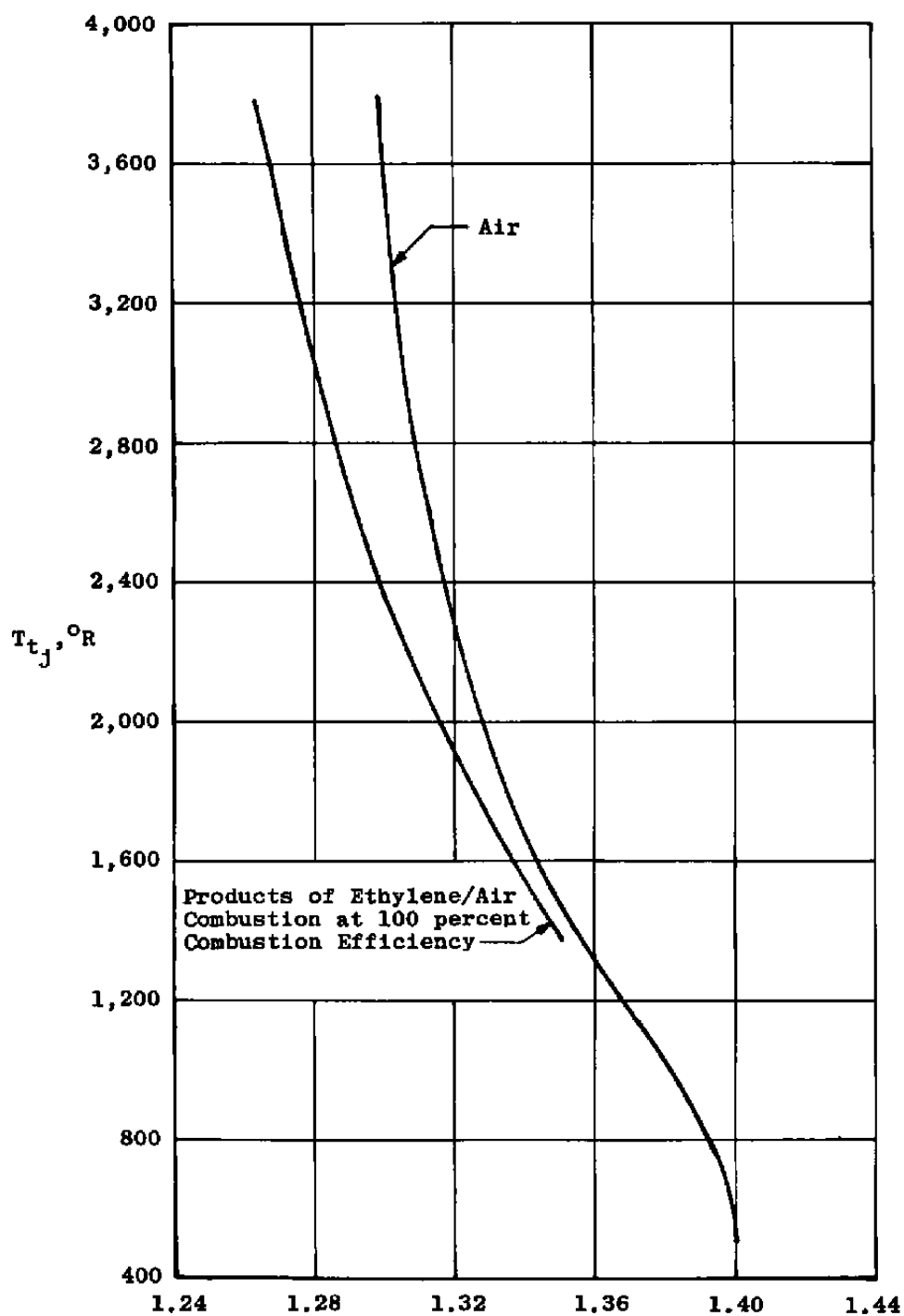
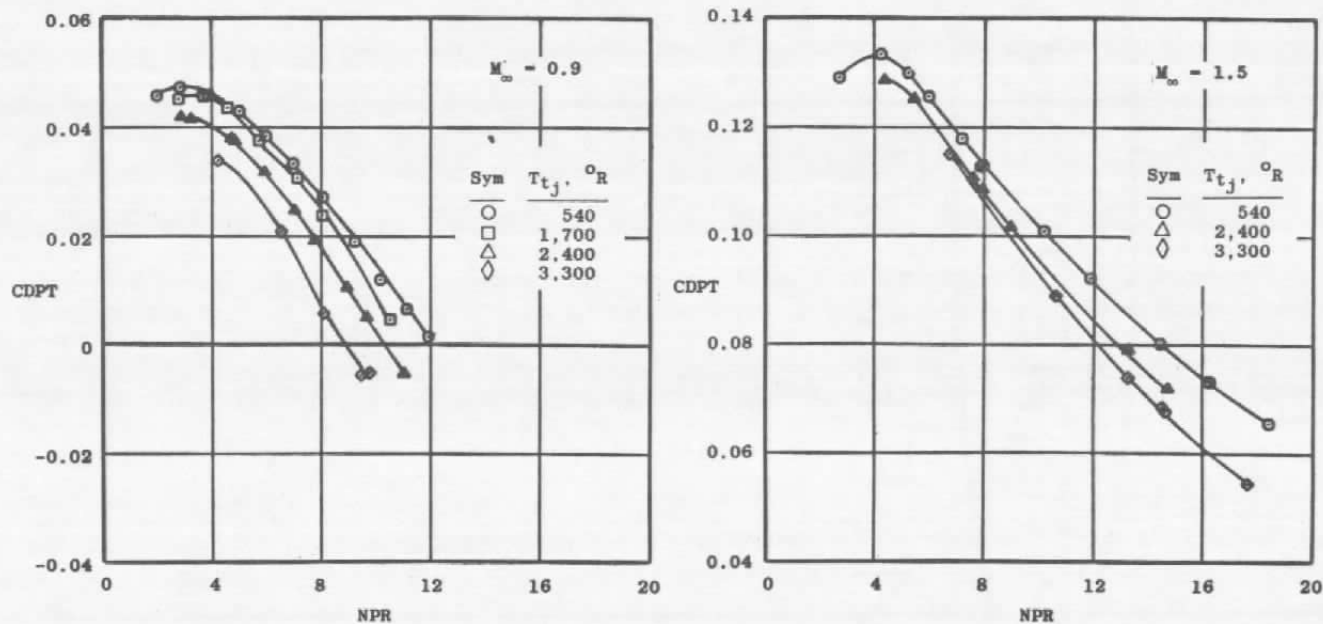


Figure 6. Variation of the ratio of specific heats as a function of jet total temperature for air and for the products of 100-percent ethylene/air combustion at $P_{tj} = 14.7$ psia.

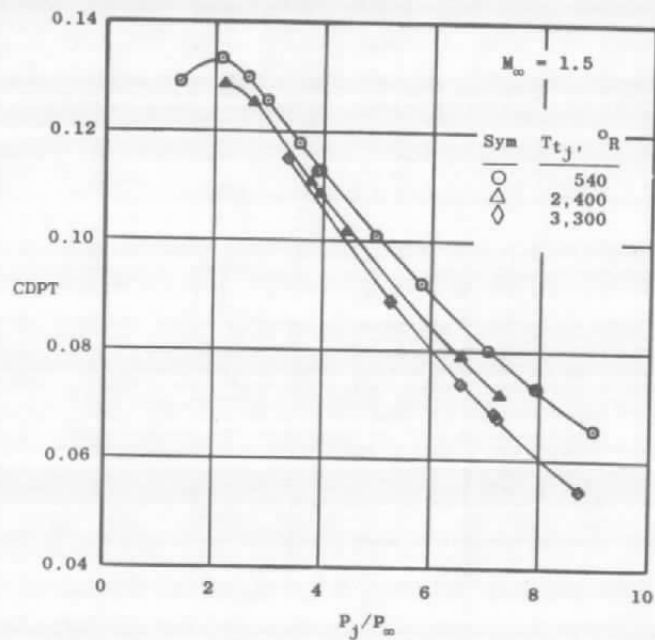
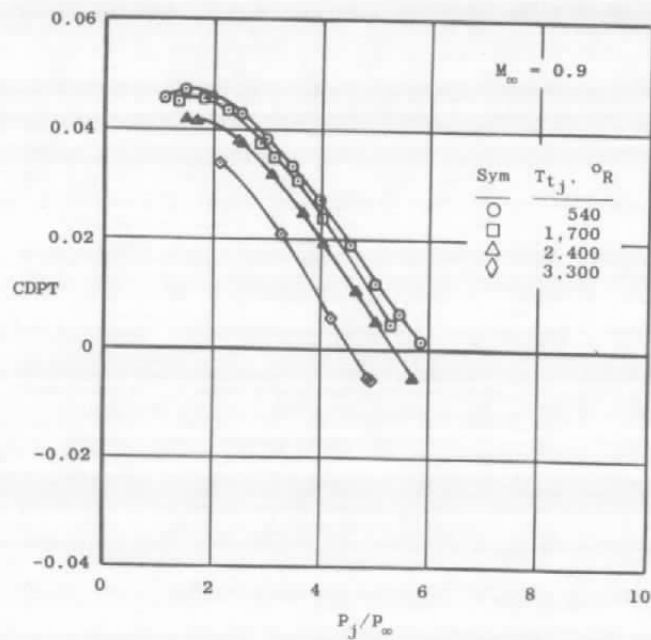
External Configuration: 15-deg Boattail
 Internal Configuration: HF1, $A/A^* = 1.0$, $\theta_N = 0$ deg
 Free-Stream Conditions: $M_\infty = 0.9$, $Re = 2.5 \times 10^6$
 $M_\infty = 1.5$, $Re = 2.5 \times 10^6$



a. Nozzle total pressure ratio

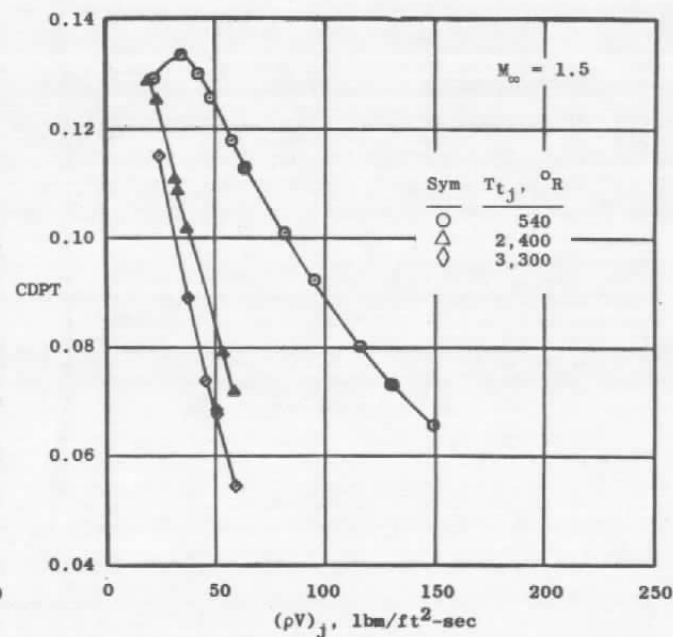
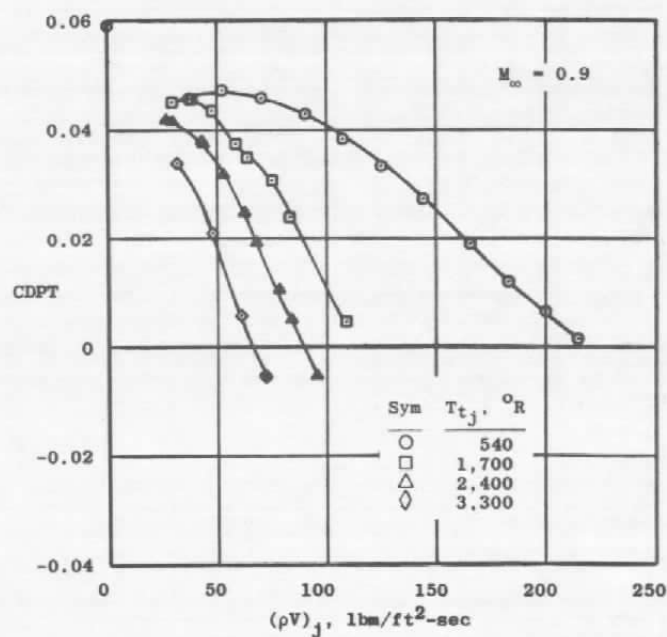
Figure 7. Jet temperature effects on afterbody pressure drag coefficient for a convergent nozzle geometry with unseparated afterbody flow.

External Configuration: 15-deg Boattail
 Internal Configuration: HF1, $A/A^* = 1.0$, $\theta_N = 0$ deg
 Free-Stream Conditions: $M_\infty = 0.9$, $Re = 2.5 \times 10^6$
 $M_\infty = 1.5$, $Re = 2.5 \times 10^6$



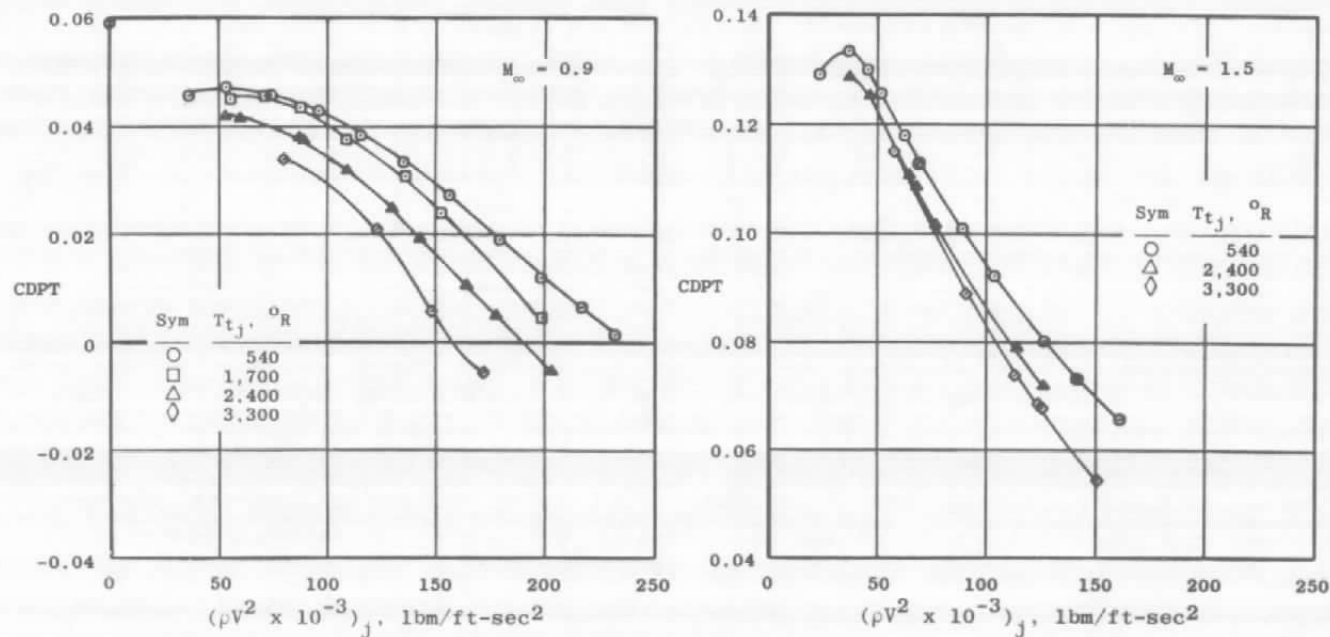
b. Nozzle exit static pressure ratio
 Figure 7. Continued.

External Configuration: 15-deg Boattail
 Internal Configuration: HF1, $A/A^* = 1.0$, $\theta_N = 0$ deg
 Free-Stream Conditions: $M_\infty = 0.9$, $Re = 2.5 \times 10^6$
 $M_\infty = 1.5$, $Re = 2.5 \times 10^6$



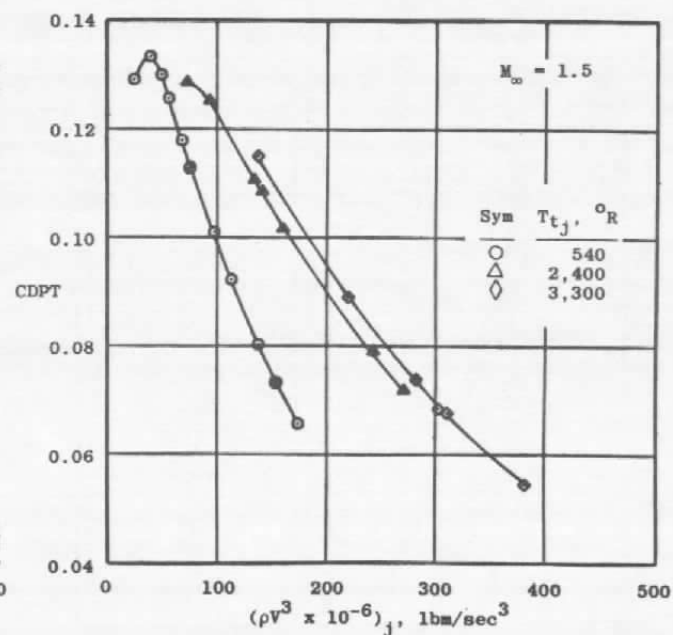
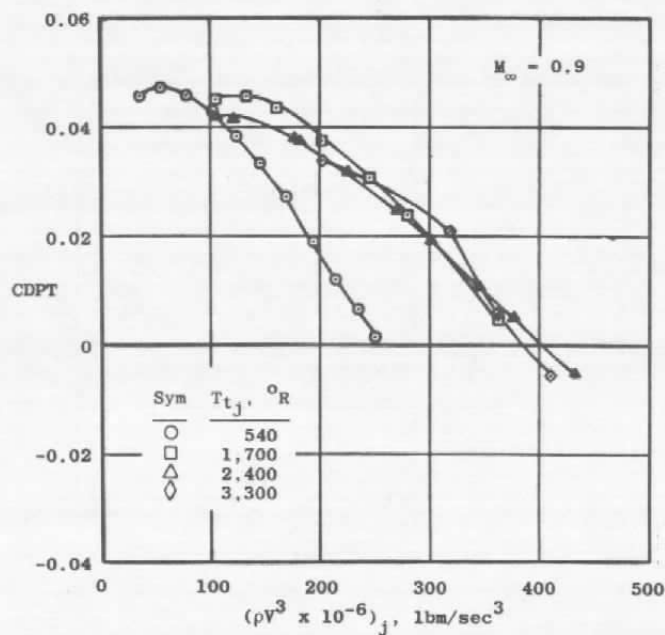
c. Nozzle exit mass flow flux
 Figure 7. Continued.

External Configuration: 15-deg Boattail
Internal Configuration: HF1, $A/A^* = 1.0$, $\theta_N = 0$ deg
Free-Stream Conditions: $M_\infty = 0.9$, $Re = 2.5 \times 10^6$
 $M_\infty = 1.5$, $Re = 2.5 \times 10^6$



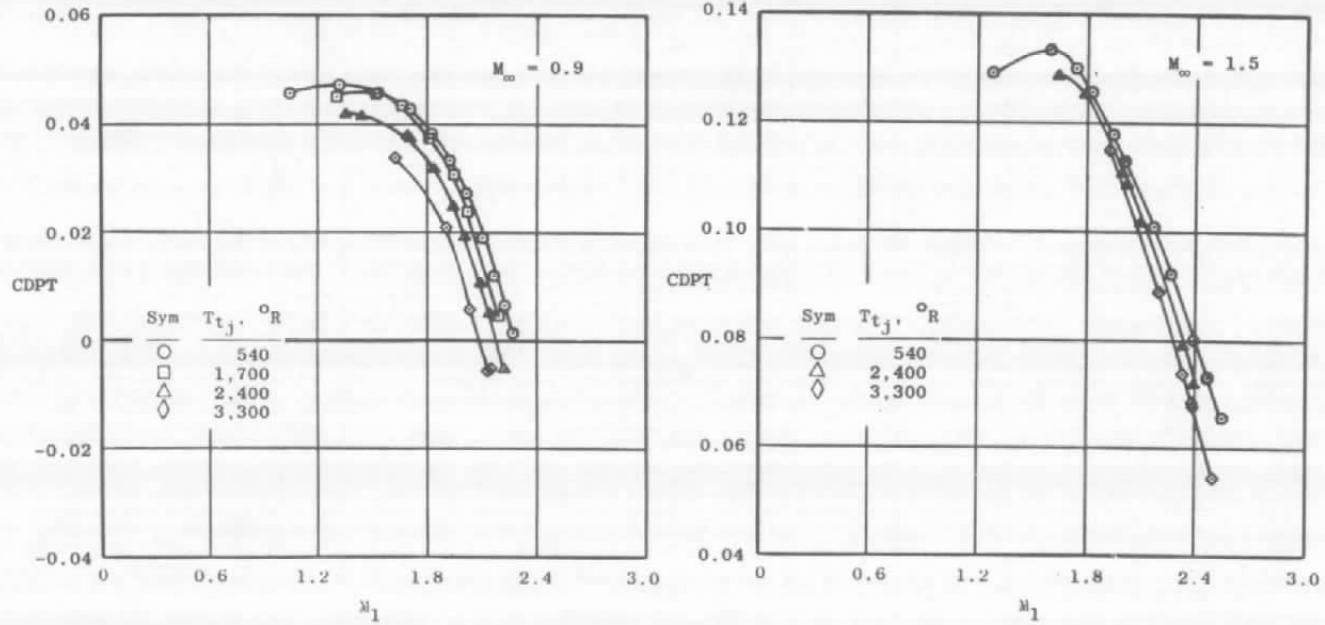
d. Nozzle exit momentum flux
Figure 7. Continued.

External Configuration: 15-deg Boattail
 Internal Configuration: HF1, $A/A^* = 1.0$, $\theta_N = 0$ deg
 Free-Stream Conditions: $M_\infty = 0.9$, $Re = 2.5 \times 10^6$
 $M_\infty = 1.5$, $Re = 2.5 \times 10^6$



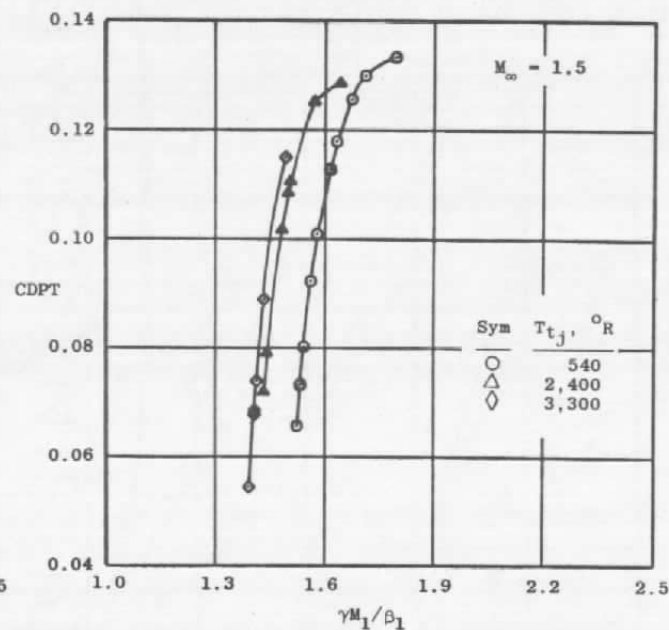
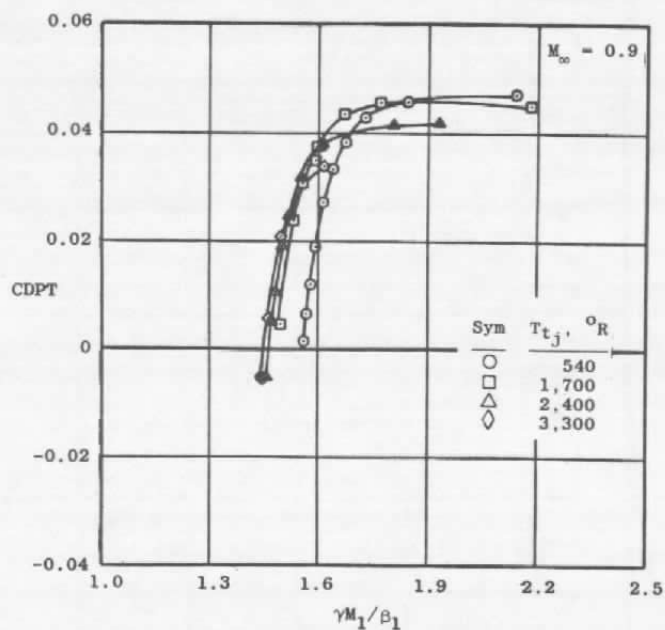
e. Nozzle exit kinetic energy flux
 Figure 7. Continued.

External Configuration: 15-deg Boattail
 Internal Configuration: HF1, $A/A^* = 1.0$, $\theta_N = 0$ deg
 Free-Stream Conditions: $M_\infty = 0.9$, $Re = 2.5 \times 10^6$
 $M_\infty = 1.5$, $Re = 2.5 \times 10^6$



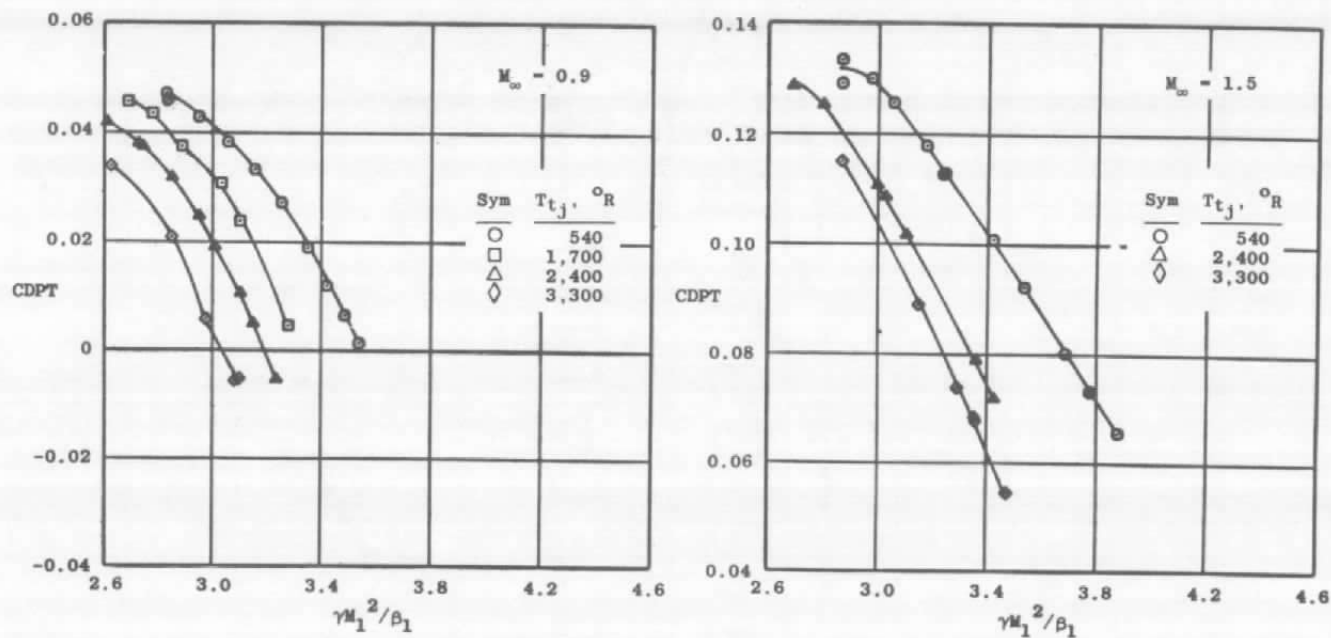
f. Jet boundary Mach number
 Figure 7. Continued.

External Configuration: 15-deg Boattail
 Internal Configuration: HF1, $A/A^* = 1.0$, $\theta_N = 0$ deg
 Free-Stream Conditions: $M_\infty = 0.9$, $Re = 2.5 \times 10^6$
 $M_\infty = 1.5$, $Re = 2.5 \times 10^6$



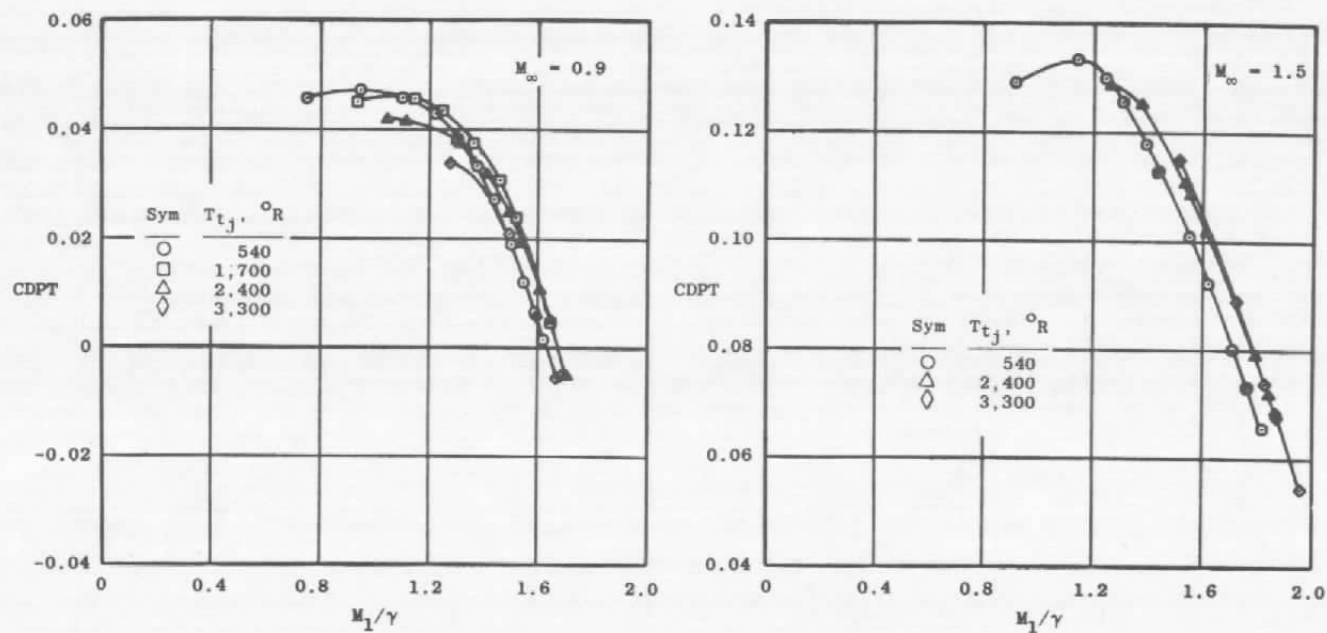
g. Jet boundary matching parameter
 Figure 7. Continued.

External Configuration: 15-deg Boattail
 Internal Configuration: HFI, $A/A^* = 1.0$, $\theta_N = 0$ deg
 Free-Stream Conditions: $M_\infty = 0.9$, $Re = 2.5 \times 10^6$
 $M_\infty = 1.5$, $Re = 2.5 \times 10^6$



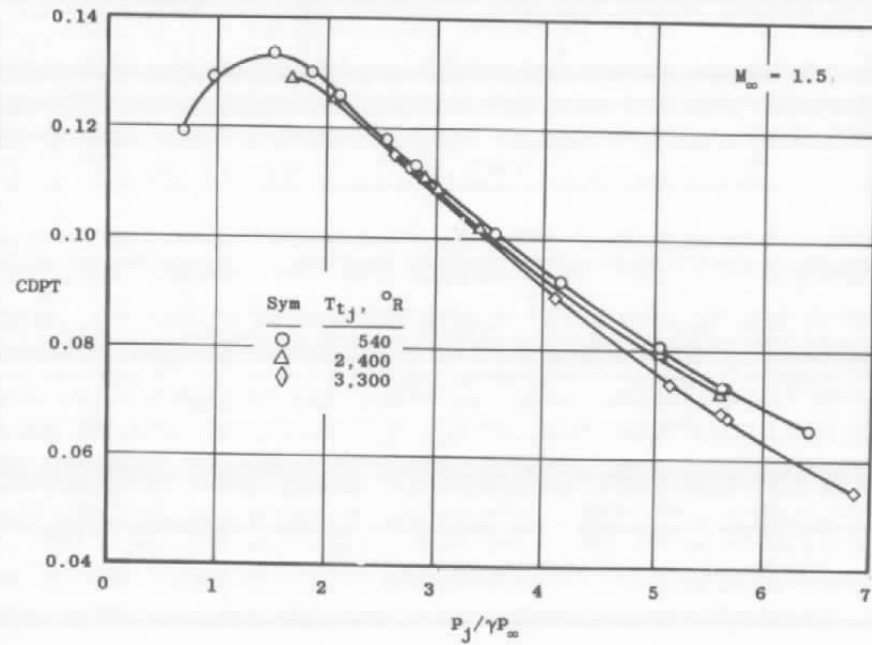
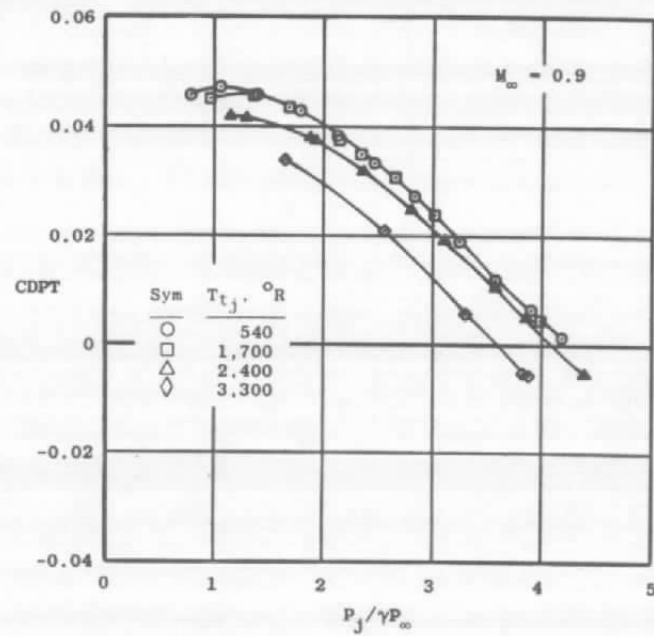
h. Jet boundary matching parameter
 Figure 7. Continued.

External Configuration: 15-deg Boattail
 Internal Configuration: HF1, $A/A^* = 1.0$, $\theta_N = 0$ deg
 Free-Stream Conditions: $M_\infty = 0.9$, $Re = 2.5 \times 10^6$
 $M_\infty = 1.5$, $Re = 2.5 \times 10^6$



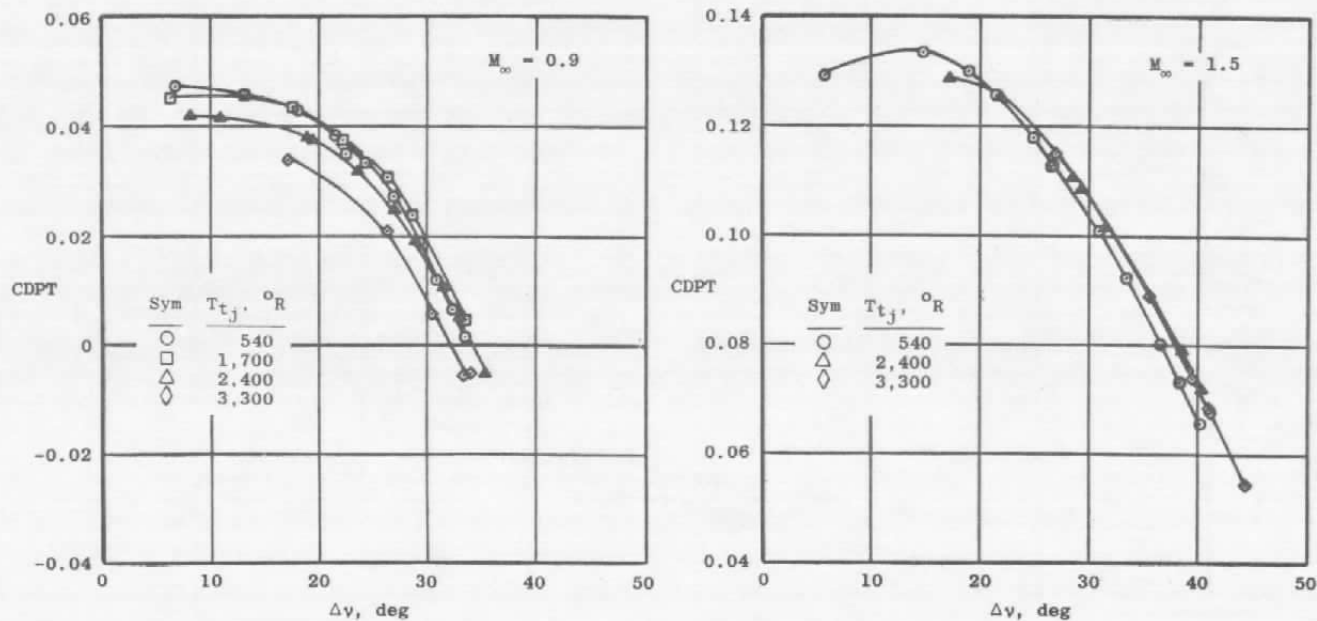
i. Jet boundary Mach number corrected for specific heat ratio
 Figure 7. Continued.

External Configuration: 15-deg Boattail
 Internal Configuration: HF1, $A/A^* = 1.0$, $\theta_N = 0$ deg
 Free-Stream Conditions: $M_\infty = 0.9$, $Re = 2.5 \times 10^6$
 $M_\infty = 1.5$, $Re = 2.5 \times 10^6$



j. Nozzle exit static pressure ratio corrected for specific heat ratio
 Figure 7. Continued.

External Configuration: 15-deg Boattail
 Internal Configuration: HF1, $A/A^* = 1.0$, $\theta_N = 0$ deg
 Free-Stream Conditions: $M_\infty = 0.9$, $Re = 2.5 \times 10^6$
 $M_\infty = 1.5$, $Re = 2.5 \times 10^6$



k. Incremental Prandtl-Meyer angle
 Figure 7. Concluded.

Sym	$T_{tj}, ^\circ R$	NPR
○	540	11.14
□	1,700	10.53
△	2,400	9.68
◇	3,300	8.08

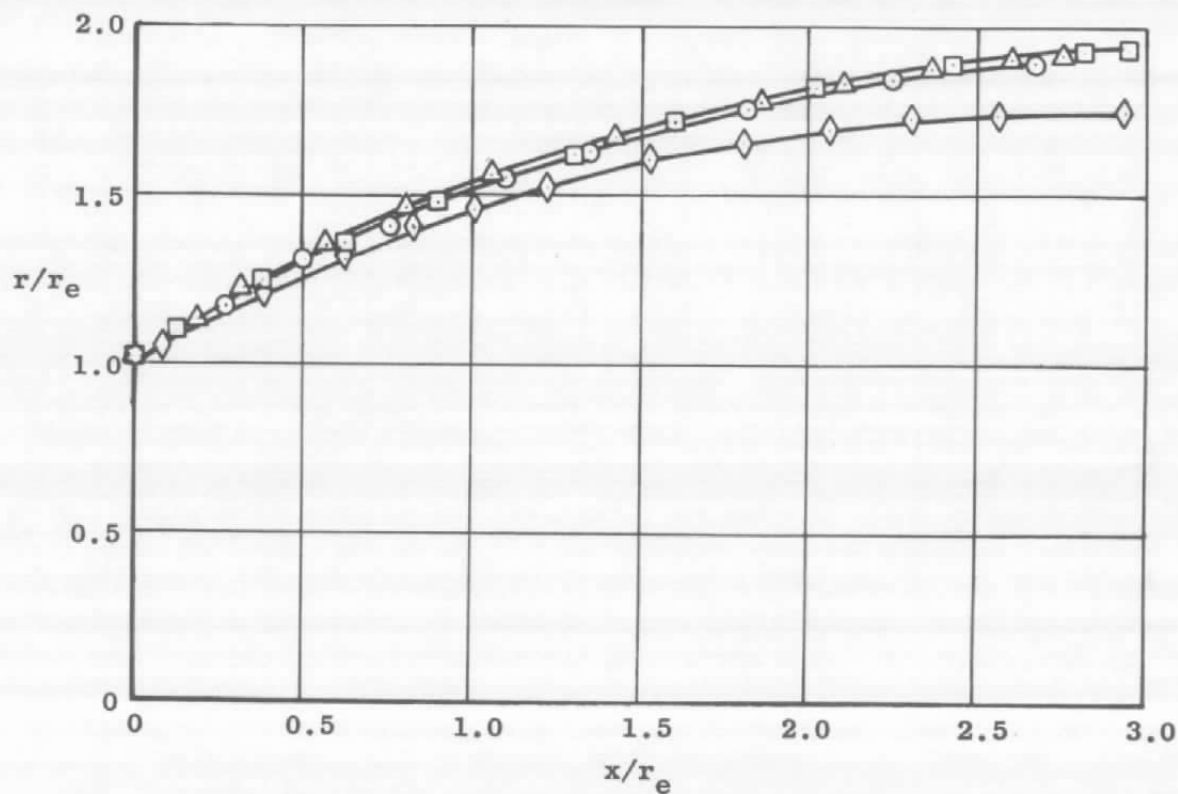


Figure 8. Comparison of quiescent MOC jet plume boundaries evaluated at equal drag conditions with jet total temperature as a variable.

Sym	$T_{tj}, ^\circ R$	NPR
○	540	9.25
□	1,700	9.00
△	2,400	8.70
◇	3,300	8.07

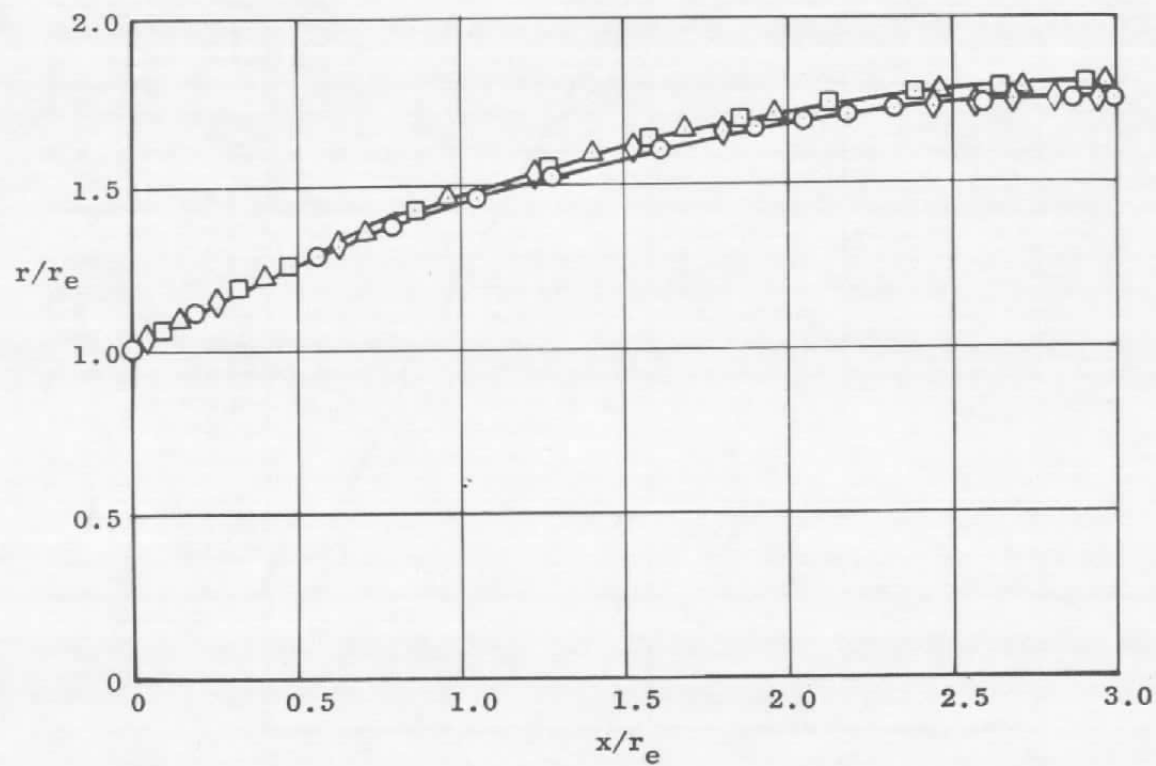


Figure 9. Comparison of quiescent MOC jet plume boundaries at a fixed value of $\Delta\nu$ with jet total temperature as a variable.

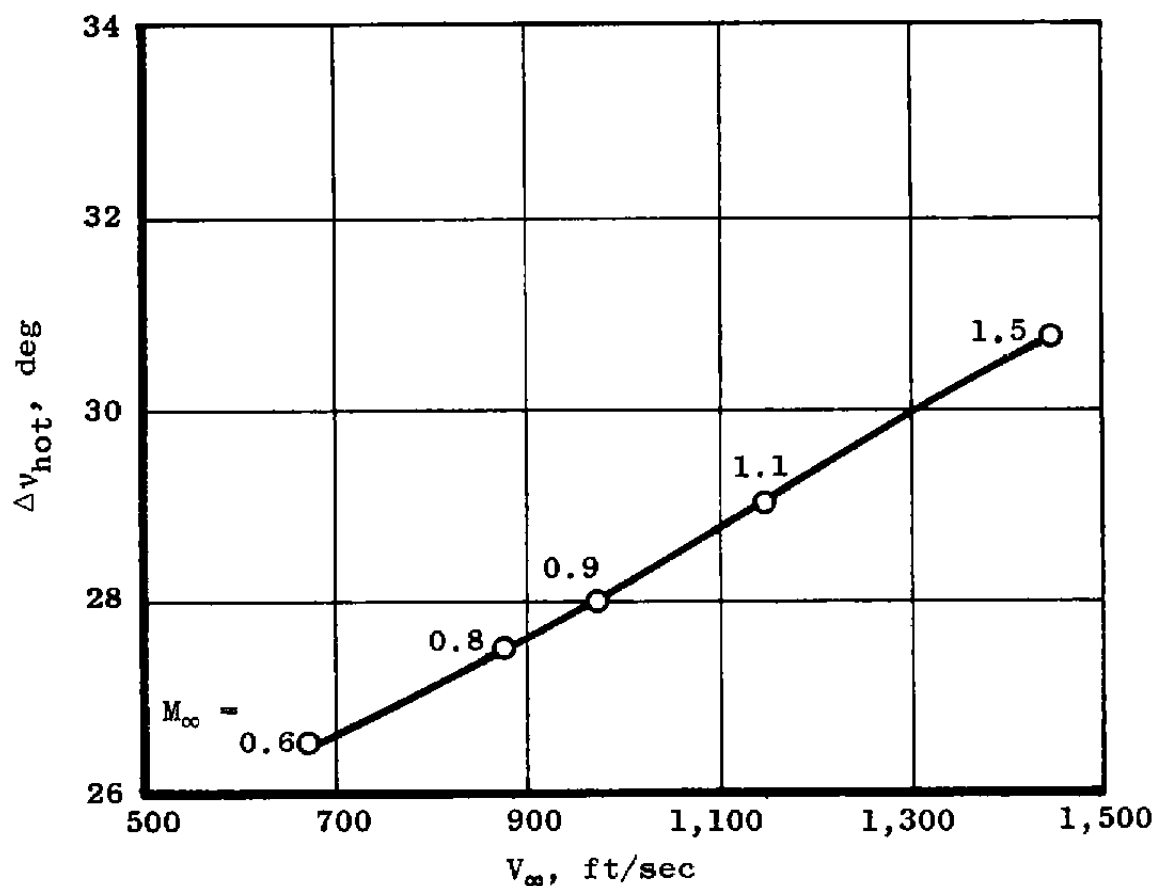
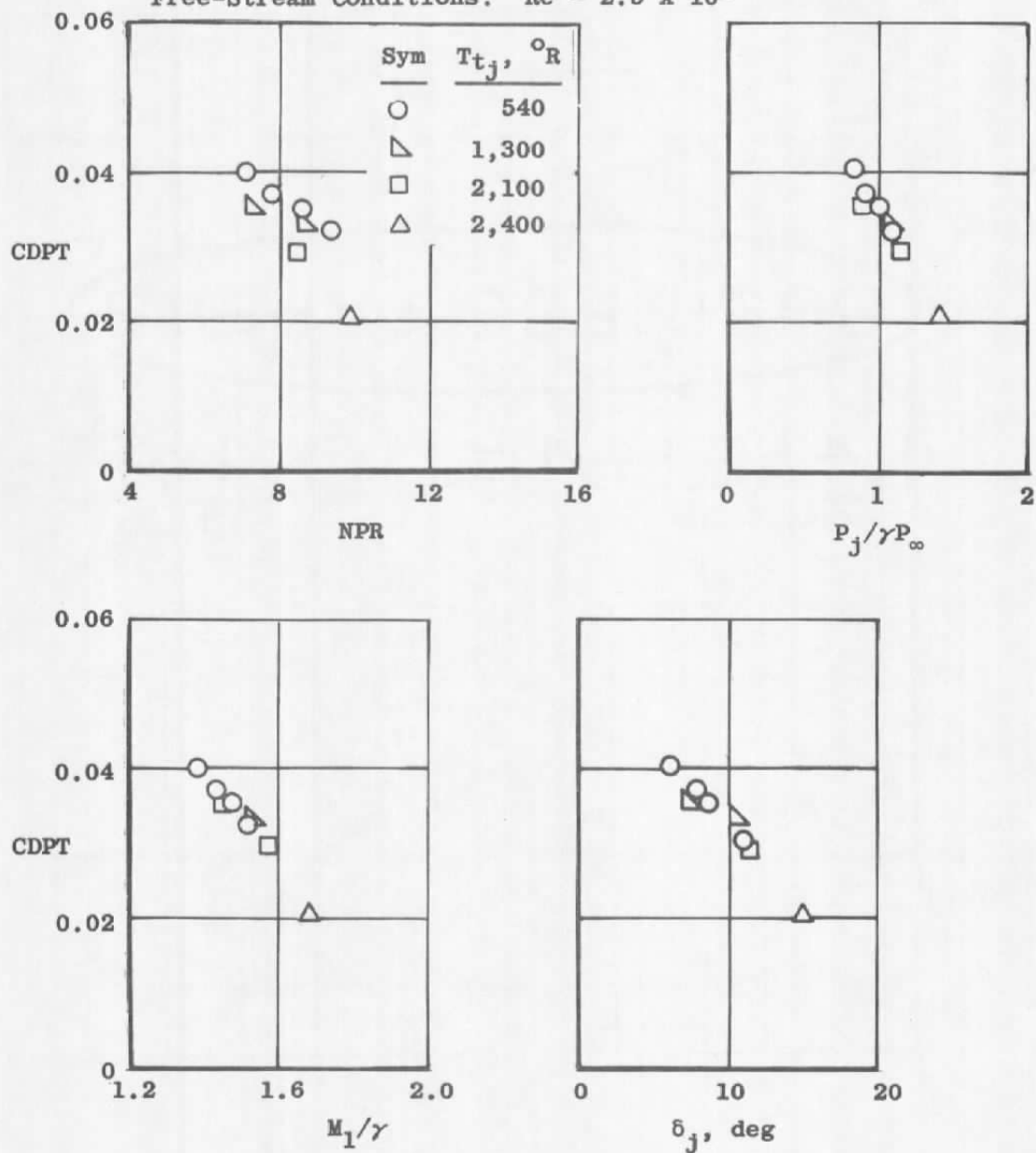


Figure 10. Δv_{hot} for equal drag as a function of free-stream velocity at a $\Delta v_{cold} = 30$ deg.

External Configuration: CDE1 Afterbody and Boattail

Internal Configuration: HF2, $A/A^* = 1.480$, $\theta_N = 3.22$ deg

Free-Stream Conditions: $Re = 2.5 \times 10^6$



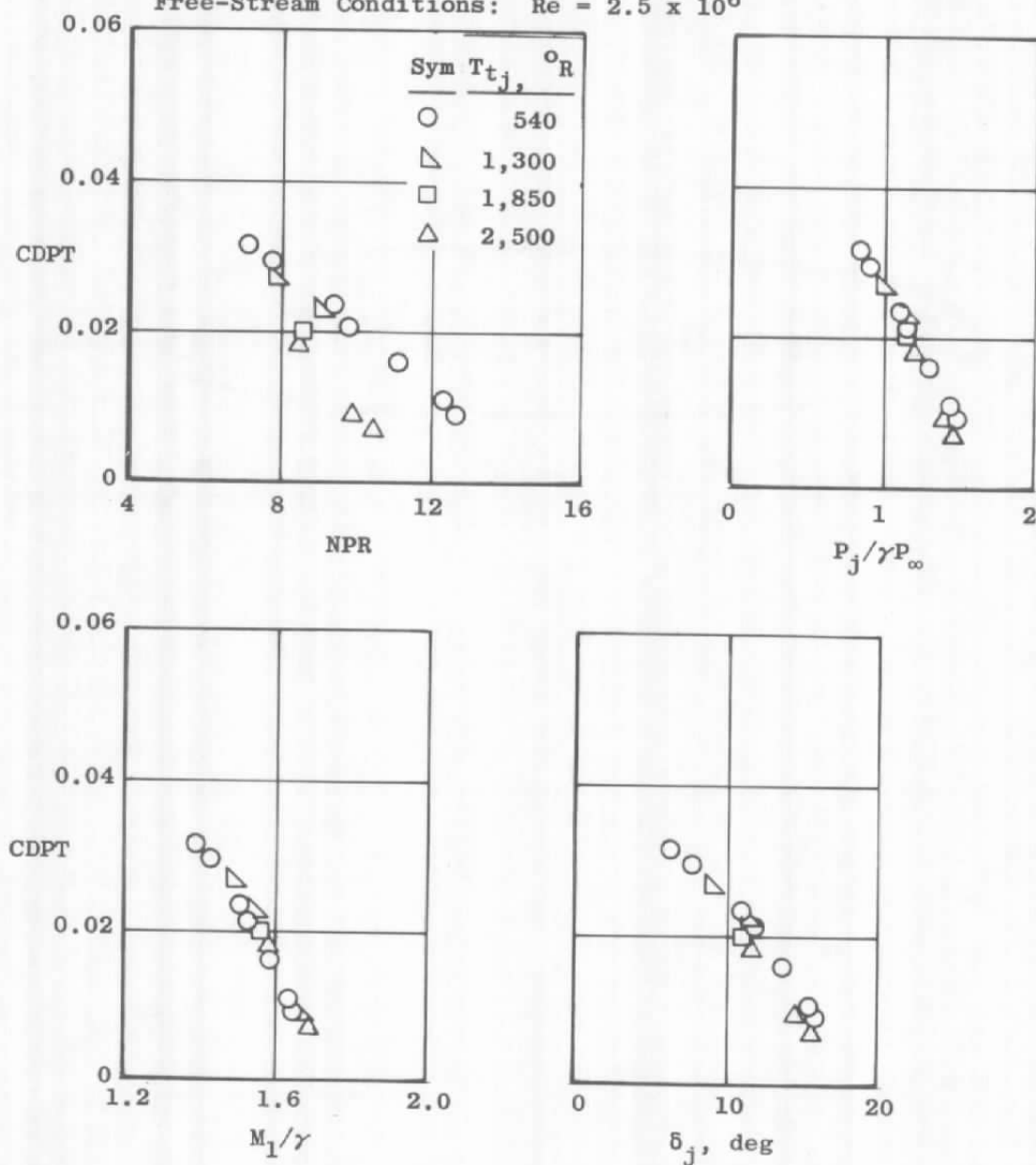
a. $M_\infty = 0.6$

Figure 11. Jet temperature effects on afterbody pressure drag coefficient for a convergent-divergent nozzle geometry with unseparated afterbody flow.

External Configuration: CDE1 Afterbody and Boattail

Internal Configuration: HF2, $A/A^* = 1.480$, $\theta_N = 3.22$ deg

Free-Stream Conditions: $Re = 2.5 \times 10^6$

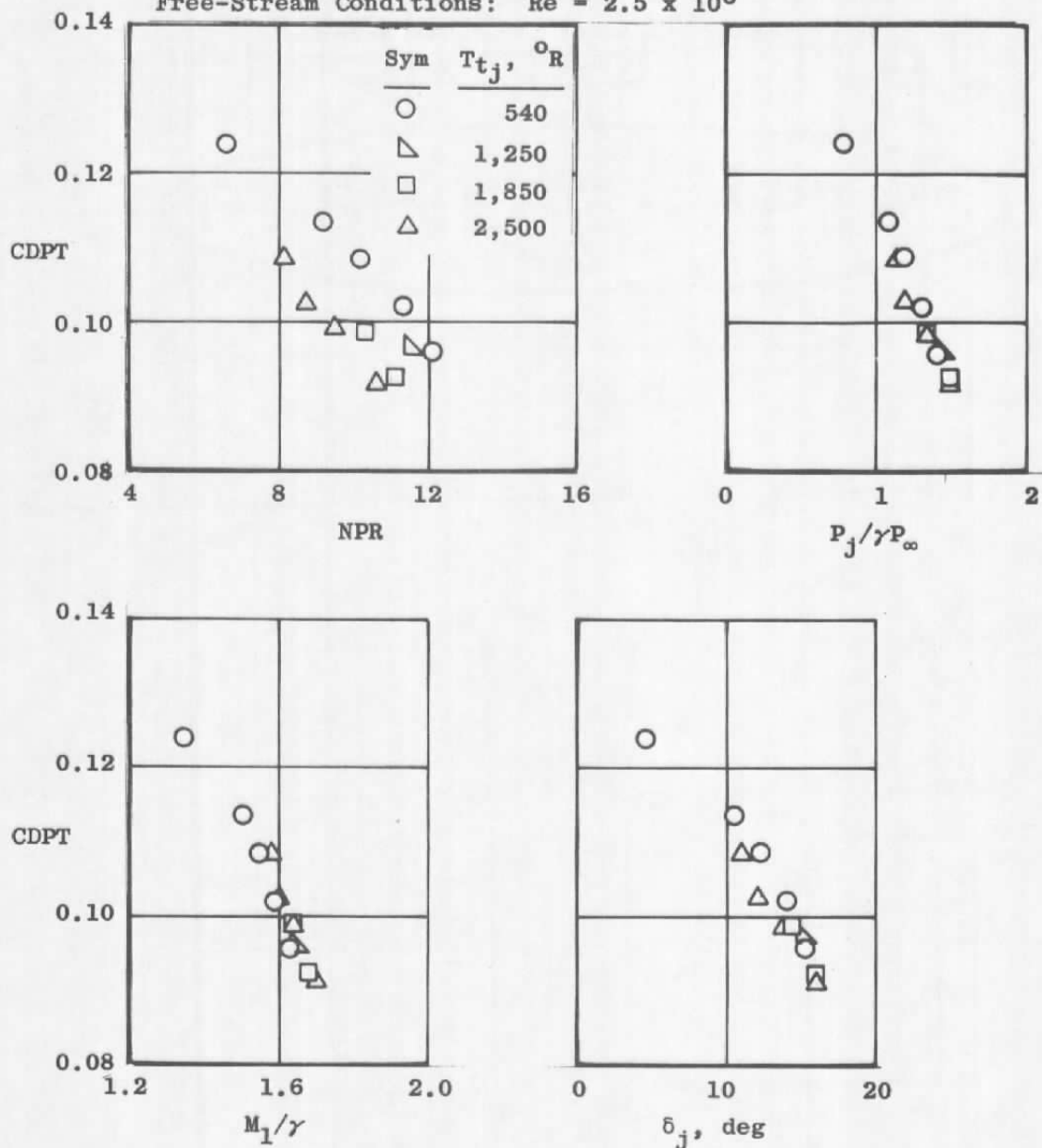


b. $M_\infty = 0.9$
Figure 11. Continued.

External Configuration: CDEI Afterbody and Boattail

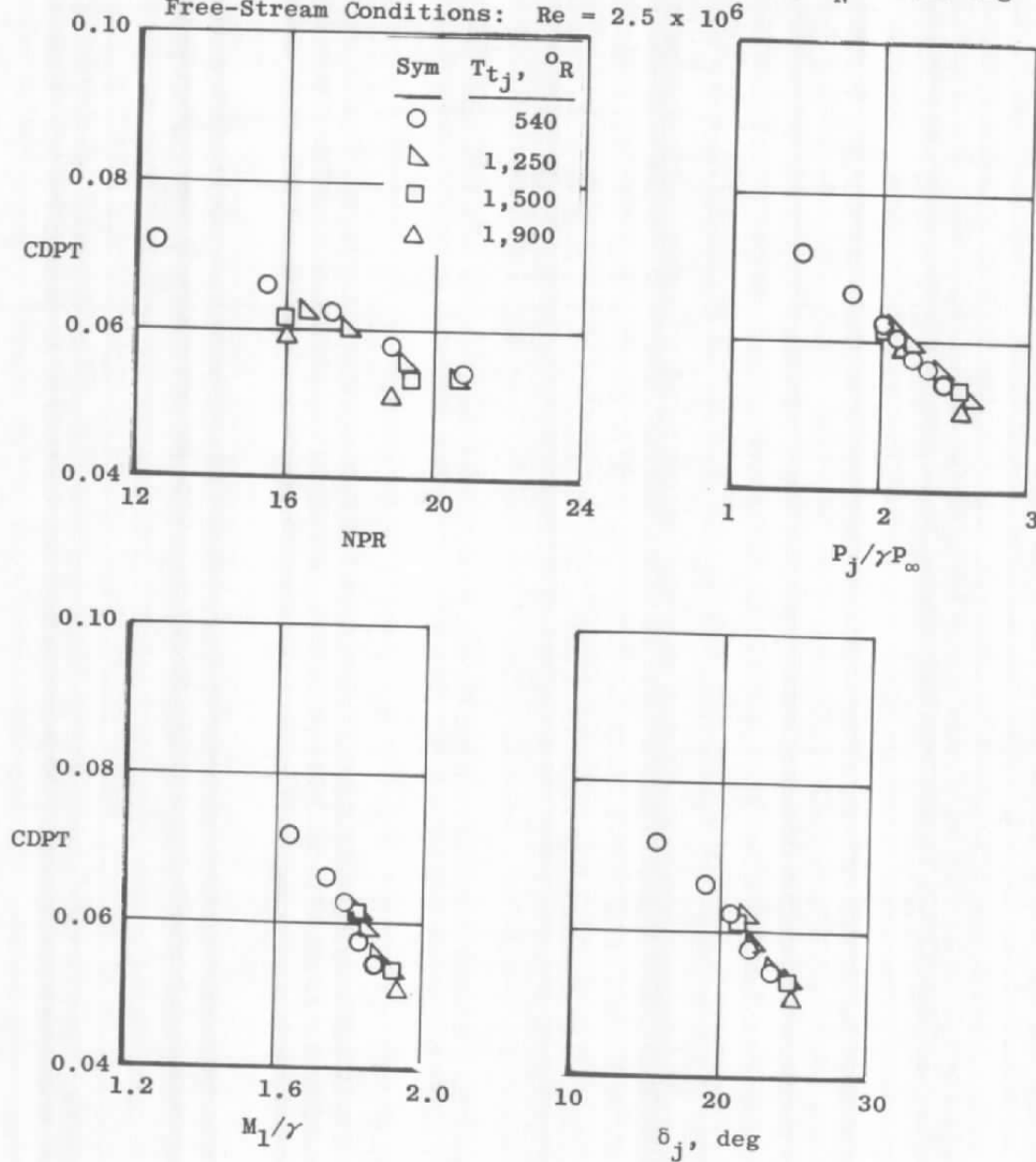
Internal Configuration: HF2, $A/A^* = 1.480$, $\theta_N = 3.22$ deg

Free-Stream Conditions: $Re = 2.5 \times 10^6$



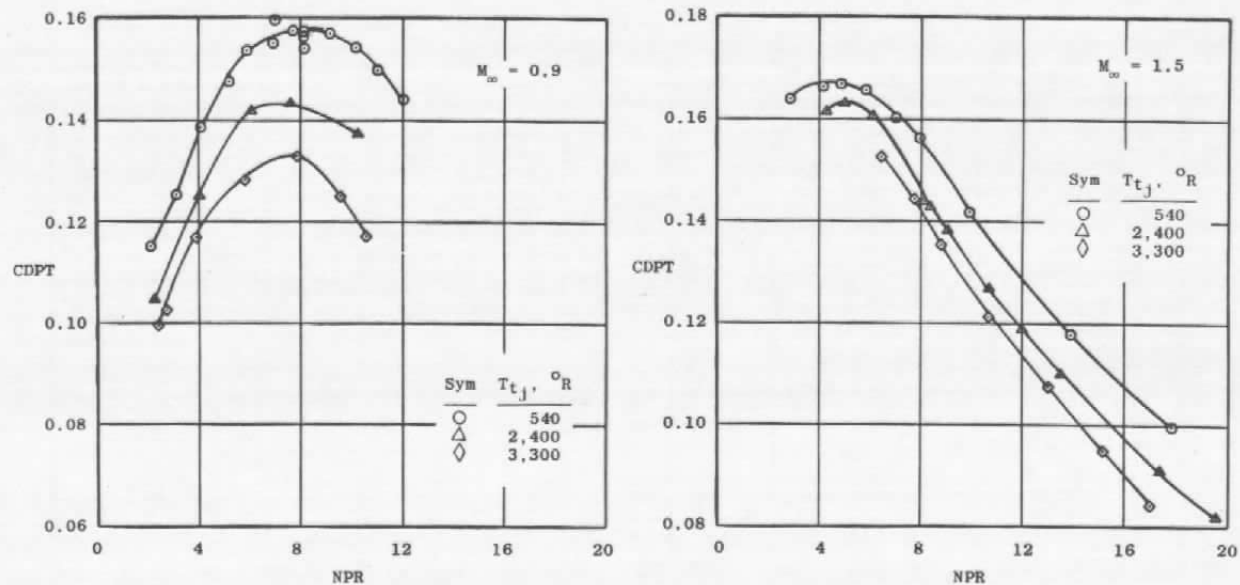
c. $M_\infty = 1.1$
Figure 11. Continued.

External Configuration: CDE1 Afterbody and Boattail
 Internal Configuration: HF2, $A/A^* = 1.480$, $\theta_N = 3.22$ deg
 Free-Stream Conditions: $Re = 2.5 \times 10^6$



d. $M_{\infty} = 1.5$
 Figure 11. Concluded.

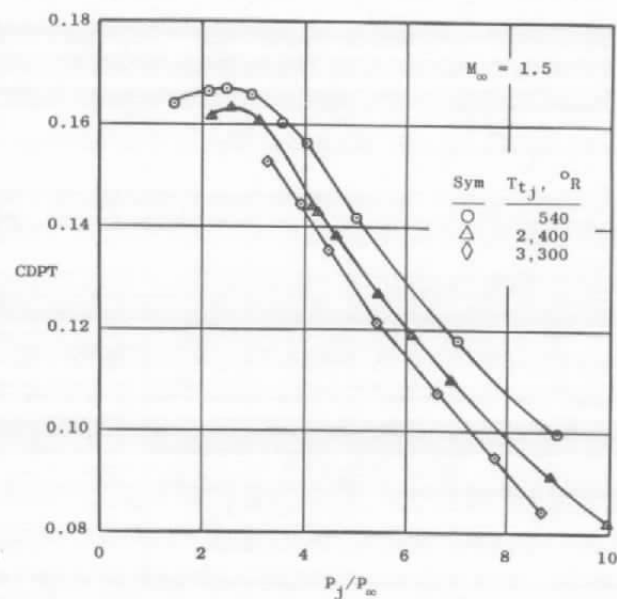
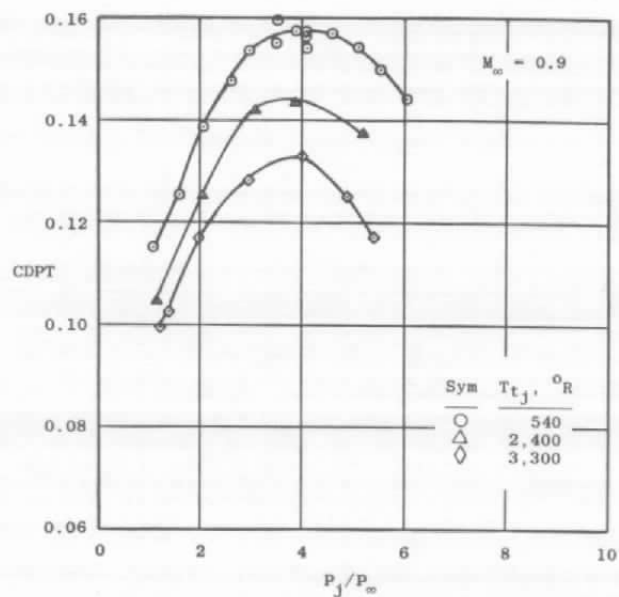
External Configuration: 25-deg Boattail
 Internal Configuration: HFI, $A/A^* = 1.0$, $\theta_N = 0$ deg
 Free-Stream Conditions: $M_\infty = 0.9$, $Re = 2.5 \times 10^6$
 $M_\infty = 1.5$, $Re = 2.5 \times 10^6$



a. Nozzle total pressure ratio

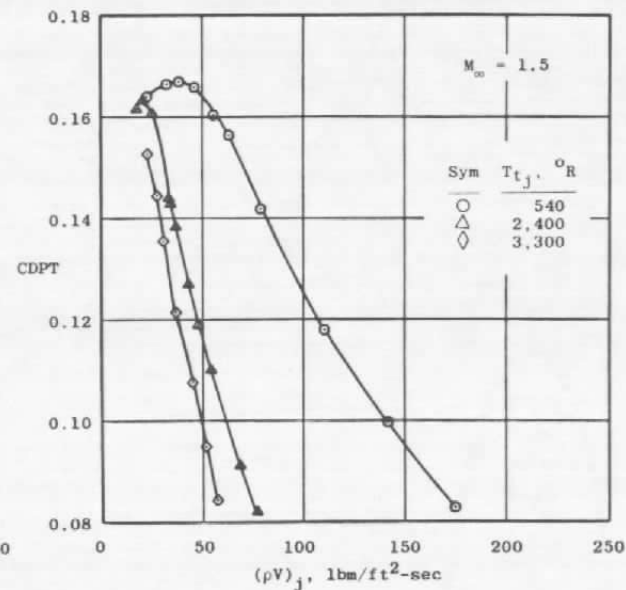
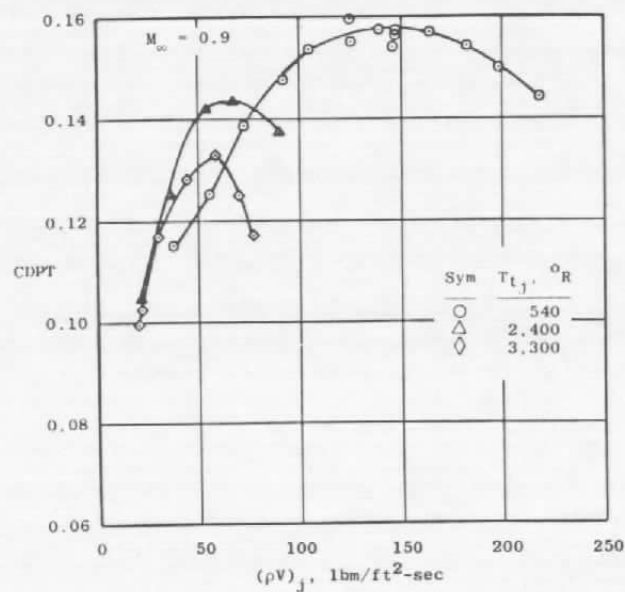
Figure 12. Jet temperature effects on afterbody pressure drag coefficient for a convergent nozzle geometry with separated afterbody flow.

External Configuration: 25-deg Boattail
 Internal Configuration: HF1, $A/A^* = 1.0$, $\theta_N = 0$ deg
 Free-Stream Conditions: $M_\infty = 0.9$, $Re = 2.5 \times 10^6$
 $M_\infty = 1.5$, $Re = 2.5 \times 10^6$



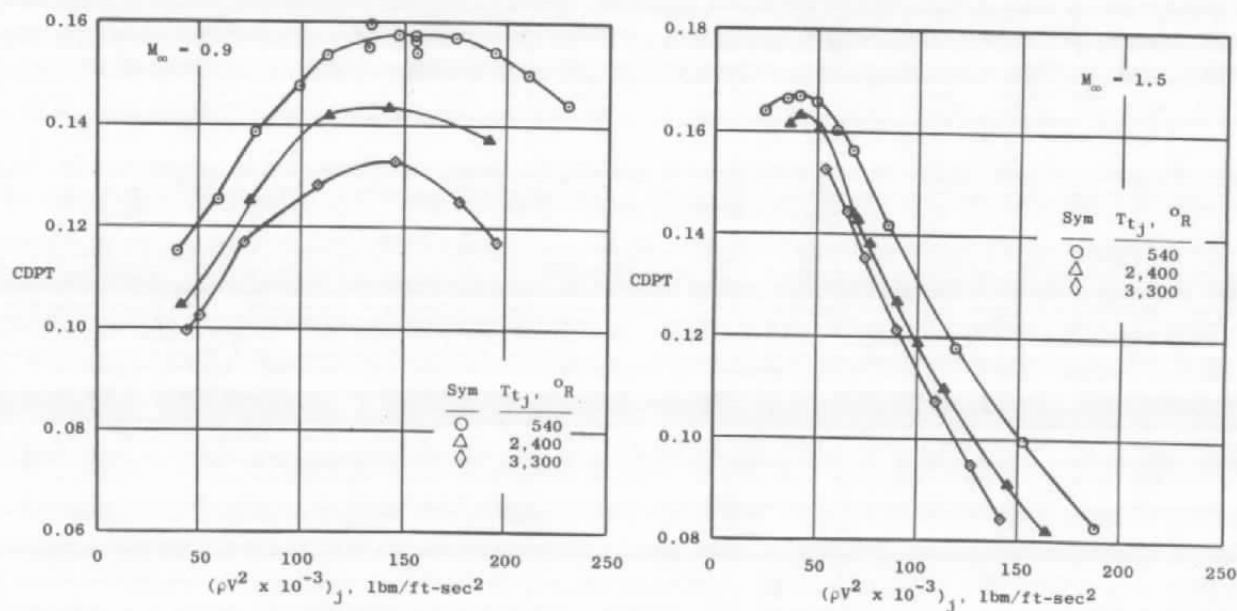
b. Nozzle exit static pressure ratio
 Figure 12. Continued.

External Configuration: 25-deg Boattail
 Internal Configuration: HF1, $A/A^* = 1.0$, $\theta_N = 0$ deg
 Free-Stream Conditions: $M_\infty = 0.9$, $Re = 2.5 \times 10^6$
 $M_\infty = 1.5$, $Re = 2.5 \times 10^6$



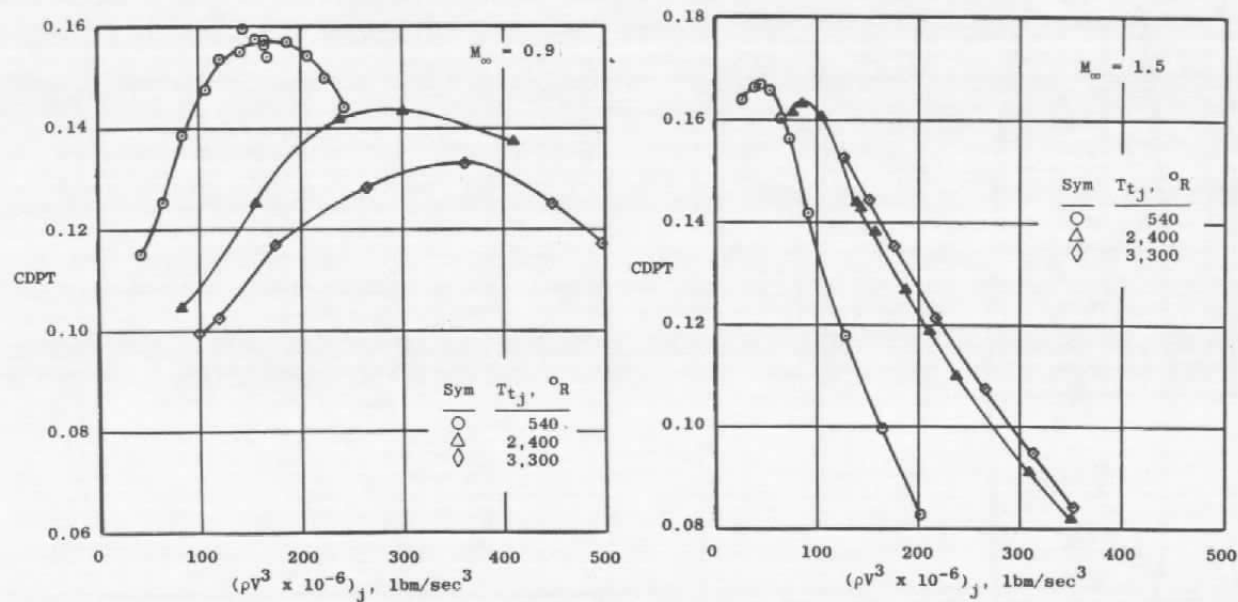
c. Nozzle exit mass flow flux
 Figure 12. Continued.

External Configuration: 25-deg Boattail
 Internal Configuration: HFl, $A/A^* = 1.0$, $\theta_N = 0$ deg
 Free-Stream Conditions: $M_\infty = 0.9$, $Re = 2.5 \times 10^6$
 $M_\infty = 1.5$, $Re = 2.5 \times 10^6$



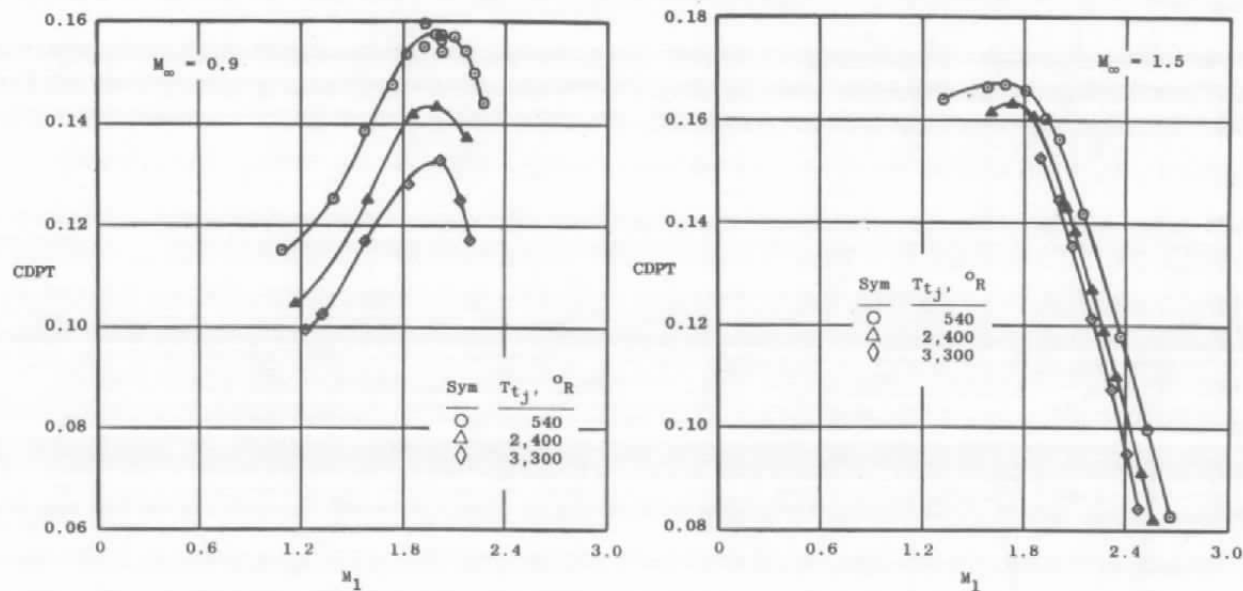
d. Nozzle exit momentum flux
 Figure 12. Continued.

External Configuration: 25-deg Boattail
 Internal Configuration: HFl, $A/A^* = 1.0$, $\theta_N = 0$ deg
 Free-Stream Conditions: $M_\infty = 0.9$, $Re = 2.5 \times 10^6$
 $M_\infty = 1.5$, $Re = 2.5 \times 10^6$



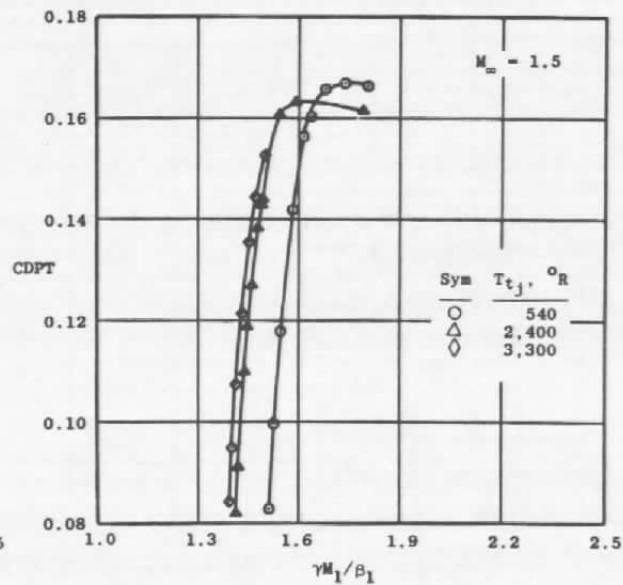
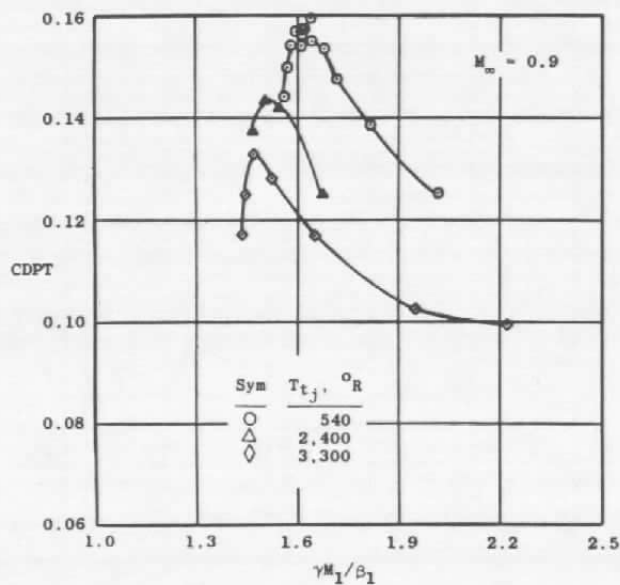
e. Nozzle exit kinetic energy flux
 Figure 12. Continued.

External Configuration: 25-deg Boattail
 Internal Configuration: HF1, $A/A^* = 1.0$, $\theta_N = 0$ deg
 Free-Stream Conditions: $M_\infty = 0.9$, $Re = 2.5 \times 10^6$
 $M_\infty = 1.5$, $Re = 2.5 \times 10^6$



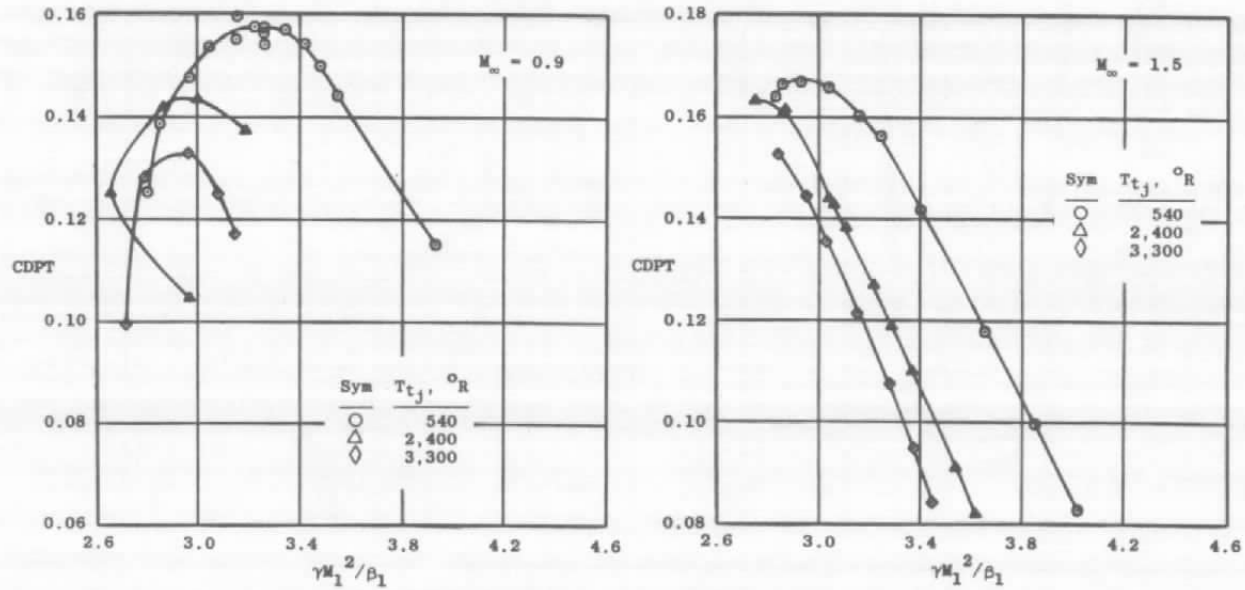
f. Jet boundary Mach number
 Figure 12. Continued.

External Configuration: 25-deg Boattail
 Internal Configuration: HF1, $A/A^* = 1.0$, $\theta_N = 0$ deg
 Free-Stream Conditions: $M_\infty = 0.9$, $Re = 2.5 \times 10^6$
 $M_\infty = 1.5$, $Re = 2.5 \times 10^6$



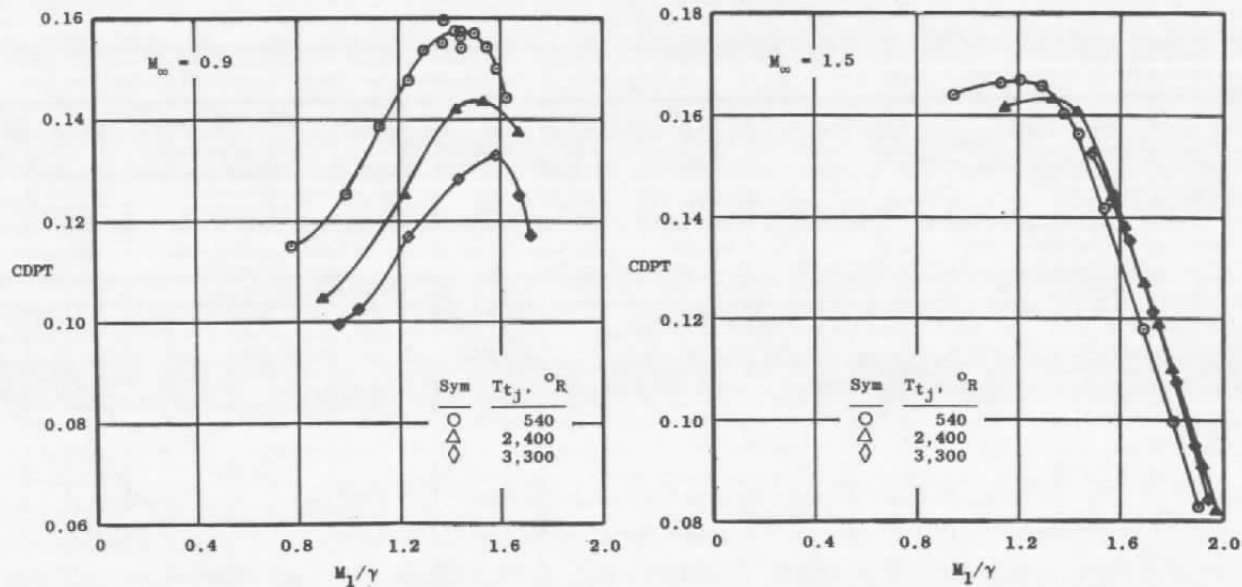
g. Jet boundary matching parameter
 Figure 12. Continued.

External Configuration: 25-deg Boattail
 Internal Configuration: HF1, $A/A^* = 1.0$, $\theta_N = 0$ deg
 Free-Stream Conditions: $M_\infty = 0.9$, $Re = 2.5 \times 10^6$
 $M_\infty = 1.5$, $Re = 2.5 \times 10^6$



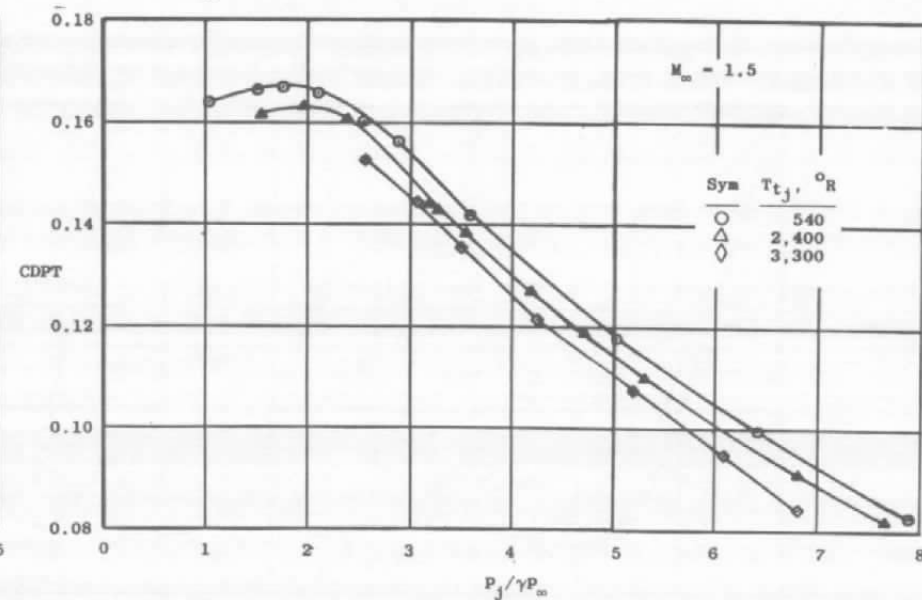
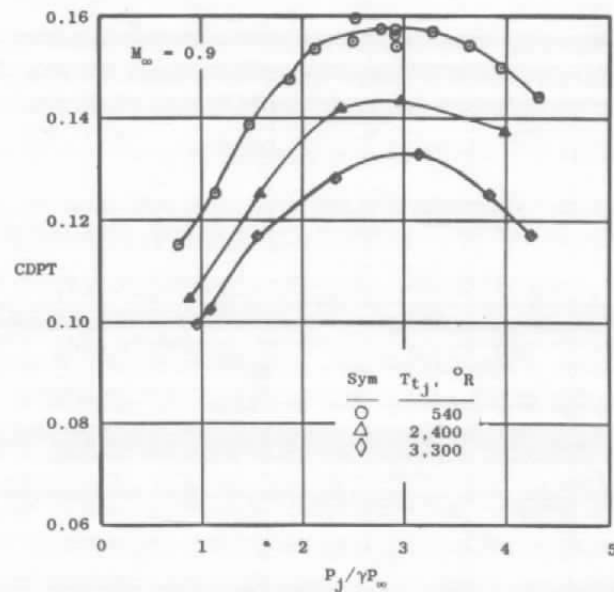
h. Jet boundary matching parameter
 Figure 12. Continued.

External Configuration: 25-deg Boattail
 Internal Configuration: HFI, $A/A^* = 1.0$, $\theta_N = 0$ deg
 Free-Stream Conditions: $M_\infty = 0.9$, $Re = 2.5 \times 10^6$
 $M_\infty = 1.5$, $Re = 2.5 \times 10^6$



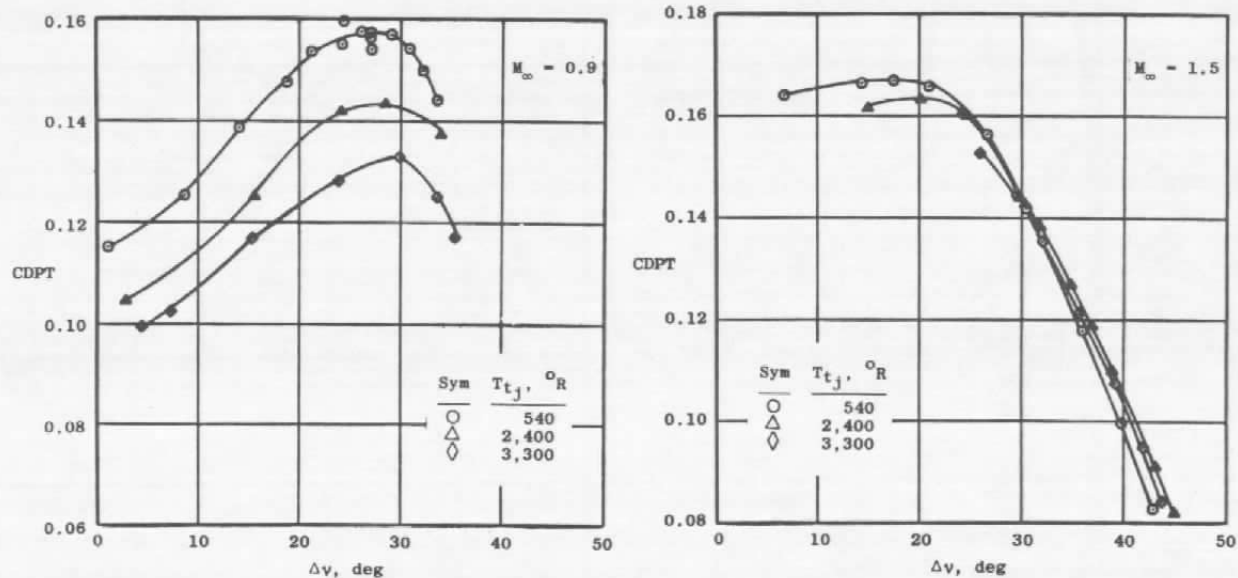
i. Jet boundary Mach number corrected for specific heat ratio
 Figure 12. Continued.

External Configuration: 25-deg Boattail
 Internal Configuration: HFL, $A/A^* = 1.0$, $\theta_N = 0$ deg
 Free-Stream Conditions: $M_\infty = 0.9$, $Re = 2.5 \times 10^6$
 $M_\infty = 1.5$, $Re = 2.5 \times 10^6$



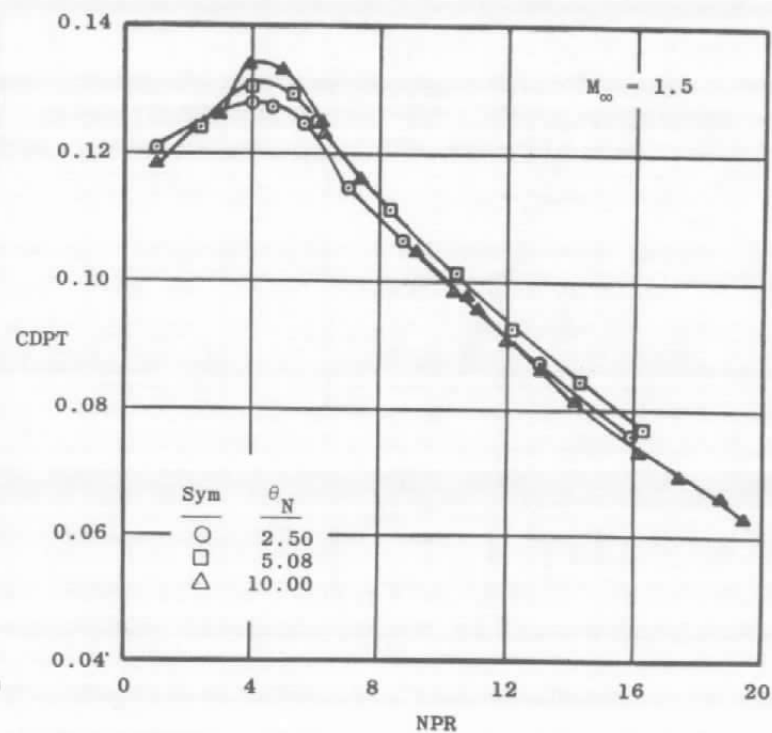
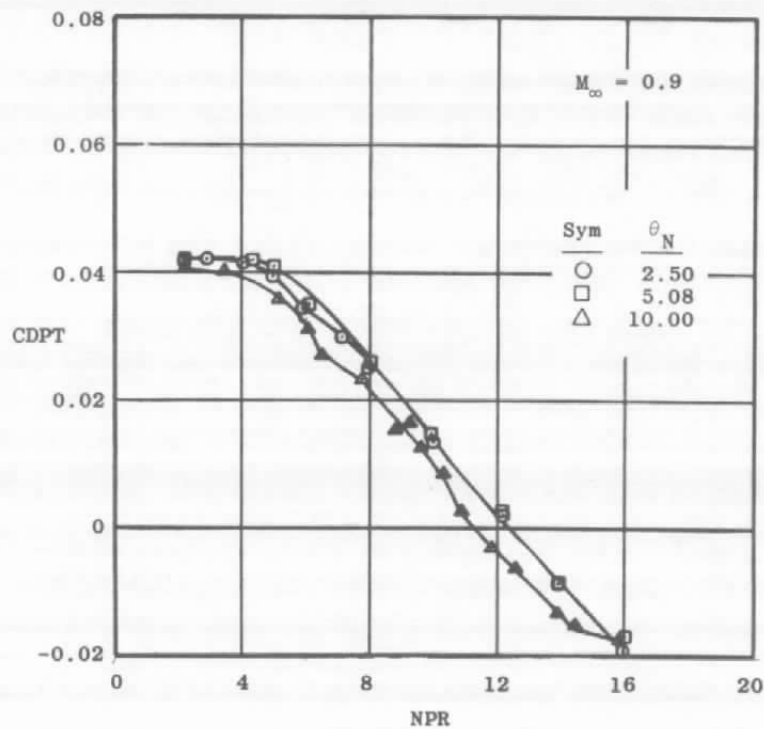
j. Nozzle exit static pressure ratio corrected for specific heat ratio
 Figure 12. Continued.

External Configuration: 25-deg Boattail
 Internal Configuration: HFI, $A/A^* = 1.0$, $\theta_N = 0$ deg
 Free-Stream Conditions: $M_\infty = 0.9$, $Re = 2.5 \times 10^6$
 $M_\infty = 1.5$, $Re = 2.5 \times 10^6$



k. Incremental Prandtl-Meyer angle
 Figure 12. Concluded.

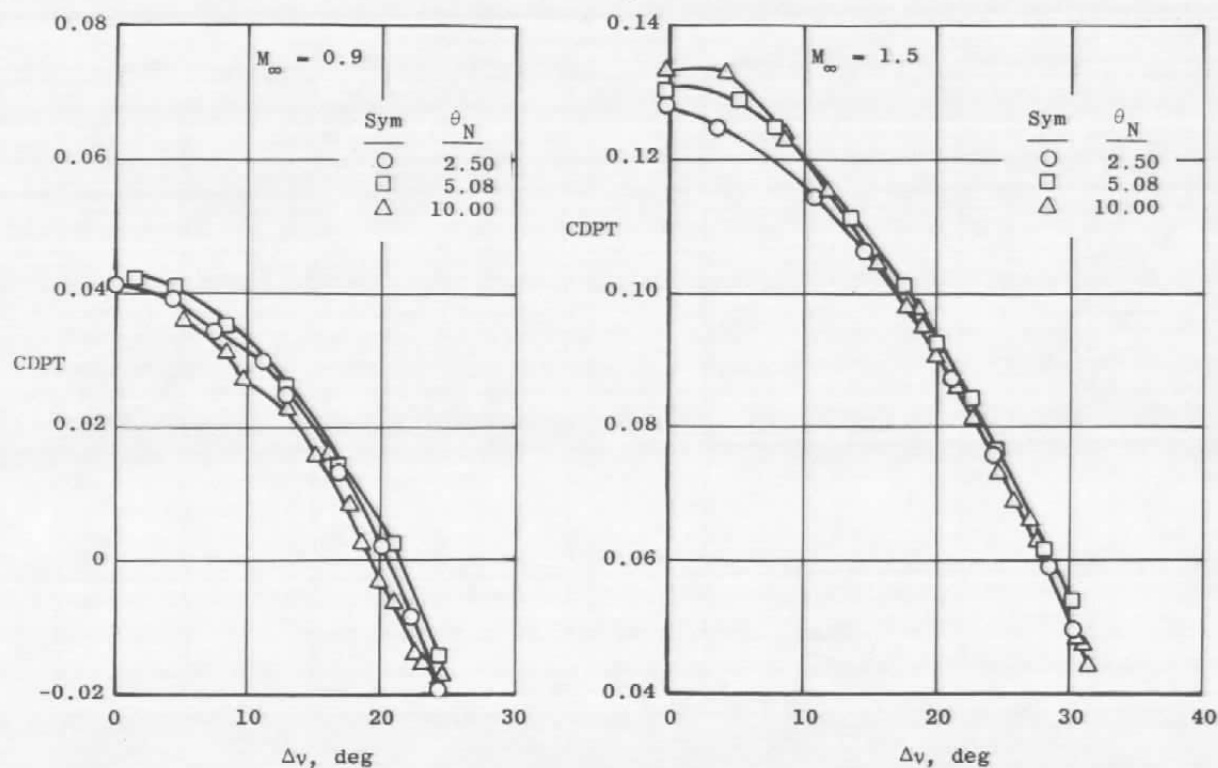
External Configuration: 15-deg Boattail
 Internal Configuration: CF1, $A/A^* = 1.22$
 Free-Stream Conditions: $M_\infty = 0.9$, $Re = 1.5 \times 10^6$
 $M_\infty = 1.5$, $Re = 2.0 \times 10^6$



a. Nozzle total pressure ratio

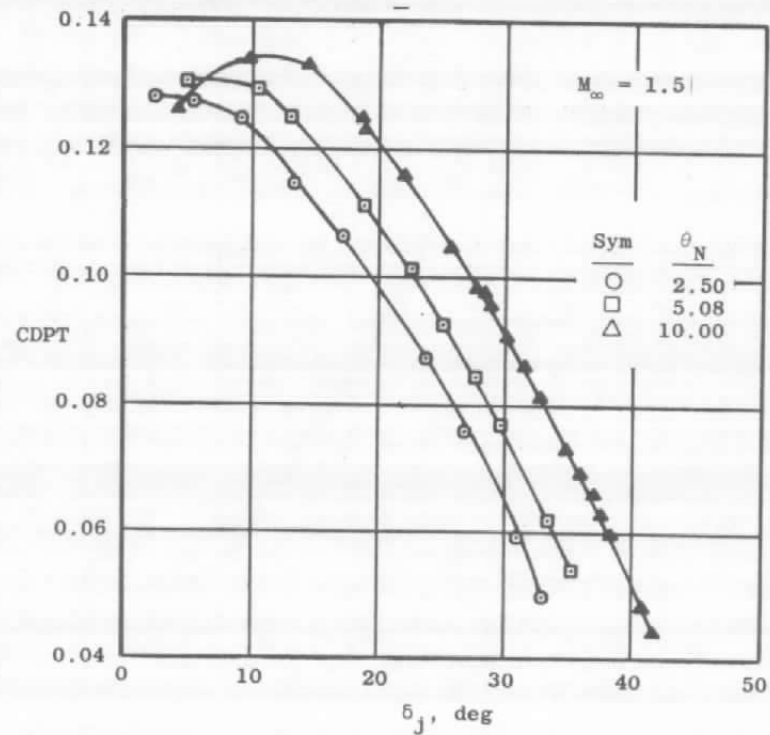
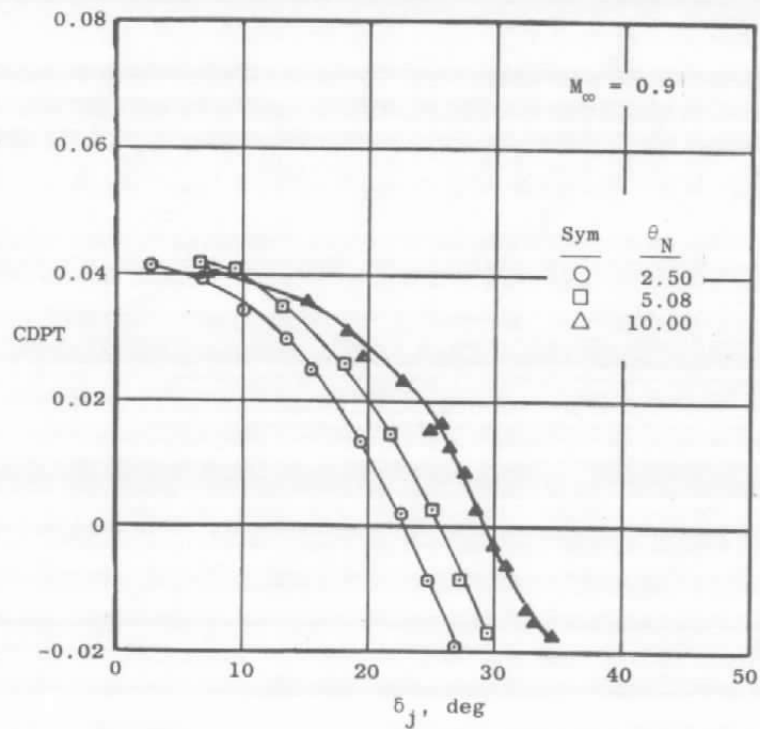
Figure 13. Nozzle divergence angle effects on afterbody pressure drag coefficient with unseparated afterbody flow.

External Configuration: 15-deg Boattail
 Internal Configuration: CF1, $A/A^* = 1.22$
 Free-Stream Conditions: $M_\infty = 0.9$, $Re = 2.5 \times 10^6$
 $M_\infty = 1.5$, $Re = 2.5 \times 10^6$



b. Incremental Prandtl-Meyer angle
 Figure 13. Continued.

External Configuration: 15-deg Boattail
 Internal Configuration: CF1, $A/A^* = 1.22$
 Free-Stream Conditions: $M_\infty = 0.9$, $Re = 1.5 \times 10^6$
 $M_\infty = 1.5$, $Re = 2.0 \times 10^6$



c. Initial jet inclination angle
 Figure 13. Concluded.

Sym	A/A*	θ_N , deg	NPR
○	1.219	2.50	12.0
□	1.222	5.08	12.0
△	1.213	10.00	12.0

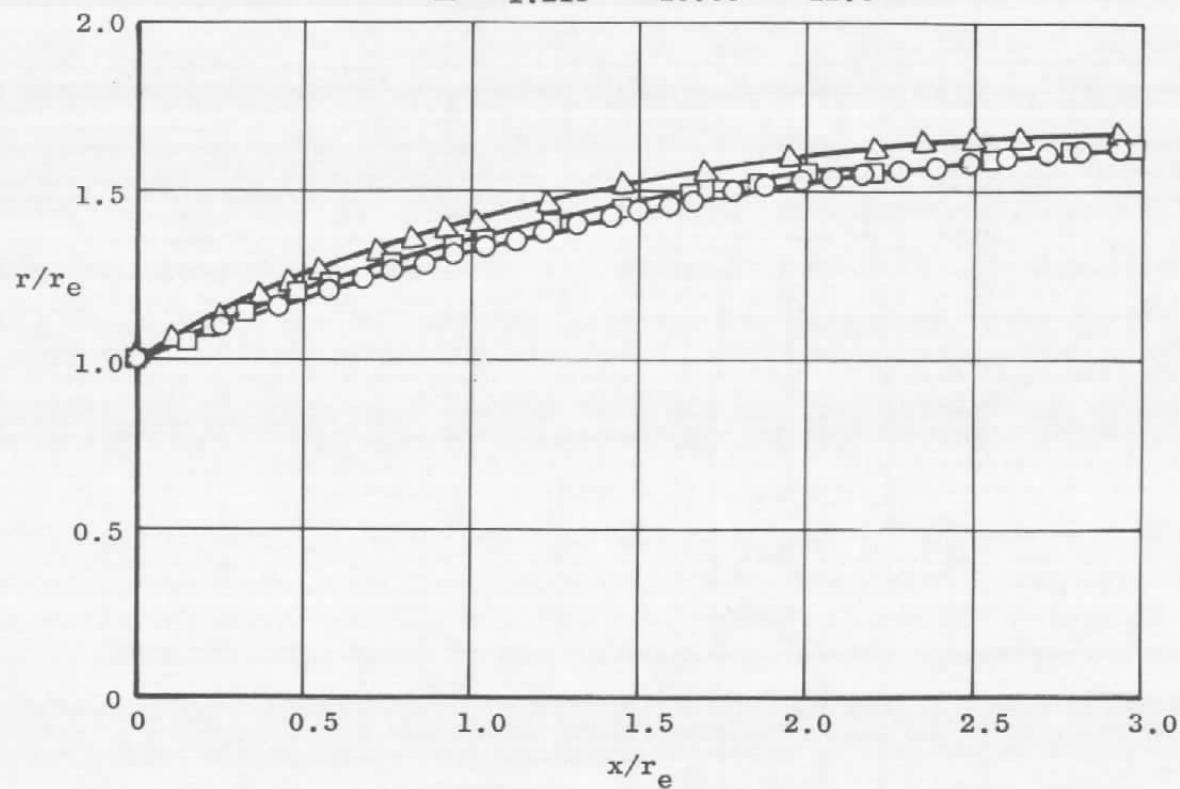
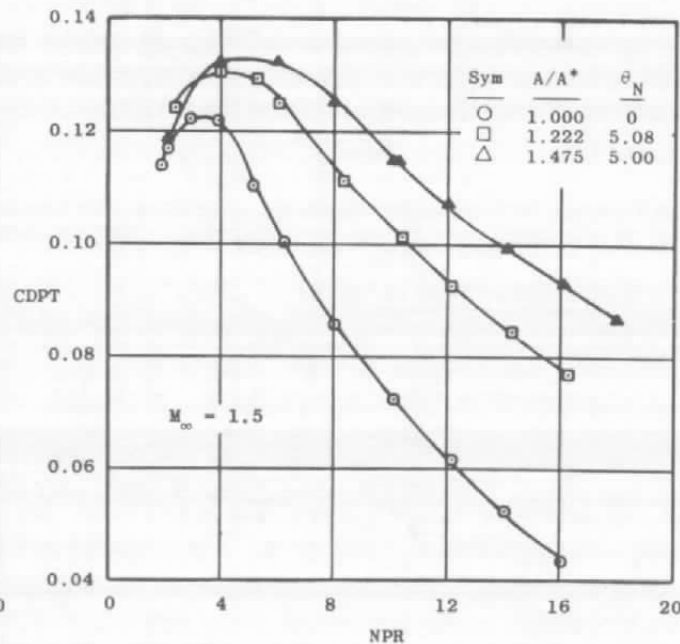
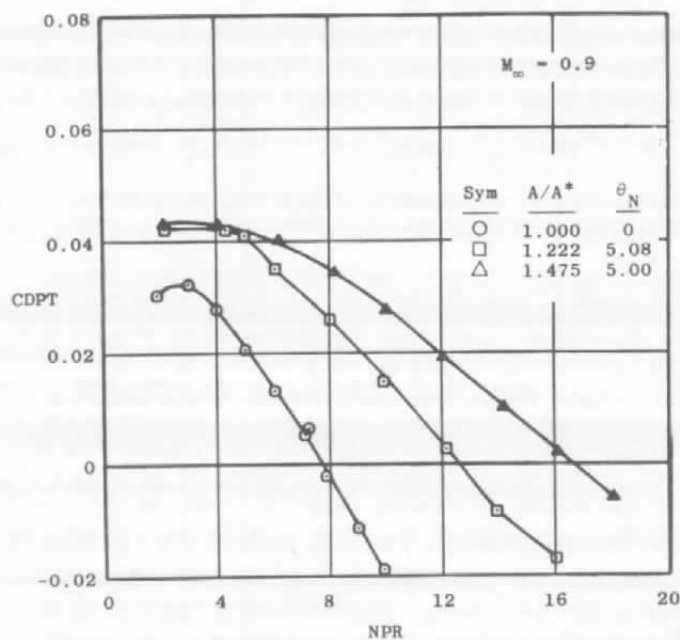


Figure 14. Comparison of quiescent MOC jet plume boundaries evaluated at equal drag conditions with nozzle divergence half-angle as a variable.

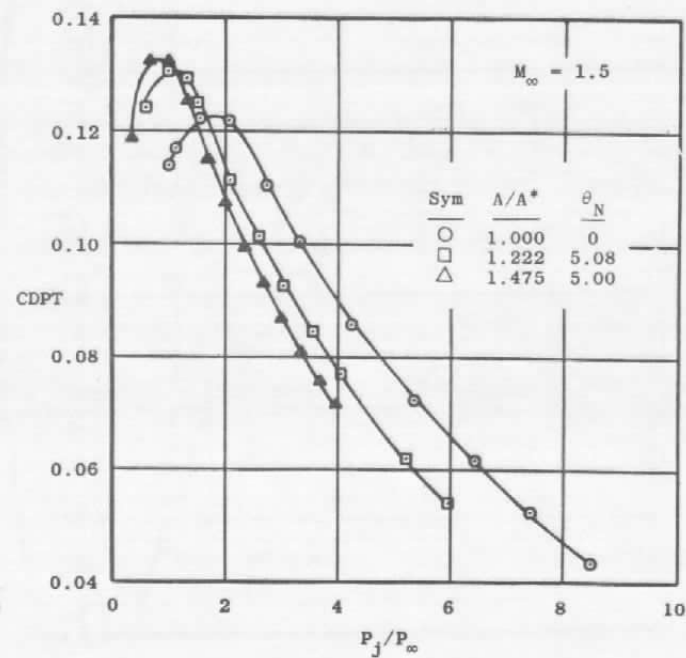
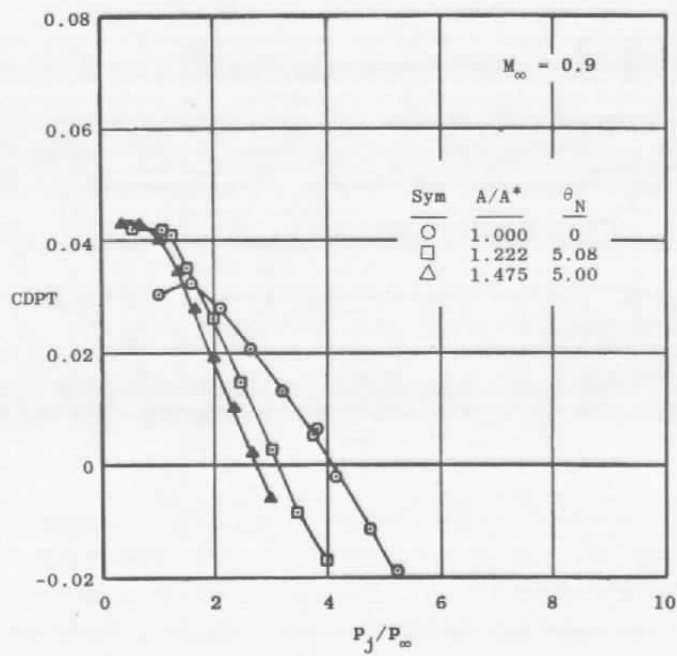
External Configuration: 15-deg Boattail
 Internal Configuration: CF1
 Free-Stream Conditions: $M_\infty = 0.9$, $Re = 1.5 \times 10^6$
 $M_\infty = 1.5$, $Re = 2.0 \times 10^6$



a. Nozzle total pressure ratio

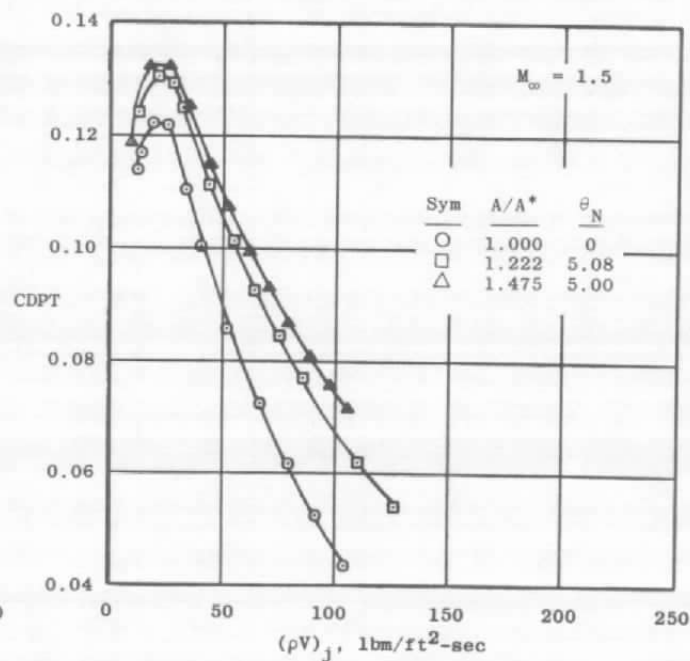
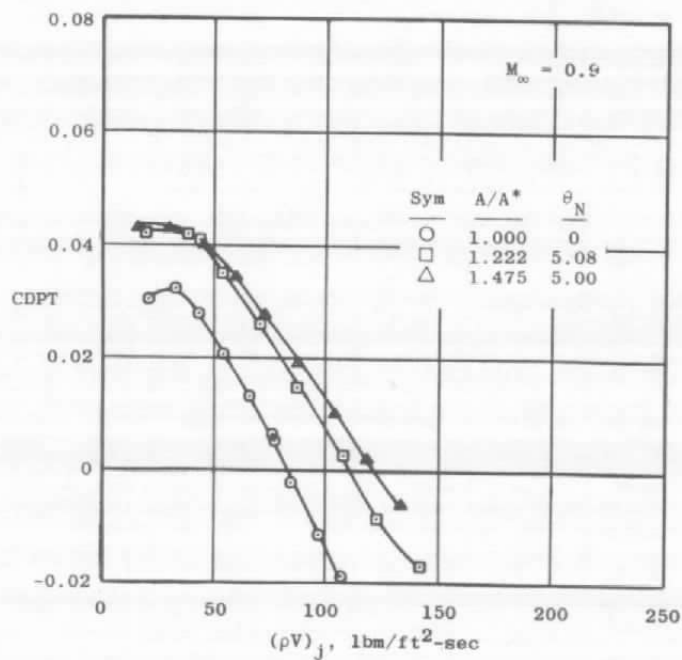
Figure 15. Nozzle exit-to-throat area ratio effects on afterbody pressure drag coefficient with unseparated afterbody flow.

External Configuration: 15-deg Boattail
 Internal Configuration: CF1
 Free-Stream Conditions: $M_{\infty} = 0.9$, $Re = 1.5 \times 10^6$
 $M_{\infty} = 1.5$, $Re = 2.0 \times 10^6$



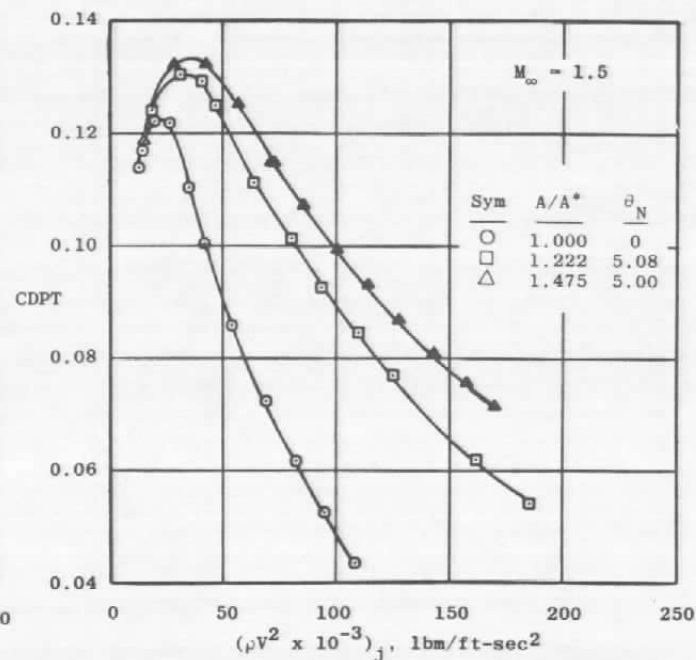
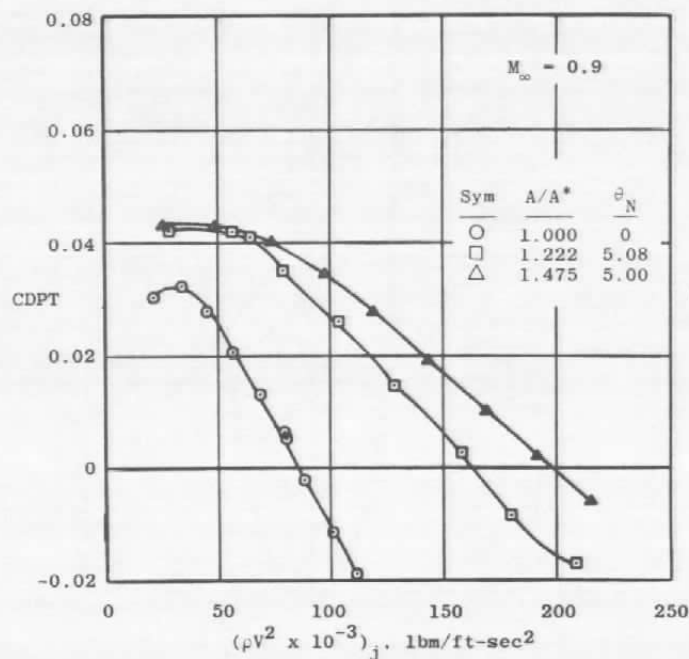
b. Nozzle exit static pressure ratio
 Figure 15. Continued.

External Configuration: 15-deg Boattail
 Internal Configuration: CF1
 Free-Stream Conditions: $M_{\infty} = 0.9$, $Re = 1.5 \times 10^6$
 $M_{\infty} = 1.5$, $Re = 2.0 \times 10^6$



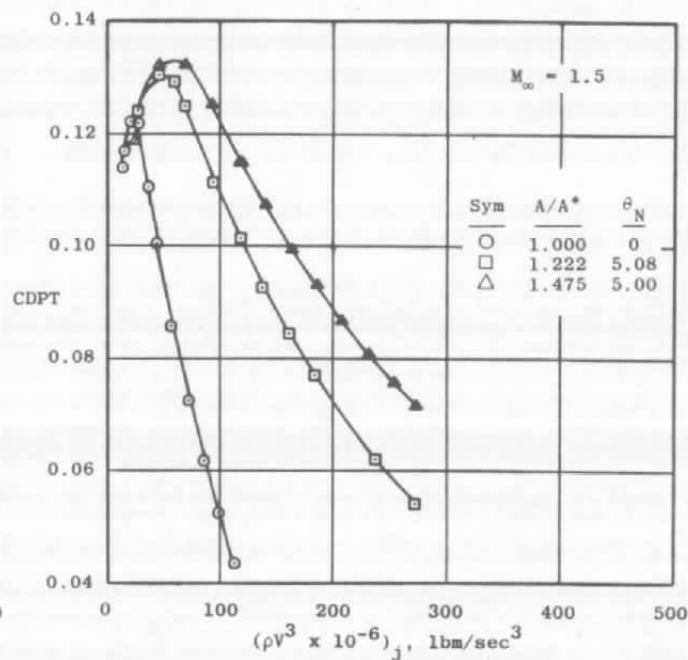
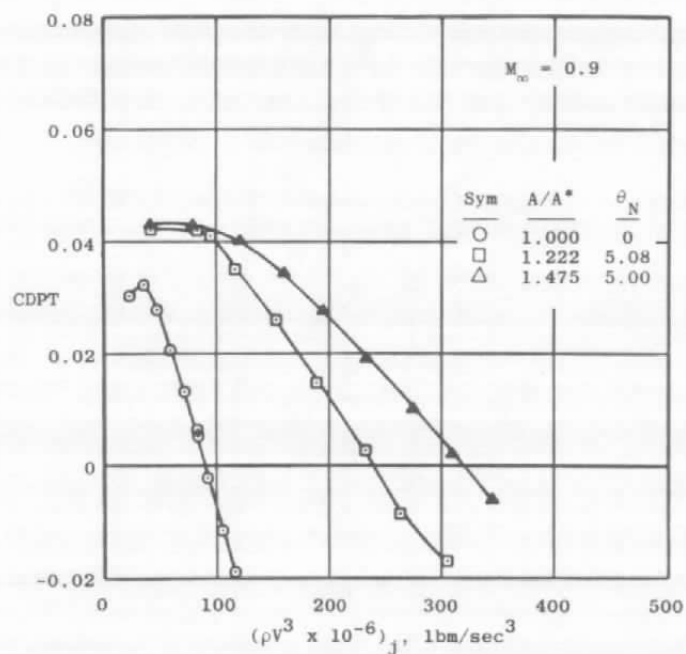
c. Nozzle exit mass flow flux
 Figure 15. Continued.

External Configuration: 15-deg Boattail
 Internal Configuration: CF1
 Free-Stream Conditions: $M_\infty = 0.9$, $Re = 1.5 \times 10^6$
 $M_\infty = 1.5$, $Re = 2.0 \times 10^6$



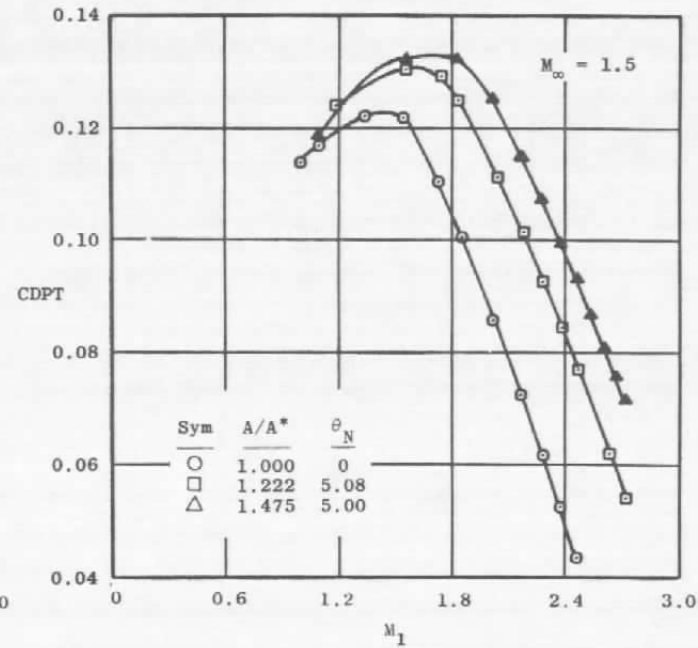
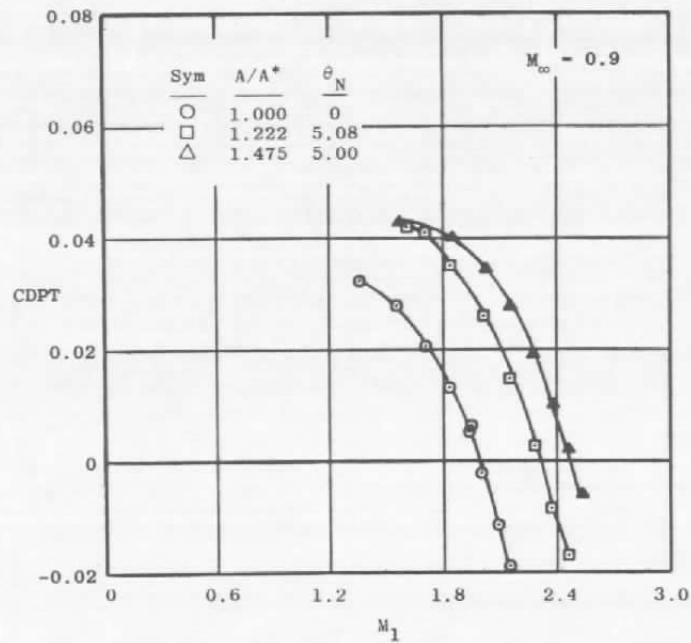
d. Nozzle exit momentum flux
 Figure 15. Continued.

External Configuration: 15-deg Boattail
 Internal Configuration: CF1
 Free-Stream Conditions: $M_\infty = 0.9$, $Re = 1.5 \times 10^6$
 $M_\infty = 1.5$, $Re = 2.0 \times 10^6$



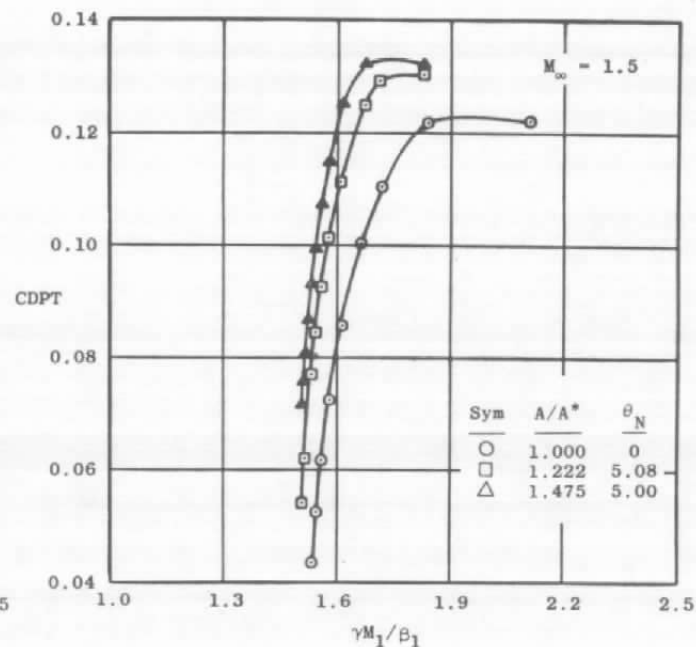
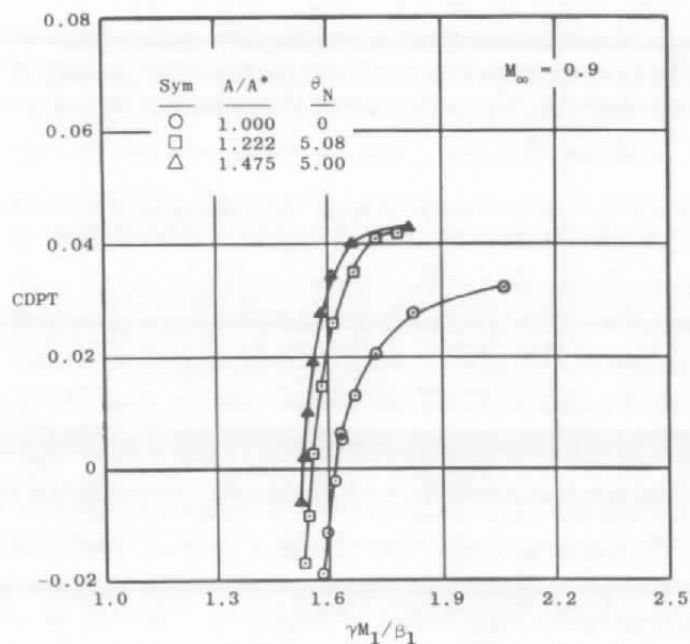
e. Nozzle exit kinetic energy flux
 Figure 15. Continued.

External Configuration: 15-deg Boattail
 Internal Configuration: CFI
 Free-Stream Conditions: $M_\infty = 0.9$, $Re = 1.5 \times 10^6$
 $M_\infty = 1.5$, $Re = 2.0 \times 10^6$



f. Jet boundary Mach number
 Figure 15. Continued.

External Configuration: 15-deg Boattail
 Internal Configuration: CF1
 Free-Stream Conditions: $M_{\infty} = 0.9$, $Re = 1.5 \times 10^6$
 $M_{\infty} = 1.5$, $Re = 2.0 \times 10^6$



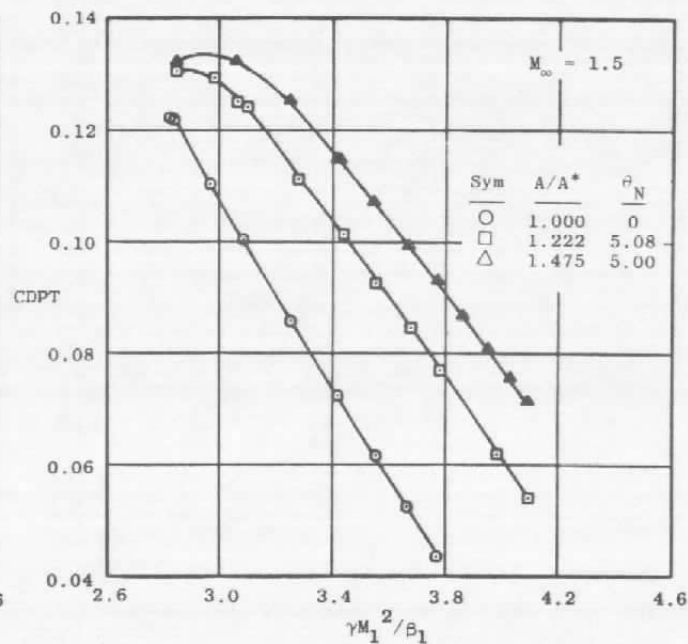
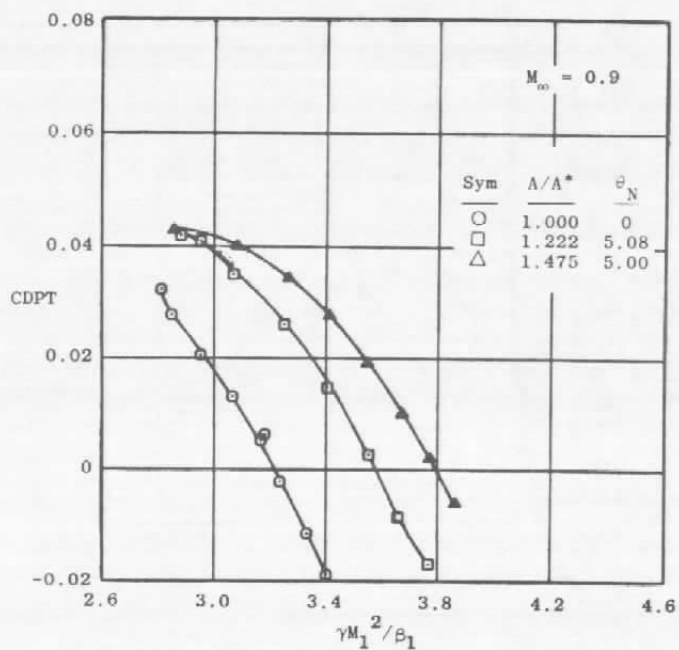
g. Jet boundary matching parameter
 Figure 15. Continued.

External Configuration: 15-deg Boattail

Internal Configuration: CF1

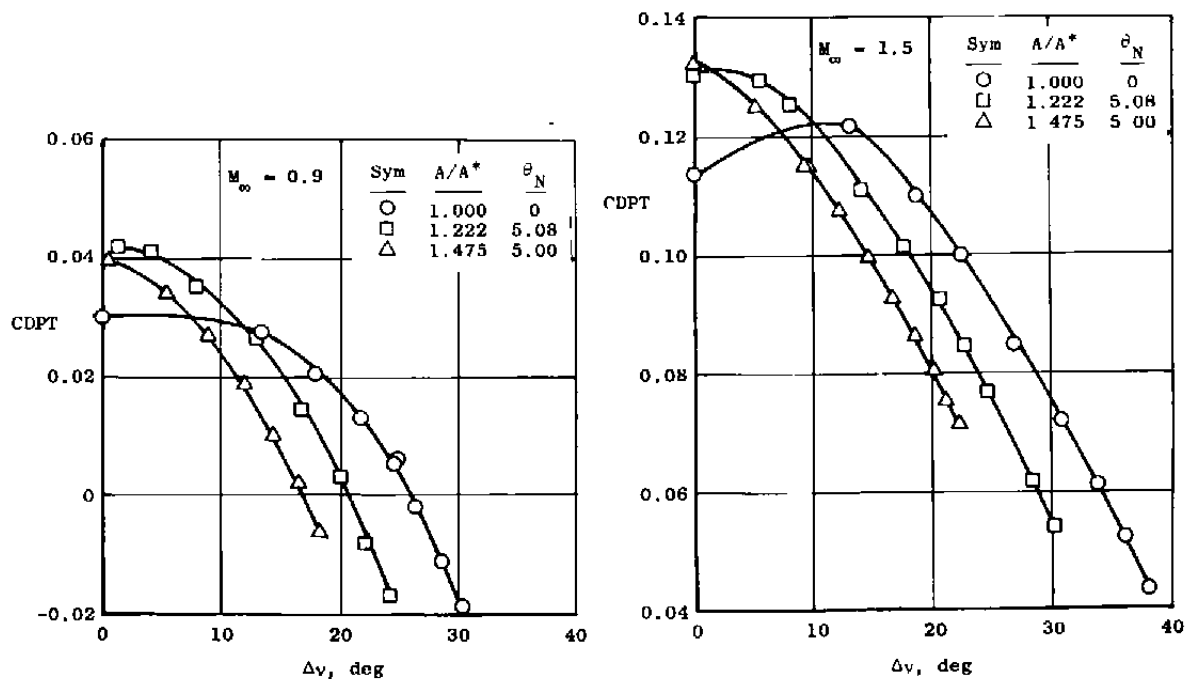
Free-Stream Conditions: $M_\infty = 0.9$, $Re = 1.5 \times 10^6$

$M_\infty = 1.5$, $Re = 2.0 \times 10^6$



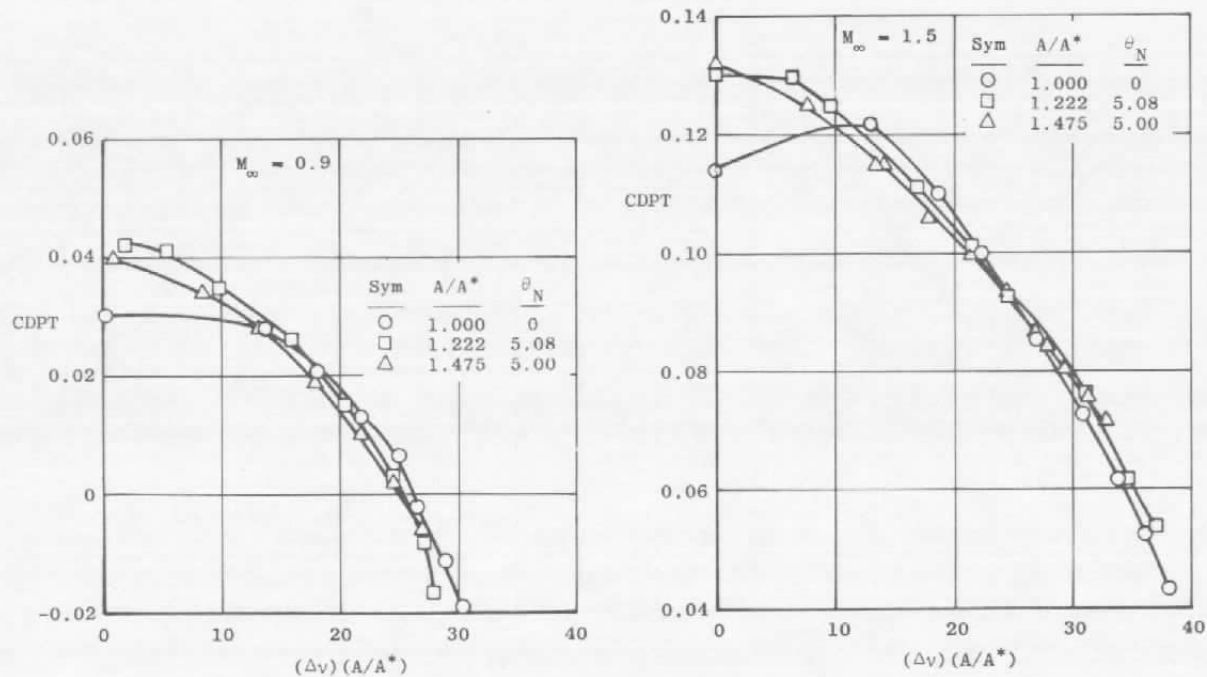
h. Jet boundary matching parameter
Figure 15. Continued.

External Configuration: 15-deg Boattail
 Internal Configuration: CF1
 Free-Stream Conditions: $M_\infty = 0.9$, $Re = 2.5 \times 10^6$
 $M_\infty = 1.5$, $Re = 2.5 \times 10^6$



i. Incremental Prandtl-Meyer angle
 Figure 15. Continued.

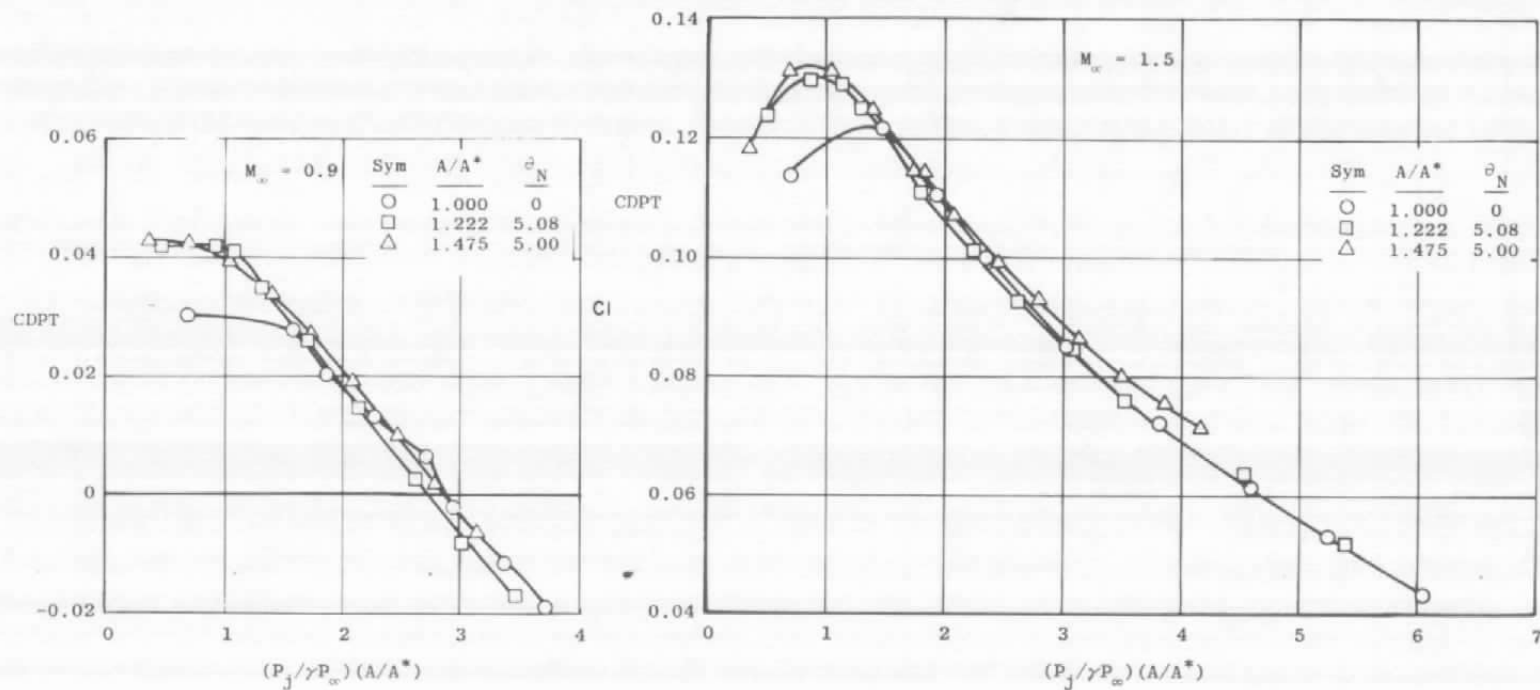
External Configuration: 15-deg Boattail
 Internal Configuration: CF1
 Free-Stream Conditions: $M_\infty = 0.9$, $Re = 2.5 \times 10^6$
 $M_\infty = 1.5$, $Re = 2.5 \times 10^6$



j. Incremental Prandtl-Meyer angle corrected for nozzle exit-to-throat area ratio
 Figure 15. Continued.

External Configuration: 15-deg Boattail

Internal Configuration: CFI

Free-Stream Conditions: $M_\infty = 0.9$, $Re = 2.5 \times 10^6$ $M_\infty = 1.5$, $Re = 2.5 \times 10^6$ 

k. Nozzle exit static pressure ratio corrected for specific heat ratio and nozzle exit-to-throat area ratio

Figure 15. Concluded.

Sym	A/A^*	θ_N , deg	NPR
○	1.000	0	5.96
□	1.222	5.08	10.25
△	1.475	5.00	14.15

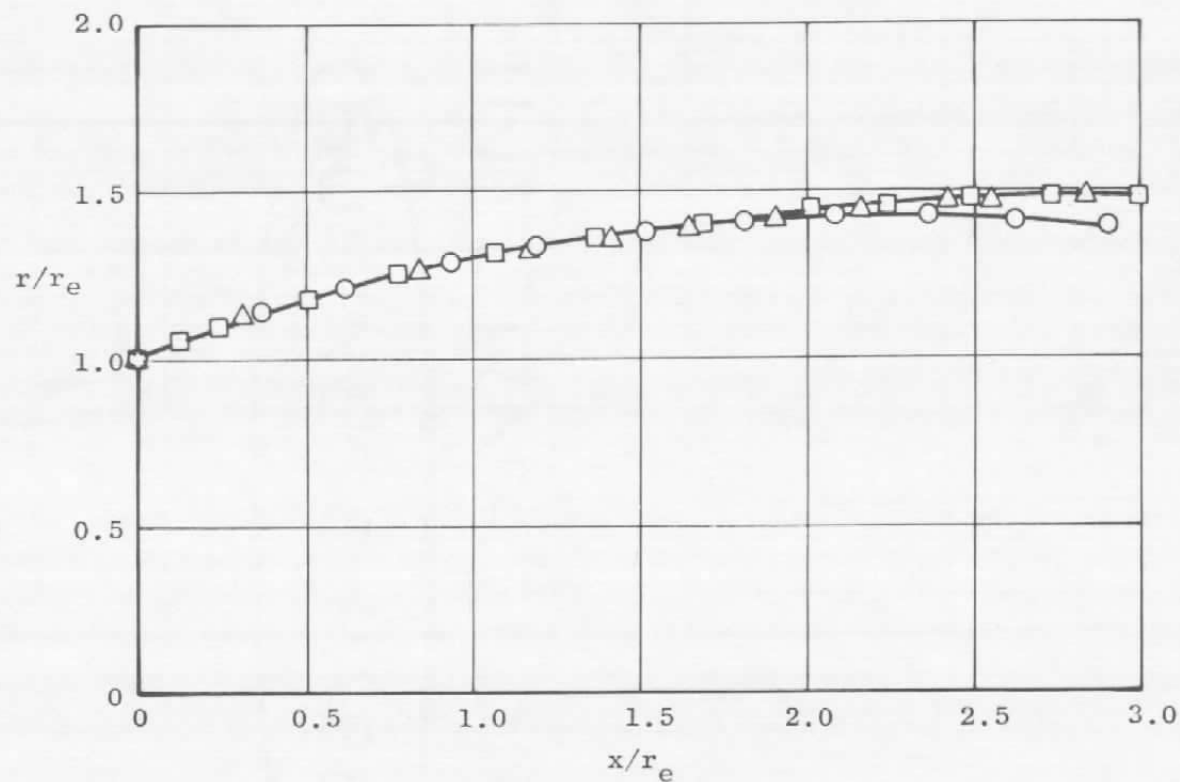


Figure 16. Comparison of quiescent MOC jet plume boundaries evaluated at equal drag conditions with nozzle exit-to-throat area ratio as a variable.

External Configuration: 15-deg Boattail
 Internal Configuration: HF1, $A/A^* = 1.0$, $\theta_N = 0$ deg
 Free-Stream Conditions: $M_\infty = 0.9$, $Re = 2.5 \times 10^6$
 $M_\infty = 1.5$, $Re = 2.5 \times 10^6$

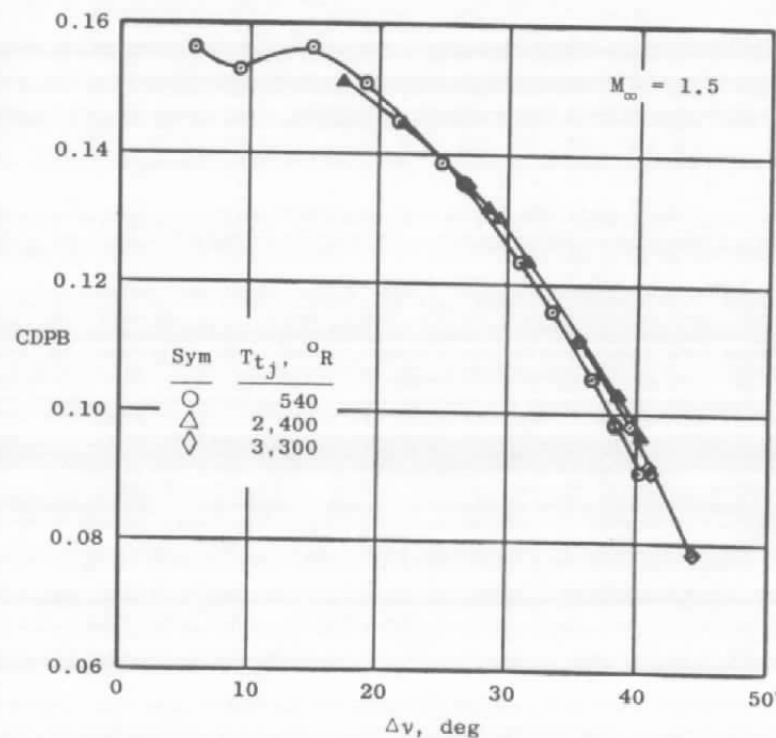
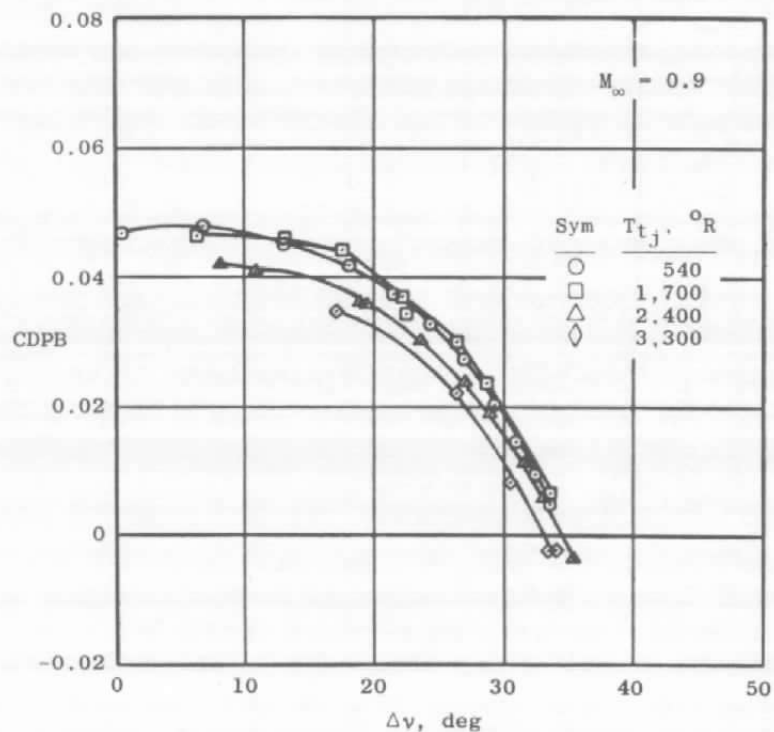


Figure 17. Model strut interference effects on the jet simulation performance of $\Delta\nu$ with variable jet total temperature.

External Configuration: 15-deg Boattail

Internal Configuration: CF1

Free-Stream Conditions: $M_\infty = 0.9$, $Re = 2.5 \times 10^6$

$M_\infty = 1.5$, $Re = 2.5 \times 10^6$

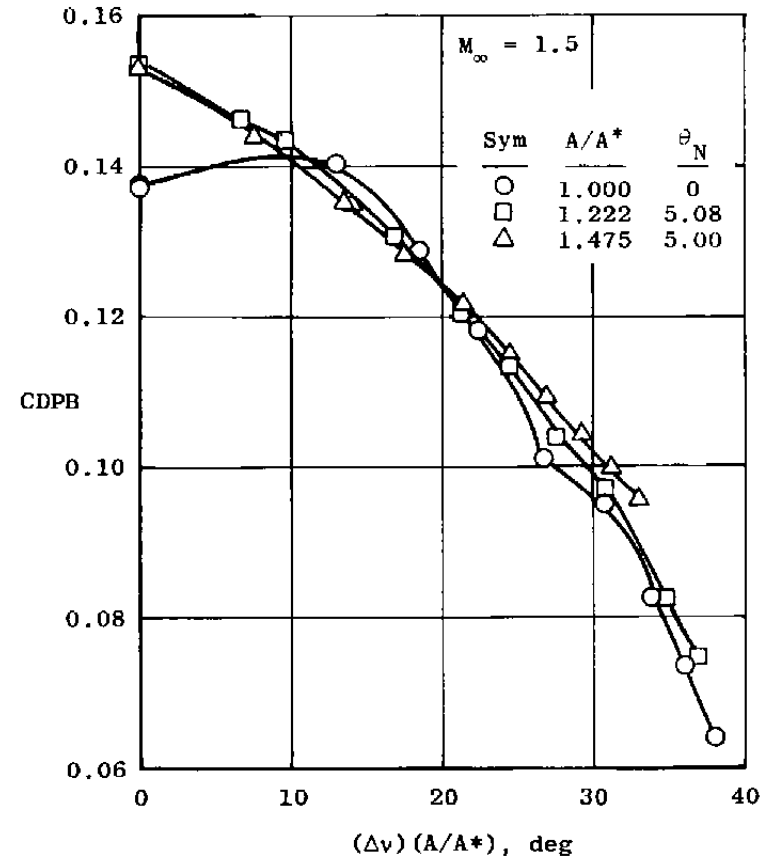
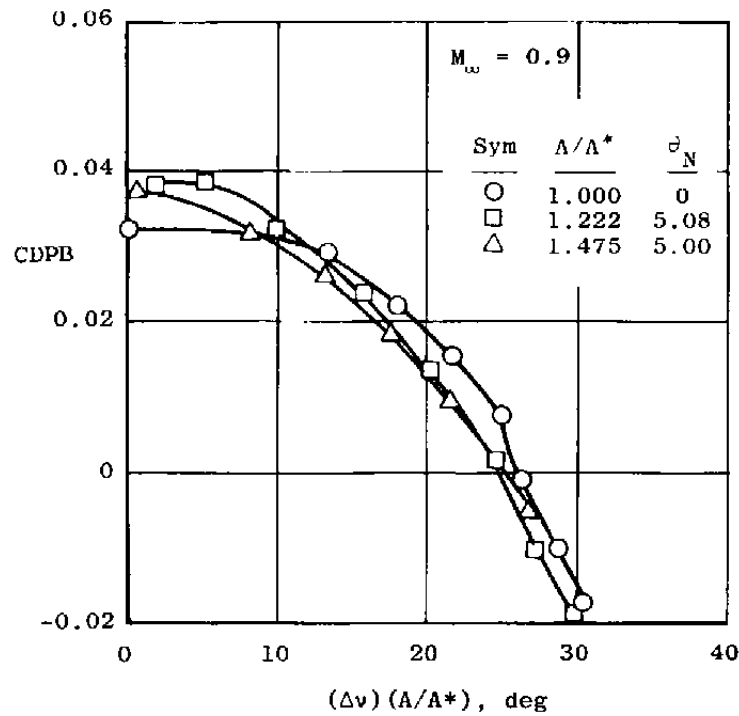
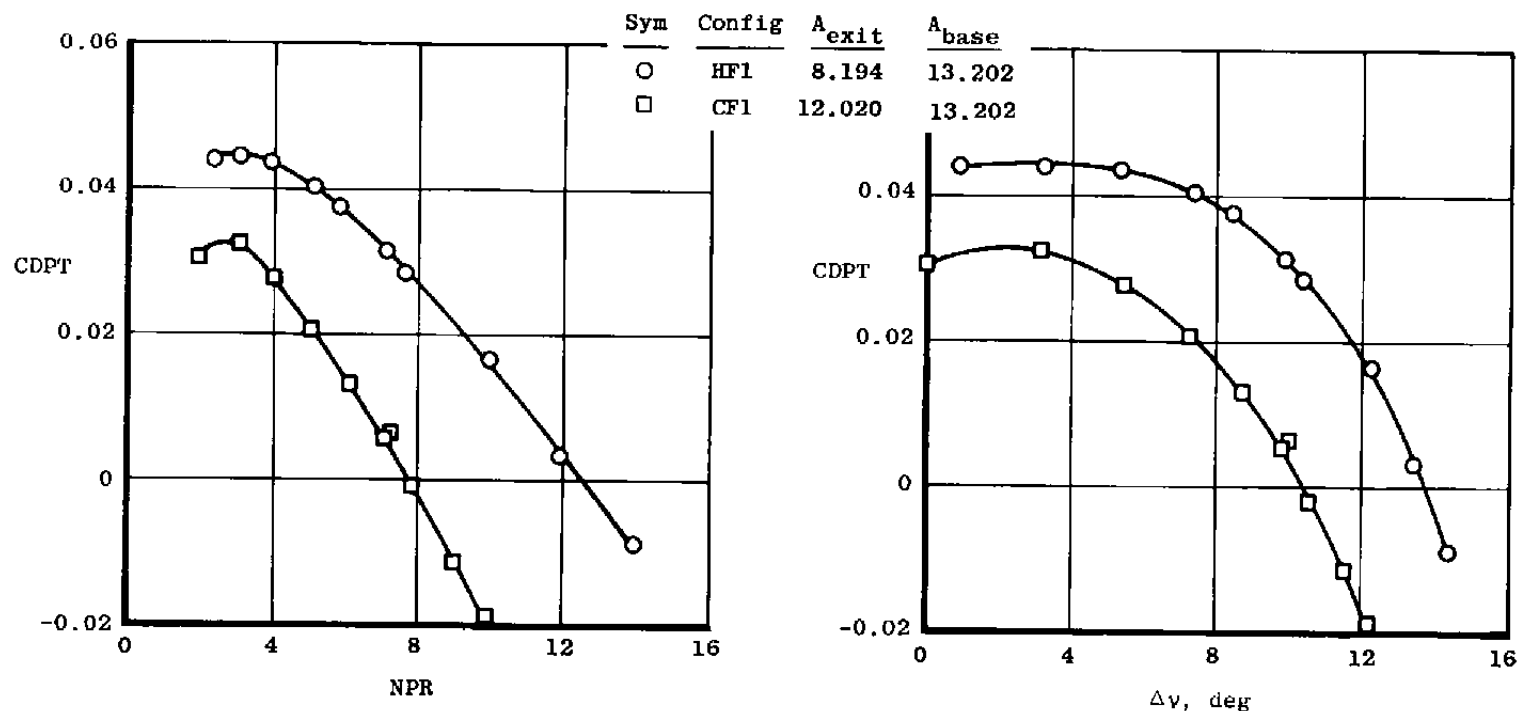


Figure 18. Model strut interference effects on the jet simulation performance of $(\Delta v) (A/A^*)$ with variable nozzle exit-to-throat area ratio.

External Configuration: 15-deg Boattail
 Internal Configuration: $A/A^* = 1.0$
 Free-Stream Conditions: $M_\infty = 0.9$, $Re = 1.5 \times 10^6$



a. Nozzle total pressure ratio

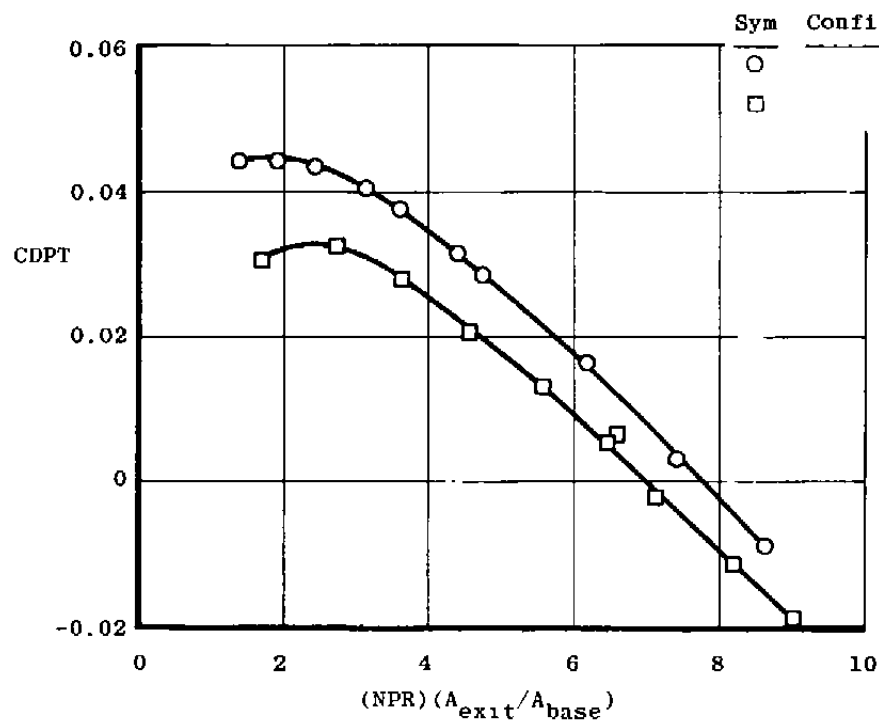
b. Incremental Prandtl-Meyer angle

Figure 19. Nozzle base area effects on afterbody pressure drag coefficient with unseparated afterbody flow.

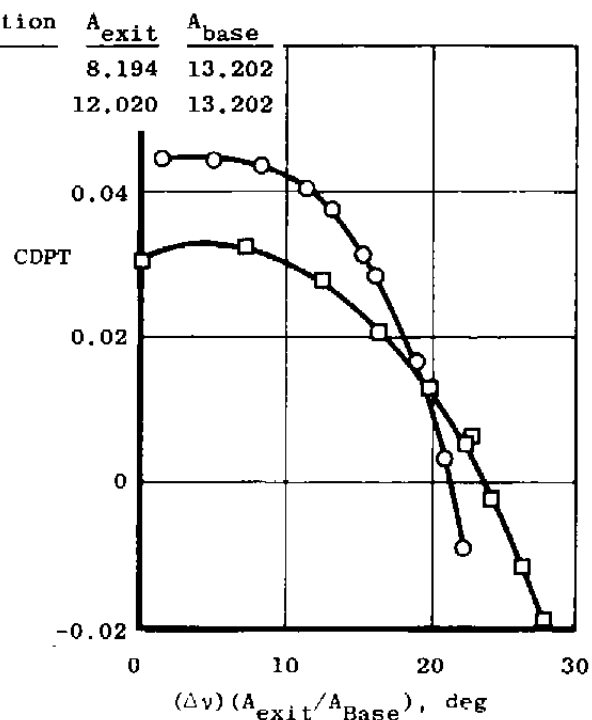
External Configuration: 15-deg Boattail

Internal Configuration: $A/A^* = 1.0$

Free-Stream Conditions: $M_\infty = 0.9$, $Re = 1.5 \times 10^6$



c. Nozzle total pressure ratio corrected for nozzle exit-to-base area ratio



d. Incremental Prandtl-Meyer angle corrected for nozzle exit-to-base area ratio

Figure 19. Concluded.

Table 1. Model Configurations

Configuration	Hot-Flow Convergent Nozzle Configuration	Hot-Flow Convergent- Divergent Nozzle Configuration	Cold-Flow Configuration
Configuration Code	HF1	HF2	CF1
Model Length, in.	146.97	153.22	146.97
Forebody Length, in.	130.47	135.47	130.47
Afterbody Length, in.	16.50	17.75	16.50
Maximum Body Diameter, in.	9.86	9.86	9.86
Tunnel Station of Model Nose, in.	124.50	124.50	124.50
Nozzle A/A*	1.000	1.480 (Effective)	Variable (1.000, 1.222, 1.475)
Nozzle θ_N , deg	0	3.22	Variable (0, 2.5, 5.0, 10.0)

Table 2. Jet Simulation Parameter Performance for Variable Jet Total Temperature

Parameter	$\Delta CDPT = CDPT_{cold} (\gamma = 1.400) - CDPT_{hot} (\gamma = 1.275)$			
	Maximum Cold Jet Drag Condition		NPR >> NPR _{Design}	
	$M_\infty = 0.9$ $CDPT_{cold} = 0.0458$	$M_\infty = 1.5$ $CDPT_{cold} = 0.1330$	$M_\infty = 0.9$ $CDPT_{cold} = 0.0200$	$M_\infty = 1.5$ $CDPT_{cold} = 0.1000$
NPR	0.0080	0.0040	0.0250	0.0125
P_j/P_∞	0.0080	0.0040	0.0250	0.0100
$(\rho V)_j$	0.0270	0.0420	0.0800	0.0800
$(\rho V)_j^2$	0.0080	0.0040	0.0300	0.0125
$(\rho V)_j^3$	-0.0050	-0.0120	-0.0200	-0.0250
M_1	0.0060	0.0030	0.0300	0.0150
$\gamma M_1/\beta_1$	0.0040	0.0040	-0.0150	-0.0300
$\gamma M_1^2/\beta_1$	0.0250	0.0150	0.0600	0.0400
M_1/γ	0.0080	0.0020	0.0060	0.0090
$P_j/\gamma P_\infty$	0.0060	0.0020	0.0150	0.0030
Δv	0.0060	0.0040	0.0060	0.0025

Table 3. Jet Simulation Parameter Performance for Variable Nozzle Exit-to-Throat Area Ratio

Parameter	$\Delta CDPT = CDPT_{A/A^* = 1.000} - CDPT_{A/A^* = 1.475}$			
	NPR \approx NPR _{Design} (A/A* = 1.000)		NPR \gg NPR _{Design} (A/A* = 1.000)	
	$M_\infty = 0.9$ CDPT _{sonic} = 0.0300	$M_\infty = 1.5$ CDPT _{sonic} = 0.1220	$M_\infty = 0.9$ CDPT _{sonic} = 0.0	$M_\infty = 1.5$ CDPT _{sonic} = 0.0600
NPR	-0.0140	-0.0100	-0.0350	-0.0470
P_j/P_∞	-0.0100	-0.0100	0.0230	0.0200
$(\rho V)_j$	-0.0110	-0.0100	-0.0220	-0.0240
$(\rho V)_j^2$	-0.0110	-0.0100	-0.0380	-0.0450
$(\rho V)_j^3$	-0.0100	-0.0020	-0.0420	-0.0640
M_1	-0.0100	-0.0080	-0.0380	-0.0460
$\gamma M_1/\beta_1$	-0.0100	-0.0080	-0.0360	-0.0500
$\gamma M_1^2/\beta_1$	-0.0080	-0.0100	-0.0360	-0.0460
Δv	-0.0100	-0.0150	0.0300	0.0260
$(\Delta v) (A/A^*)$	-0.0100	-0.0050	0.0020	-0.0030
$(P_j/\gamma P_\infty) (A/A^*)$	-0.0100	-0.0060	0.0020	-0.0040

NOMENCLATURE

A	Nozzle exit area, in. ²
A_t	Nozzle throat area, in. ²
A/A^*	Nozzle exit-to-throat area ratio
C_{D_p}	Afterbody pressure drag coefficient, $D_p/q_\infty S$
C_d	Nozzle discharge coefficient
D_p	Integrated afterbody pressure drag, lbf
f/a	Fuel/air ratio
M	Mach number
M_1/γ	Jet boundary Mach number corrected for specific heat ratio
NPR	Nozzle total-to-free-stream static pressure ratio, P_{t_j}/P_∞
P	Static pressure, psia
P_j/P_∞	Nozzle exit static-to-free-stream static pressure ratio
P_t	Total pressure, psia
q	Dynamic pressure, psi
r	Jet plume boundary radius measured from nozzle centerline, in.
r_e	Nozzle exit radius, in.

S	Model cross-sectional area, 76 in. ²
T _t	Total temperature, °R
V	Velocity, ft/sec
X	Distance aft of nozzle exit, in.
β	(M ² - 1) ^{1/2}
γ	Specific heat ratio of the jet
γM ₁ /β ₁	Jet plume boundary simulation parameter
γM ₁ ² /β ₁	Jet plume boundary simulation parameter
Δv	Incremental change in Prandtl-Meyer angle, (v ₁ - v _j), deg
δ _j	Initial jet inclination angle, (Δv + θ _N), deg
θ _N	Nozzle divergence half-angle, deg
v	Prandtl-Meyer angle, deg
ρ	Mass density, lbm/ft ³
ρV	Mass flow flux, lbm/ft ² -sec
ρV ²	Momentum flux, lbm/ft-sec ²
ρV ³	Kinetic energy flux, lbm/sec ³

SUBSCRIPTS

1	Conditions at jet plume boundary
B	Bottom row of afterbody and boattail pressures
j	Conditions at nozzle exit plane
T	Top row of afterbody and boattail pressures
t	Total or stagnation conditions
∞	Tunnel free-stream conditions